



LUND UNIVERSITY

Precision Standard Model Phenomenology for High Energy Processes

Vitos, Timea

2023

[Link to publication](#)

Citation for published version (APA):

Vitos, T. (2023). *Precision Standard Model Phenomenology for High Energy Processes*. [Doctoral Thesis (compilation), Particle and nuclear physics]. Lund.

Total number of authors:

1

General rights

Unless other specific re-use rights are stated the following general rights apply:

Copyright and moral rights for the publications made accessible in the public portal are retained by the authors and/or other copyright owners and it is a condition of accessing publications that users recognise and abide by the legal requirements associated with these rights.

- Users may download and print one copy of any publication from the public portal for the purpose of private study or research.
- You may not further distribute the material or use it for any profit-making activity or commercial gain
- You may freely distribute the URL identifying the publication in the public portal

Read more about Creative commons licenses: <https://creativecommons.org/licenses/>

Take down policy

If you believe that this document breaches copyright please contact us providing details, and we will remove access to the work immediately and investigate your claim.

LUND UNIVERSITY

PO Box 117
221 00 Lund
+46 46-222 00 00



Precision Standard Model Phenomenology for High Energy Processes

TIMEA VITOS

DEPARTMENT OF PHYSICS | FACULTY OF SCIENCE | LUND UNIVERSITY



Precision Standard Model Phenomenology for
High Energy Processes

Precision Standard Model Phenomenology for High Energy Processes

by Timea Vitos



LUND
UNIVERSITY

Thesis for the degree of Doctor of Philosophy

Thesis advisor: Rikkert Frederix

Faculty opponent: Alessandro Vicini

To be presented, with the permission of the Faculty of Science of Lund University, for public criticism in
Lundmarksalen at the Department of Physics on Friday the 16th of June 2023 at 10:00.

Organization LUND UNIVERSITY Department of Physics Professorsgatan 1 SE-223 63 LUND Sweden		Document name DOCTORAL DISSERTATION	
		Date of disputation 2023-06-16	
Author(s) Timea Vitos		Sponsoring organization	
Title and subtitle Precision Standard Model Phenomenology for High Energy Processes			
Abstract <p>The present status of particle physics is that the Standard Model has been completed with the discovery of the Higgs boson in 2012, but there is a multitude of phenomena in nature which is not accounted for by this model. Researchers are investigating possibilities for detecting new physics at the current particle physics facilities, with the Large Hadron Collider (LHC) at the frontier. As no significant sign of new physics has been observed as of today, precision phenomenology becomes increasingly important. This thesis and the four papers included in it contribute to this field of precision predictions for various important processes at the LHC.</p> <p>In paper I and paper IV, the Drell-Yan process is investigated, and specifically, the decay coefficients which parameterize the spherical distribution of the outgoing leptons in the process. In the first work, we investigate the next-to-leading-order (NLO) electroweak corrections to the coefficients of the neutral-current process. In the second work, a similar study, but including also next-to-next-to-leading-order quantum chromodynamic (QCD) corrections, is performed for the decay coefficients of the charged-current Drell-Yan process. The latter process and the corresponding coefficients are of great importance for measuring the W-boson mass at the LHC.</p> <p>In paper II, the top quark pair production and the spin correlations for the process are investigated. The spin correlation information of the top quarks may reveal underlying new physics when probed at high precision. Therefore, this work computes approximate complete-NLO corrections, including electroweak corrections to the spin correlation coefficients and related leptonic distributions, contributing to the state-of-the-art high precision Standard Model predictions for these observables.</p> <p>Finally, paper III is the theoretical base of a crucial improvement to matrix-element generators. We propose in this paper to utilize a next-to-leading-colour truncation of the colour matrix in the large-N_C limit, in order to reduce the complexity of the cross section computation when a large number of QCD patrons are involved in the process. The results suggest that such a truncation of the colour expansion will facilitate for efficient computation of multi-jet events, which are a dominant background for many important processes and new physics searches at hadron colliders, such as the LHC.</p>			
Key words precision phenomenology, Standard Model predictions, NLO electroweak corrections, decay coefficients, Drell-Yan process, top quark spin correlations, colour expansion, large-N_C truncation			
Classification system and/or index terms (if any)			
Supplementary bibliographical information		Language English	
ISSN and key title		ISBN 978-91-8039-668-4 (print) 978-91-8039-667-7 (pdf)	
Recipient's notes		Number of pages 228	Price
		Security classification	

I, the undersigned, being the copyright owner of the abstract of the above-mentioned dissertation, hereby grant to all reference sources the permission to publish and disseminate the abstract of the above-mentioned dissertation.

Signature _____

Date 2023-04-25

Precision Standard Model Phenomenology for High Energy Processes

by Timea Vitos



LUND
UNIVERSITY

A doctoral thesis at a university in Sweden takes either the form of a single, cohesive research study (monograph) or a summary of research papers (compilation thesis), which the doctoral student has written alone or together with one or several other author(s).

In the latter case the thesis consists of two parts. An introductory text puts the research work into context and summarizes the main points of the papers. Then, the research publications themselves are reproduced, together with a description of the individual contributions of the authors. The research papers may either have been already published or are manuscripts at various stages (in press, submitted, or in draft).

Cover illustration front: Szabadság híd (Liberty Bridge) over the Danube in Budapest, March 2023, representing the bridge of phenomenology between experiment and theory in particle physics. The choice of bridge reflects one true pillar in life: freedom.

Cover illustration back: Picture of me in blooming Lund, April 2023.

Funding information: This thesis and the work in it was supported by the Swedish Research Council under contract numbers 2016-05996 and 2020-04423.

© Timea Vitos 2023

Faculty of Science, Department of Physics

ISBN: 978-91-8039-668-4 (print)

ISBN: 978-91-8039-667-7 (pdf)

Printed in Sweden by Media-Tryck, Lund University, Lund 2023



*Isten segédelmével,
a családomnak*

Contents

Acknowledgements	v
List of publications	vi
Magyar összefoglaló	viii
Populärvetenskaplig sammanfattning på svenska	ix
Introduction	I
1 Basic scientific introduction	2
2 Introducing particle physics phenomenology	8
2.1 The successful Standard Model	8
2.2 Cross sections and matrix-elements	19
2.3 Renormalization, regularization and resonances	21
2.4 Parameters of the Standard Model	25
2.5 Soft emissions, parton evolution and infrared safety	29
2.6 The colour expansion in the large- N_C limit	33
3 Monte Carlo collider physics	39
3.1 Monte Carlo integration	39
3.2 Perturbative fixed-order expansion	41
3.3 More on NLO EW corrections	45
3.4 Event generators	47
4 Phenomenology at the Large Hadron Collider	57
4.1 The Large Hadron Collider and its detectors	57
4.2 A key process at the LHC: Drell-Yan production	60
4.3 The most abundant heavy process: top-quark pair production	72
4.4 What washes over the detectors: multi-jet processes	80
5 Outlook	83
6 Overview of publications	90
Publications	
I Electroweak corrections to the angular coefficients in finite-p_T Z-boson production and dilepton decay	95
1 Introduction	96
2 Theoretical setup	97

2.1	Angular coefficients	97
2.2	NLO electroweak corrections	99
3	Numerical setup	100
3.1	Basic cuts and parameters	100
3.2	Scale and PDF	102
4	Results	103
5	Conclusions and discussions	108
II	Probing the spin correlations of $t\bar{t}$ production at NLO QCD+EW	115
1	Introduction	116
2	Theoretical setup	117
2.1	Reweighting in fixed-order PS point generation	118
2.2	Spin correlation coefficients	121
2.3	Asymmetries	123
3	Numerical setup	124
4	Results	126
5	Conclusion and discussion	131
III	The colour matrix at next-to-leading-colour accuracy for tree-level multi-parton processes	139
1	Introduction	140
2	The colour matrix in the fundamental decomposition	141
2.1	n -gluon amplitude	142
2.2	One $q\bar{q}$ pair and n gluons	147
2.3	Two distinct-flavour $q\bar{q}$ pairs and n gluons	149
2.4	Two same-flavour $q\bar{q}$ pairs and n gluons	153
3	The colour matrix in the colour-flow decomposition	155
3.1	n -gluon amplitude	156
3.2	One $q\bar{q}$ pair and n gluons	157
3.3	Two distinct-flavour $q\bar{q}$ pairs and n gluons	161
3.4	Two same-flavour $q\bar{q}$ pairs and n gluons	166
4	Results	167
4.1	Phase-space symmetrisation	167
4.2	Number of non-zero elements in the colour matrix	170
5	Conclusion	179
A	Data for figures	181
IV	Angular coefficients in $W + j$ production at the LHC with high precision	189
1	Introduction	190
2	Details of the calculations	191
2.1	Definition of the process	191
2.2	Computational set-up	195

2.3	Tools used	195
3	Numerical results	196
4	Conclusion	202
A	Electroweak corrections and decay coefficients	203

Acknowledgements

Foremostly, I would like to thank my supervisor Rikkert. Your support, guidance and patience throughout my doctoral studies have been an important ingredient in producing this work. I greatly appreciate everything I learned from you: starting from computer basics (I remember the day you showed me tab completion in a Linux terminal!) to your most interesting particle physics expertise.

A big help when facing computer as well as physics challenges, came from Davide, Ioannis and Marco. Thank you for answering all my small and big questions about MadGraph5. Many thanks to Andrei, Ioannis, Mathieu and Rene for fruitful collaborations on the works in this thesis and all interesting discussions we had during this time. Further, I am very grateful to Emil, Hans, Kristoffer, Levente, Mattias and Zsófia, for proofreading various parts of this thesis and giving valuable feedbacks.

My days at the department in Lund were made bright by my fellow Ph.D. and postdoc colleagues: Anca, Andrecia, Andrew, Chiara, Harsh, Jasmina, Joan, João, Leif, Mattias, Mårten, Nils, Robin and Torbjörn. Thank you for all our social activities, SET games during fika, fancy lunches, snowman building, Monday junior meetings and discussions on running and races. An additional thank you to Andrew, Emil, Marius, Mattias and Robin for our short exercise sessions every day during some period. For being nice, helpful and always happy office mates, thank you to Andrew, Marius and Mårten. An extra thanks to Andrew for being a good and helpful company on our work trips to Bonn, Zakopane and Paris, and for the short, but fun, physics collaboration we had in the colour project.

Thank you to Lena, Eva and Caroline, who were always fast at helping me with administrative and practical questions; and thank you, Louise, for the help with travel administration and making sure there was always tea in the kitchen.

I would further like to thank my physics teacher in high school, Mats-Olof Söderberg, who, in the last moment, guided me to pursuing my studies in physics instead of mathematics. For Stefan Leupold I am very grateful for introducing me to the world of particle physics and QFT, and later for his guidance, advice and friendship.

Your heartfelt support during these years, Emil, is the spark in this work, it means very much to me. And thank you, Marysia, for your always honest and true friendship. And thank you to all my friends scattered throughout the world. Without friendship in my life I would be nothing but a collection of particles.

Legfontosabban, lélekből hálás vagyok szüleimnek, nővéremnek és nagyszüleimnek, hogy megtanítottak szívből tanulni, komolyan dolgozni és szeretni a munkát. És a munka gyümölcsét Istentől kapott szerénységgel szüretelni.

List of publications

This thesis is based on the following publications:

- I **Electroweak corrections to the angular coefficients in finite- p_T Z -boson production and dilepton decay**
Rikkert Frederix, Timea Vitos
Eur. Phys. J. C **80**, 939 (2020)
e-print: arXiv:2007.08867 [hep-ph]

- II **Probing the spin correlations of $t\bar{t}$ production at NLO QCD+EW**
Rikkert Frederix, Ioannis Tsinikos, Timea Vitos
Eur. Phys. J. C **81**, 817 (2021)
e-print: arXiv:2105.11478 [hep-ph]

- III **The colour matrix at next-to-leading-colour accuracy for tree-level multi-parton processes**
Rikkert Frederix, Timea Vitos
J. High Energ. Phys. **2021**, 157 (2021)
e-print: arXiv:2109.10377 [hep-ph]

- IV **Angular coefficients in $W+j$ production at the LHC with high precision**
Mathieu Pellen, Rene Poncelet, Andrei Popescu, Timea Vitos
Eur. Phys. J. C **82**, 693 (2022)
e-print: arXiv:2204.12394 [hep-ph]

All papers are reproduced with permission of their respective publisher, with minor stylistic changes in the layout and wording.

Works which are not included in the thesis but were published or worked on during the time of my doctoral studies:

- V **Electromagnetic form factors of the transition from the spin-3/2 Σ to the Λ hyperon**
Olov Junker, Stefan Leupold, Elisabetta Perotti, Timea Vitos
Phys. Rev. C **101**, 1, 015206 (2020)
e-print: arXiv:1910.07396 [hep-ph]

VI **W-boson angular coefficients at LHC at high precision**

Timea Vitos

To be published in Proceedings of Science.

e-print: [arXiv:2208.12150](https://arxiv.org/abs/2208.12150) [hep-ph]

VII **Combination of NLO QCD+PS and Sudakov EW corrections via reweighting**

Davide Pagani, **Timea Vitos**, Marco Zaro

In preparation.

Magyar összefoglaló

Az emberiség mai hozzáállása a természettudományhoz egy pár alapfelfogáson épül. Első sorban, azt a jelenséget tartjuk valósnak, ami a természetben megfigyelhető (mert ha a fáról úgy esik le az alma, hogy azt senki sem hallotta, akkor valójában adott-e ki hangot?). Másodszor, ha a valóságban megfigyelték papíron leírhatóak és egy elméletbe foglalhatóak, és leginkább akkor, ha jósló képessége van ennek az elméletnek, akkor célba értünk a kutatott kérdéssel kapcsolatban. Így egyértelművé válik, hogy az egyik alapvető kihívás a mai tudományban, hogy minél *pontosabban* tudjuk megfigyelni a természetet; minél *pontosabb* elméleteket fejlesszünk ki és ezeket minél *pontosabban* tudjuk használni a természet megismerésére. Pontosság.

A természettudományon belül a fizika az élettelen természetet leíró nyelvezetünk. Minden élő szervezet és anyag legkisebb egysége a sejt. Viszont a sejtet képező ennél még kisebb alaprészecskék már — a mai tudomány szerint — élettelen alapegységek, így a fizika, és ezen belül a részecskefizika, alaptörvényeire hallgatnak. Az emberiség mai napig legsikeresebb elmélete az alaprészecskék leírására, a Standard Modell, amely összefoglalja az eddigi ismert és valamilyen formában megfigyelt összes részecskét és a köztük fennálló kölcsönhatásokat.

A Standard Modelltől kiinduló számítások sokrétegű nehézséggel járnak. Ezért a pontos leírása és a számítógép segítségével kiszámolt eredményei egy egész külön ágat alkotnak a részecskefizika világán belül, a precíziós (pontos) fenomenológiát. A jelen doktori dolgozat, a Standard Modell pontosításához valamint a részecskefizikán belüli kísérletekhez való összehasonlításának lehetőségéhez járul hozzá.

A bevezetőt egy jogos kérdéssel zárom. Miért érdekl az emberiséget ez a sok alaptudomány? Kinek vagy minek teszünk az ezzel való foglalkozással jót és a társadalmat hogyan mozdítjuk előre? A válasz egy egyszerű szóban rejlik: felelősség. Hiszen a világot alkotó csodák véget nem érve kerülnek eléink felderítésre. Ezek közül pedig a legnagyobb csoda az, hogy Isten minket annyi képességgel és érdeklődéssel ajándékozott meg, hogy ezt mind felderíthessük.

Éljünk ezzel az ajándékkal.

Populärvetenskaplig sammanfattning på svenska

Vad är det som hindrar oss att falla rakt igenom stolen när vi sätter oss? Och varför kan vi hålla en temugg i handen utan att krama sönder den? Svar på dessa och liknande frågor får vi genom att undersöka de allra *minsta* beståndsdelarna i materia som bildar världen. Varför hålls planeter kvar i sina omloppsbanor och varför blir stjärnor till? Det är frågor som rör de allra *största* objekten i vår värld. Oavsett om det handlar om mycket stora eller mycket små längdskalor, är människan nyfiken på *varför*.

Nyfikenhet har alltid drivit människan mot att upptäcka nya fenomen. Men vad menas egentligen med nya fenomen? Det måste vara nytt i jämförelse med något annat. Vi kan knappast påstå att vi upptäcker något nytt när man uppfinner hjulet igen, men på sin tid var det sannerligen en genomträngande upptäckt. För att verkligen kunna säkerställa att det som har upptäckts är nytt, måste vi lika noggrant veta vad vi redan vet och vad vi förväntar oss av omvärlden utifrån den befintliga kunskapen. I många fall kan detta vara en mindre självklar uppgift än vad det låter som.

Fysik är i synnerhet alltid driven åt att förstå hur materia växelverkar. Låter vi temuggen stå på bordet utan någon yttre inverkan kommer den att stå kvar en väldigt lång tid, och ingen intressant fysik verkar hända med den. Men efter många tusen år börjar den sönderfalla: detta fenomen kan på den "rätta" längdskalan — på partiklarnas nivå — beskrivas av hur de allra minsta beståndsdelarna av temuggen växelverkar med varandra och omgivningen. Oavsett längdskala, berör fysik alltid materiales samspel och dess konsekvenser och det är denna dynamik vi vill komma åt i forskning.

Med denna inledning kan vi sammanfatta ämnet i denna avhandling och förstå dess vikt inom partikelfysik. Den nuvarande teorin i partikelfysik, som har utvecklats gradvis under 1900-talet, kallas *standardmodellen* och den har kunnat beskriva fenomen som upptäckts vid energirika partikelkollisioner med häpnadsväckande bra precision. Men ändå misslyckas standardmodellen att ge svar på många frågor (som existensen av mörk materia) och dessa kräver nya modeller och nya sätt att tänka på. I denna avhandling undersöker vi den befintliga kunskapen om partiklarnas dynamik med hög precision baserad på standardmodellen. Detta utförs för olika händelser av partikelkollisioner som sker vid LHC (Large Hadron Collider) som är dagens främsta experiment för partikelfysik. Avhandlingens forskning bidrar således till att bättre kunna förstå och utnyttja data som samlas vid partikelexperiment, med förhoppning om att upptäcka fenomen som sträcker sig utöver standardmodellen och med det kunna beskriva obesvarade fenomen i vår natur.

Introduction

“Tonight I can go to sleep with the thought: the Himalayas became one dust grain taller today.”

— translation from Reményik Sándor

This doctoral thesis focuses on the study of fundamental, indivisible pointlike particles and the particles with (very small) spatial extension formed by them. In this field of science, the interactions of these particles are investigated at both low and high energies compared to the particle rest masses. High energy collisions of particles are investigated at large particle physics facilities, out of which the largest today is CERN, which hosts the Large Hadron Collider (LHC), colliding protons (pp collisions) and heavy nuclei. This thesis and the four papers included in it are concerned with pp collisions, with a focus on a few processes and measurements related to these: the Drell-Yan process, the production of a top quark pair, and multi-jet processes.

The aim of this introductory chapter is to provide sufficient background information for understanding the papers included in the thesis. For those who are interested in a shorter, less formal, but complete introduction, Section 1 is dedicated to precisely this purpose. A more formal development of the introduction is presented in the following sections:

- Section 2 covers some essentials of theoretical particle physics and concepts within particle physics phenomenology.
- Section 3 discusses Monte Carlo computer-based simulations of particle interactions and related topics.
- Section 4 provides a slightly more experimentally-oriented background, with a focus on the LHC program and presents the processes investigated in the papers.

These sections can be read in any order, as they provide complementary information. Finally, the introduction is concluded with some final words and outlook in Section 5, before making a transition to the papers of the thesis by presenting a summary of them and my contributions to each in Section 6.

I Basic scientific introduction

“Nature is an infinite sphere of which the center is everywhere and the circumference nowhere.”

— Blaise Pascal

The aim of particle physics is to study the interactions of fundamental particles. It is important to note that these particles are not like everyday particles with finite size; in fact, we do not know if they have any spatial extension at all. What is meant by particles in this setting are those fundamental entities which emerge at the smallest scales and are not further composed of even smaller entities. And how do we detect and realize these fundamental particles? To understand this, we draw a parallel between classical physics and particle physics.

In the world around us, the motion of an object with mass m having a force $\mathbf{F}(t)$ exerted on it can be predicted by Newton’s law $\mathbf{F}(t) = m \mathbf{a}(t)$ thereby obtaining a (time-dependent) acceleration $\mathbf{a}(t)$. The particle’s motion is then entirely determined (with some suitable initial conditions), allowing us to calculate its velocity $\mathbf{v}(t) = \int \mathbf{a}(t)dt$ and its position $\mathbf{s}(t) = \int \mathbf{v}(t)dt$ at any time t . This, so far, is all described with classical Newtonian physics. In particle physics, the goal is analogous: we want to understand how particles are affected by external forces. For instance, in electromagnetism, electrically charged objects exert forces on other charged objects. In other words, matter interacts through the electromagnetic force field. Similarly, at the particle level, we investigate how fundamental particles affect each other through various force fields.

In the everyday world, we can perform a wide variety of experiments on objects, such as dropping an apple from a height to probe the gravitational field, or giving it a push, or even cutting it into pieces. In particle physics, however, there are limitations to the types of experiments we can conduct. The reason for this is that we do not operate on the length scales of these particles. We can reach their level in research only by means of particle colliders, which are quite limited in their setup. Particle colliders accelerate particles to extremely high speeds to achieve high energies. This way we can probe the fundamental particles, and not only those which naturally occur in our world, but also the rare ones. This restricts us to two main types of experiments: examining how two (or more) particles interact in a collision or how a single particle decays. In the former case, either fixed-target experiments are used, in which one particle is at rest during the collision, or collider experiments, in which both are in motion. In both cases, the objective remains to calculate the probability that an interaction of some certain type takes place in the collision.

In classical Newtonian mechanics, it is well determined how an apple will move once it is given a push in some direction. Particles are, on the other hand, described by quantum mechanics, where the path taken by the object cannot be determined perfectly in advance

with 100% certainty even with perfect knowledge of the object and the initial conditions. Instead, it is only possible to compute the probability that the object will move in various paths from one (well-defined) point to the other (well-defined) point. The final probability of the particle to reach the second point is obtained by summing and averaging over all possible paths between the initial and final points. For this reason, the calculations in quantum mechanics often become more complex and time-consuming than those in Newtonian mechanics, even though the concepts of force and resulting motion remain the same.

This finally leads us to the concept of cross sections in particle physics. The cross section for an interaction is the probability of some set of particles to produce some other (or the same) set of particles under specific conditions, such as energy of the collision, particle types, and temperature. The cross section is generally denoted with $\sigma(\{i\} \rightarrow \{f\})$, where $\{i\}$ is the initial set of particles and $\{f\}$ is the final set of particles. To be able to calculate this probability, we need to know the forces acting between the particles: in analogy to Newton's law, we need to know $F(t)$. However, determining which forces are included is not trivial, as various models include different types of fundamental forces. One such model, the Standard Model, includes three types of forces: the weak interaction, the strong interaction and the electromagnetic interaction. It omits the description of gravity, a very basic force in our everyday world — this is in fact one of the (many) limitations of this model. But despite its flaws, this model has reached a remarkable agreement with observations at particle collisions. Consequently, it serves as a baseline for experiments, while active research seeks models describing and including further phenomena, such as gravity.

With this general introduction, we can now describe the fundamental particles and interactions that are contained in the Standard Model. The electromagnetic force affects charged *leptons*, *quarks* and two charged weak *bosons*; the weak interaction affects charged leptons and neutral leptons (*neutrinos*) and quarks and three weak bosons (two charged and one neutral); and finally the strong interaction affects quarks and *gluons*. These particles are divided into matter particles and force carrier particles: matter particles are the leptons and quarks (collectively known as fermions), while the force carriers (collectively known as bosons) are the three weak bosons, the photon and the gluon. The photon, a neutral and massless particle, interacts only with charged fermions in this model, while the gluon interacts also with other gluons. The leptons and quarks are grouped in three sets, or generations, with increasing mass scales. Each particle also has a corresponding anti-particle (which might be itself) that has the same mass and other internal properties, but opposite charges. Anti-particles for quarks and neutrinos are denoted with a bar (for example \bar{b} represents a bottom anti-quark and $\bar{\nu}_\tau$ an anti-tau-neutrino), while the anti-particles for the leptons and the charged bosons are denoted with the opposite charge sign (e^+ for the electron anti-particle, the positron). In addition to these particles, there is another one, the Higgs boson, that interacts with all particles which have mass (or more precisely, the

particles which interact with the Higgs boson acquire mass). The Higgs boson also plays a role in reducing the three forces mentioned above (the strong, weak and electromagnetic forces) to effectively only two: the quantum chromodynamic (QCD) interaction (describing the strong interaction) and the electroweak (EW) interaction. The particles and the three basic interactions in the Standard Model are depicted in Figure 1.

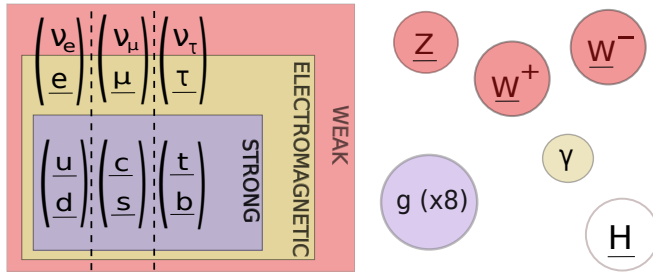


Figure 1: Schematic content of the Standard Model: the particles in boxes are fermions, while those in circular shapes are bosons, the force carriers. The red indicates the weak interaction, the yellow indicates the electromagnetic interaction and finally the purple indicates the strong interaction. The Higgs boson interacts with the underlined particles. The dashed lines separate the fermions into the three generations.

Only three of the mentioned particles occur naturally: the electron (orbiting the atomic nuclei), and the up and down quarks (forming the protons and neutrons in the atomic nuclei). All other particles can be created only for short times at high energy colliders. The spatial size of the fundamental particles is portrayed in Figure 2, comparing the sizes of the building blocks of a plant in our everyday world. The size of the other fundamental particles are comparable to the size of the up and down quarks (valence quarks) in the proton, less than 10^{-18} m.

The mathematical language for the description of the interactions is quantum field theory. Within this framework, the forces in the Standard Model are represented in a function called the Lagrangian \mathcal{L} . This function includes terms that describe interaction points between particles. The strengths of these interactions are parametrized by so-called coupling constants. With the Lagrangian as the foundation, Richard Feynman developed a convenient tool in 1948 for the evaluation of cross sections, based on a set of rules. These are known as Feynman rules, and they structure the computation of cross sections in a neat fashion, although they can produce tedious and cumbersome expressions to evaluate. The Feynman rules are based on perturbation theory, which is, in principle, a simple tool that utilizes the Taylor expansion of functions. Specifically, given some function $f(\epsilon, x)$ which

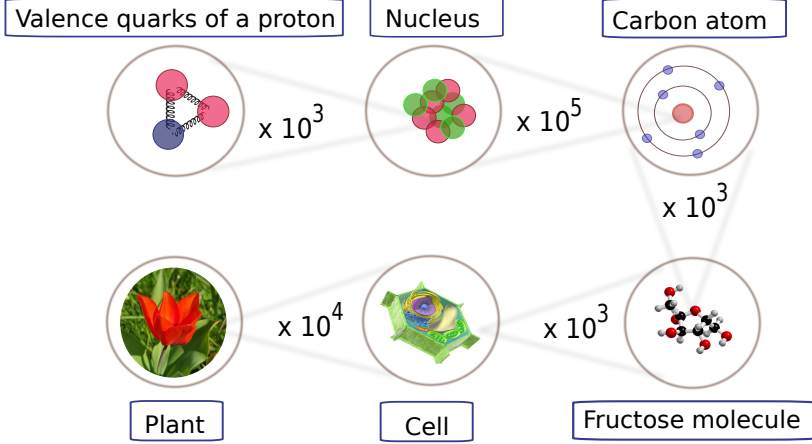


Figure 2: The size of the valence quarks in a series of magnifications starting from a plant (of order 1 m) in our everyday world.

is dependent on x and some small parameter ϵ , we Taylor expand the function,

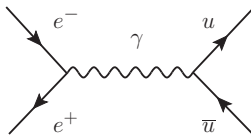
$$f(x, \epsilon) \approx \underbrace{f(x, \epsilon = 0)}_{\text{LO}} + \underbrace{\epsilon \frac{df}{d\epsilon} \Big|_{\epsilon=0}}_{\text{NLO}} + \underbrace{\frac{1}{2} \epsilon^2 \frac{d^2 f}{d\epsilon^2} \Big|_{\epsilon=0}}_{\text{NNLO}} + \mathcal{O}(\epsilon^3). \quad (1)$$

When this is applied to the Lagrangian \mathcal{L} of the Standard Model, the small expansion parameters are the coupling constants: α_s (for the strong interaction) and α (for the electroweak interaction), which are indeed small, $\alpha_s \approx 0.1$ and $\alpha \approx 0.01$. With this expansion at hand, we can keep only the first few terms in the expansion, as the impact of higher order terms become negligible. By truncating at higher and higher orders in α and α_s one increases the precision of the cross section computation. From this arises (as the equation indicates) the terminology of leading order (LO) which is the lowest (non-vanishing) order in the couplings, the next-to-leading order (NLO), and so on (NNLO, N³LO, ...). When performing a Taylor expansion in both of the couplings simultaneously, the expansion above is slightly more involved,

$$f(x, \alpha_s, \alpha) \approx \alpha_s^{c_1} \alpha^{c_2} \left(\underbrace{f(x, \alpha_s = 0, \alpha = 0)}_{\text{LO}} + \underbrace{\alpha_s \frac{df}{d\alpha_s} \Big|_{\alpha_s=0, \alpha=0}}_{\text{NLO QCD}} + \underbrace{\alpha \frac{df}{d\alpha} \Big|_{\alpha_s=0, \alpha=0}}_{\text{NLO EW}} + \mathcal{O}(\alpha_s \alpha) \right), \quad (2)$$

where the leading-order term is the first non-vanishing term in the expansion, and any potential common factor of $\alpha_s^{c_1} \alpha^{c_2}$ of the couplings is factorized. This introduces the important term of NLO electroweak (NLO EW) corrections, which is the primary focus in three papers of this thesis. Higher order terms can have pure QCD origin, pure EW origin, or be mixed terms.

Feynman envisioned all these contributions in the expansion, term by term, as diagrams. In Feynman diagrams, incoming particles appear on one side, and outgoing on the other. Particles are depicted as lines, and are connected in all possible ways following the Feynman rules (originating from the Lagrangian \mathcal{L}). These rules assign mathematical expressions to the lines and vertices, allowing the calculation of the values of the diagrams. We exemplify this by drawing the leading-order diagram for the $e^+e^- \rightarrow u\bar{u}$ process,



which is indeed the only possible diagram we can draw at leading order, based on the Feynman rules for this process within the Standard Model. According to these rules, each vertex with one photon and two charged particles translates into a factor of $i\sqrt{Q4\pi\alpha}\gamma^\mu$, where Q is the fractional charge of the particle compared to the charge of the charged leptons (e) and γ^μ is a set of constant-valued matrices. An internal line appearing inside the diagram is called a propagator. For the photon propagator in the above diagram, we assign the factor $\frac{-i}{E^2+i\epsilon}$, where E is the energy of the photon and ϵ a small number (which is set to zero after all computations are finished, but is needed for proper bookkeeping of the calculations). Considering that the u quark has electric charge $\frac{2}{3}e$, the diagram evaluates to

$$\begin{array}{c} \text{Diagram} \end{array} \sim i\sqrt{4\pi\alpha}\gamma^\mu \frac{-i}{E^2+i\epsilon} i\frac{2}{3}\sqrt{4\pi\alpha}\gamma_\mu. \quad (3)$$

The diagrams enter the cross section as the square of the sum of all possible diagrams. As such, this diagram squared contributes at order $\mathcal{O}(\alpha^2)$, to the leading-order term of the Taylor expansion of this process.

To put this background into context, the processes that are targeted in the papers of the thesis are now introduced. The first process is the neutral-current Drell-Yan process, where two protons collide to produce two charged light leptons (e^+e^- or $\mu^+\mu^-$) in the final state. This process has been crucial for the identification of the fundamental particle content of the proton and the verification of the strong interaction. The cross section, or specifically its dependence on the directions in which the outgoing charged leptons leave the interaction point, is parametrized by a set of decay coefficients, calculated with perturbation theory and

measurable as observables at particle detectors. Paper I in this thesis presents the NLO EW corrections to these coefficients, which is an important contribution to the understanding of the Standard Model precision predictions for this important process at the LHC.

A closely related process is the charged-current Drell-Yan process, where one charged lepton and the corresponding neutrino is created in the collision ($e^\pm \bar{\nu}_e$ or $\mu^\pm \bar{\nu}_\mu$). Again, a set of decay coefficients parametrizes the cross section. This process is challenging to measure because the neutrino, which only interacts through the weak interaction, escapes all detectors. Consequently, the precision predictions for the decay coefficients have been previously missing, and for this reason, in paper IV we present NNLO QCD and NLO EW corrections to these observables for the first time, in hope of experiments achieving high-precision measurements of them in the near future.

The third process of interest to this thesis is the production of a $t\bar{t}$ pair, in which the heavy top quark (the heaviest particle in the Standard Model) and its anti-particle are produced. Of special interest related to this process is how the spin (an internal property of each particle) is correlated between the two produced quarks and the particles which they decay into. Paper II investigates the NLO EW corrections to the spin correlations and related observables for this process with leptonic decays of the top quarks.

Finally, paper III targets a rather different type of process at the LHC: multi-jet events. These are abundant processes that appear in almost all process investigations at the LHC and are essentially a QCD background to the interesting signals which are being extracted from data. The strong interaction is in some aspect mathematically the most complicated interaction to compute. Therefore, when a large number of strongly interacting final state particles are present, performing computations at high precision becomes very challenging. In paper III we propose a new approach to the computation of these processes, laying the theoretical foundation for the implementation of a new, improved computational toolkit.

This concludes the basic scientific introduction with which the main essence of the papers in this thesis can be understood. A short summary of the publications and my contributions to them are presented in Section 6. The remaining of this introductory chapter presents the background in more detail.

2 Introducing particle physics phenomenology

“Nothing in life is to be feared; it is only to be understood.”

— Marie Curie

The physics of fundamental particles is described within the framework of quantum field theory, which is the combination of special relativity, field theory and quantum mechanics. In this theory, particles are described as excitations of fields. Various models exist, describing different interactions between these fields, but the one model which has been very successful in precisely describing phenomena in nature is the Standard Model, which is the focus of this thesis. In order to introduce and properly appreciate the Standard Model, in this section first some important ingredients in quantum field theory are presented. Then, the gauge group symmetries and the symmetry group for the Standard Model are introduced. Following this, the concept of cross sections in particle physics is discussed, before returning to some technicalities of quantum field theory. With these general aspects introduced, the free parameters of the Standard Model, the parton distribution functions and their evolution and finally, the colour expansion of matrix-elements are discussed.

2.1 The successful Standard Model

First, some basic concepts of quantum field theory are described. A complete introduction to special relativity, group theory, quantum mechanics and field theory is out of scope for this thesis. Throughout the thesis, natural units are used, which is customary in this area of physics, in which c (speed of light in vacuum) and \hbar (Planck’s constant) are set to 1. In these units, mass and momentum are of the same dimension as energy (expressed in particle physics most often in units of electronvolts, eV) and time and distance of the dimension of inverse energy.

Quantum field theory

In relativistic field theory, the dynamical degrees of freedom are fields $\Psi_i(x)$ which are functions of the position \mathbf{x} and time t , combined in spacetime points $x = (t, \mathbf{x})$. The dynamics of systems within quantum field theory is described by minimizing the action (here presented in a four-dimensional spacetime)

$$S = \int d^4x \mathcal{L}(\Psi_i(x), \partial_\mu \Psi_i(x), \dots) \quad (4)$$

with the Lagrangian density \mathcal{L} describing the dependence on the fields $\Psi_i(x)$ and on their (partial) derivatives $\partial_\mu \Psi_i(x)$ (and possibly on higher order derivatives). Minimizing this

scalar action results in equations of motion, which determine the classical dynamics of the fields. If the fields are quantized, we speak of a quantum field theory. What constrains the dynamics in a quantum field theory is thus fully encoded in the Lagrangian, which indeed is the central ingredient in any theoretical computation. In particle physics, particles are described via excitations of particle fields, meaning that each particle type is described by a quantum field reflecting the properties of the particle. These properties of the particles and fields are given by the symmetries which the system and the Lagrangian obey. Different symmetries lead to different conserved quantities and different charges, through Noether's theorem.

One of the symmetries of the Standard Model is the Poincaré symmetry, which is the group describing the symmetries of systems obeying special relativity. This group consists of three boosts (in spacetime), three rotations, and four spatial plus temporal translations. The fields on which the Lagrangian depends transform under this group in a way that leaves the total contribution invariant. This defines scalars, which are invariant under Poincaré transformations; and spinors and vector fields, fields which transform in a well-defined way under this group.

The spin \mathbf{S} of each field is defined by its transformation under the Poincaré group. The scalar fields have zero spin; fermions (spinor fields) have half-integer spin, and bosons (vector fields) have integer spin (also scalar fields are bosons but with integer spin zero). Particles described by the Standard Model are spin- $\frac{1}{2}$ ($|\mathbf{S}|=\frac{1}{2}$), spin-0 ($|\mathbf{S}|=0$) or spin-1 ($|\mathbf{S}|=1$) particles. The quantum-mechanical projection of the spin vector on the third component defines the spin state (polarization) and can take the values

$$S_z \in \{-|\mathbf{S}|, -|\mathbf{S}| + 1, \dots, |\mathbf{S}| - 1, |\mathbf{S}|\}.$$

The projection of the spin state along \mathbf{p} , the direction of motion, defines the particle's helicity, given by the helicity operator

$$h = \frac{\mathbf{S} \cdot \mathbf{p}}{|\mathbf{p}|}, \quad (5)$$

which for spinor fields either gives a positive helicity or negative helicity. This operator has a well-defined eigenvalue for massless particles; however, for massive particles, this quantity becomes Lorentz-frame-dependent. Instead, one defines chirality, which is the transformation property of the particle under the Poincaré group. For spinors, the left- and right-handed parts are obtained with the chirality projection operators P_L, P_R , defined by their action on the spinor fields $\psi(x)$ as

$$\psi_L(x) = P_L\psi(x) \quad \text{and} \quad \psi_R(x) = P_R\psi(x), \quad (6)$$

with projection properties for the operators,

$$P_{R/L}^2 = P_{R/L}, \quad P_{L/R}P_{R/L} = \mathbf{0}, \quad P_R + P_L = \mathbf{1}. \quad (7)$$

Hence, the spinor field $\psi(x)$ describing a spin- $\frac{1}{2}$ fermion is a four-component object (expressed as Dirac spinors), with two components, the left-handed ($\psi_L(x)$) and right-handed ($\psi_R(x)$) chiral parts. For massless particles, the definitions of chirality and helicity are equivalent.

Beside the Poincaré transformation, another important set of group transformations is the Lie group $SU(n)$, called the special unitary group. This is the group of $n \times n$ matrices U which are unitary, $U^{-1} = U^\dagger$, and have determinant $\det(U) = 1$. The unitary group $U(n)$ defines the same group but without the constraint of a unit determinant. Groups with $n > 1$ are non-abelian groups, meaning that two group elements do not commute, $U_1U_2 \neq U_2U_1$. Group transformations are understood as the action of the elements on a set of objects.

One can linearize Lie groups with the exponential map

$$\exp(A) = \sum_{n=0}^{\infty} \frac{A^n}{n!} \quad (8)$$

such that the elements of the Lie group $U \in SU(n)$ are written as

$$U = \exp(ic_i Y_i) \quad (9)$$

with real constants c_i and $n^2 - 1$ traceless generators Y_i , which must be hermitian by construction. The space spanned by $c_i Y_i$ is the Lie algebra of the group and the generators satisfy the commutation relation

$$[Y^a, Y^b] = is^{abc} Y^c, \quad (10)$$

with the structure constants s^{abc} forming a totally anti-symmetric tensor specific to the group. While abelian theories have $s^{abc} = 0$, non-abelian theories have in general non-vanishing structure constants.

Related to group transformations are representations. Representations are vector spaces which transform under the elements of the Lie group, and which remain closed under the transformation. Linear representations are those where the elements in the group g can be mapped to a matrix $M(g)$ and the set of objects they act on are column-vectors. Two main types of linear representations of $U(n)$ and $SU(n)$ are considered in this work: the fundamental and the adjoint representation. In the fundamental representation, the mapped matrices are the group elements themselves, $M(g) = g$. In the adjoint representation, the column-vectors which the map $M(g)$ acts on is the Lie algebra $c_i Y_i$ itself.

After this small detour through group theory, we return now to Lagrangians and field theory. The free field Lagrangian for a complex scalar field $\phi(x)$ with mass m is given by

$$\mathcal{L} = \partial_\mu \phi^*(x) \partial^\mu \phi(x) - m^2 \phi^*(x) \phi(x), \quad (11)$$

the first term being the kinetic term, and the second being the mass term. When the field is real, both terms acquire a factor $\frac{1}{2}$ to account for symmetry. The free field Lagrangian for a spinor field of mass m is generally given by

$$\mathcal{L} = \bar{\psi}(x)(i\gamma^\mu\partial_\mu - m)\psi(x) \quad (12)$$

where $\bar{\psi}(x) = \psi^\dagger(x)\gamma^0$, where γ^0 is one of the gamma matrices γ^μ . With the projection relations, one obtains that the spinor mass term can be written as

$$m\bar{\psi}\psi = m\bar{\psi}_L\psi_R + m\bar{\psi}_R\psi_L. \quad (13)$$

Both of the Lagrangians above are invariant under a global U(1) transformation of the fields,

$$\Psi(x) \rightarrow U\Psi(x) = e^{iq}\Psi(x) \quad , \quad U \in \text{U}(1) \quad (14)$$

with the (spacetime-independent) real parameter q . By demanding a local U(1) invariance of the Lagrangian (upgrading $q \rightarrow q(x)$), the kinetic term breaks its invariance under this symmetry, while the mass term remains invariant. This issue is resolved by introducing a connection field A_μ and a covariant derivative D_μ defined by the replacement of the usual partial derivative

$$\partial_\mu \rightarrow D_\mu = \partial_\mu - igA_\mu, \quad (15)$$

introducing a coupling strength g , and with a well-determined transformation of the connection field,

$$A_\mu \rightarrow A_\mu + \frac{1}{g}\partial_\mu q(x), \quad (16)$$

leading to local gauge-invariant free field Lagrangians for scalars and spinors. The commutator of the covariant derivative is defined by introducing a field strength tensor $F_{\mu\nu}$ for each connection field in the derivative,

$$[D_\mu, D_\nu] = igF_{\mu\nu}. \quad (17)$$

The covariant derivative introduces a coupling with size g between the field Ψ and the connection field through the kinetic term. As we will see, connection fields are the boson fields which are the mediators of the interactions within the Standard Model.

Introducing the Standard Model

The Standard Model includes three fundamental interactions: the strong interaction, which is responsible for keeping protons and neutrons in bound states in the nuclei; the weak

interaction, which is the mediating force for nuclear decays; and the electromagnetic interaction, which is the well-known relativistic combination of the electric and magnetic interactions.

The Standard Model incorporates two types of particles: fermions and bosons. The fermions, which are spin- $\frac{1}{2}$ particles, are also called matter particles, as they obey the Pauli exclusion principle, in which fermions cannot be packed infinitely close. These particles come in two groups: the leptons and the quarks. The leptons are those fermions that do not interact via the strong interaction, and the quarks are those that do. Each of the matter particles have a corresponding anti-particle, which form anti-matter in the universe. The second type of particles in the Standard Model are the bosons: these are the mediators of the interactions, although some of these interact themselves through those same interactions. The interactions are described by gauge groups, and the gauge bosons are the connection fields which are needed for local gauge invariance.

The local gauge symmetry group of the Standard Model consists of three unitary groups,

$$SU(3)_C \times SU(2)_L \times U(1)_Y \quad (18)$$

with the colour gauge group $SU(3)_C$ describing the strong interaction, formulated within the framework of quantum chromodynamics (QCD); the weak isospin group $SU(2)_L$ and the weak hypercharge $U(1)_Y$ gauge group together combine into the electroweak (EW) force, the unification of the weak and the electromagnetic interaction.

The $SU(3)$ and $SU(2)$ are non-abelian symmetry groups. The non-abelian nature of gauge groups yield slightly different transformations of fields than the one presented for $U(1)$ transformations. The general gauge transformation is

$$\Psi(x) \rightarrow e^{iq^a(x)t_a} \Psi(x), \quad (19)$$

where the t_a span the Lie algebra group. For the $SU(3)_C$ gauge group, the Lie algebra is

$$[T^a, T^b] = if^{abc}T^c, \quad (20)$$

where the T^a are proportional to the Gell-Mann matrices λ^a , and the f^{abc} are the anti-symmetric structure constants. For the $SU(2)_L$ gauge group, the Lie algebra is

$$[\tau^a, \tau^b] = i\epsilon^{abc}\tau^c, \quad (21)$$

with the τ^a generators being proportional to the Pauli matrices σ^i , and ϵ^{abc} is the Levi-Civita tensor. Although there are multiple bases for the group structure description, there are some constants which often appear in computations and which are basis-independent. These are, for a general $SU(n)$ gauge group with the $n^2 - 1$ fundamental generators Y^i

and structure constants s^{abc} , defined as

$$\begin{aligned}
\sum_{a=1}^{n^2-1} (Y^a Y^a)_{ij} &= \delta_{ij} C_F, & C_F &= \frac{n^2-1}{2n}, \\
\sum_{i,j=1}^n Y_{ij}^a Y_{ji}^b &= \delta^{ab} T_F, & T_F &= \frac{1}{2}, \\
\sum_{a,b=1}^{n^2-1} s^{abc} s^{abd} &= \delta^{cd} C_A, & C_A &= n,
\end{aligned} \tag{22}$$

where the summation sign is shown explicitly to indicate the number of terms in the sums. Here, C_A and C_F are called the quadratic Casimirs for the fundamental and adjoint representations respectively, and T_F is the index of a representation (in this case the fundamental representation). For the Standard Model colour gauge group with $n = 3$, we have $C_F = \frac{4}{3}$ and $C_A = 3$.

A summary of the ingredients (some of which will be introduced later in the section) in the Standard Model Lagrangian is presented in Table 1. In the table, the important gauge couplings are introduced: g_1 for the strong interaction, g_2 for the weak isospin group and g_3 for the hypercharge group. The matter particles in the Standard Model are grouped into three generations with a mass hierarchy. Within each generation, the fermions are structured according to their transformation properties with respect to the three gauge groups. The weak $SU(2)_L$ gauge group acts only on left-handed particles, meaning that this symmetry is maximally parity-violating. Hence, within each generation, the fermions are classified into five groups: two doublets Q_u, L_e (one quark and one lepton doublet including the left-handed eigenstates) and three right-handed singlets e_R, u_R, d_R (one lepton singlet and two quark singlets), transforming under the weak isospin group according to

$$\begin{aligned}
Q_u &\rightarrow U Q_u, & L_e &\rightarrow U L_e, \\
e_R &\rightarrow e_R, & u_R &\rightarrow u_R, & d_R &\rightarrow d_R,
\end{aligned} \tag{23}$$

with $U \in SU(2)_L$ and the subscripts L, R denote the left- and right-chirality eigenstates. The doublets contain the left-handed states,

$$Q_u = \begin{pmatrix} u_L \\ d_L \end{pmatrix}, \quad L_e = \begin{pmatrix} \nu_L \\ e_L^- \end{pmatrix}, \tag{24}$$

where the upper element has weak isospin charge I_3 of $+1$ and the lower element has weak isospin charge -1 . The charges under the electromagnetic interaction, Q , are also different within the doublets: all $+1$ isospin quarks carry a charge of $\frac{2}{3}e$, all the -1 isospin quarks carry a charge of $-\frac{1}{3}e$, while the charged leptons carry the elementary charge $-e$ and the neutrinos are neutral. The anti-particles have opposite charges regarding all the

Table 1: The Standard Model Lagrangian in the symmetric basis divided into separate contributions. The gauge boson fields in the covariant derivative act on those matter fields which are not singlets under the corresponding gauge group.

Fermion kinetic	$\bar{\psi}_f \gamma^\mu D_\mu \psi_f, \quad f \in F$
Covariant derivative	$D_\mu = \partial_\mu - ig_1 \frac{\lambda^a}{2} G_\mu^a - ig_2 \frac{\sigma^i}{2} W_\mu^i - ig_3 \frac{Y}{2} B_\mu$
SU(3) _C kinetic	$-\frac{1}{2} \text{Tr}[G_{\mu\nu} G^{\mu\nu}]$
SU(2) _L × U(1) _Y kinetic	$-\frac{1}{2} \text{Tr}[W_{\mu\nu} W^{\mu\nu}] - \frac{1}{4} B_{\mu\nu} B^{\mu\nu}$
Higgs sector	$\frac{1}{2} D_\mu \phi^\dagger D^\mu \phi - \mu^2 \phi^\dagger \phi + \frac{\lambda}{4} (\phi^\dagger \phi)^2$
Fermions F	$[L_e, e_R, Q_u, u_R, d_R] \quad (\text{first generation})$ $[L_\mu, \mu_R, Q_c, c_R, s_R] \quad (\text{second generation})$ $[L_\tau, \tau_R, Q_t, t_R, b_R] \quad (\text{third generation})$
Yukawa couplings	$g_e \bar{L}_e \phi e_R + g_u \bar{Q}_u \phi_c u_R + g_d \bar{Q}_u \phi d_R$ $g_\mu \bar{L}_\mu \phi \mu_R + g_c \bar{Q}_c \phi_c c_R + g_s \bar{Q}_c \phi s_R$ $g_\tau \bar{L}_\tau \phi \tau_R + g_t \bar{Q}_t \phi_c t_R + g_b \bar{Q}_t \phi b_R$

interactions. All matter particles and their masses are listed in Table 2. We note that of all the particles present in the Standard Model (including the massive bosons), the top quark is the heaviest with a mass of ~ 173 GeV.

The Lagrangian presented up to now is the classical version of the Standard Model, with a gauge freedom in the symmetries. As a quantum field theory, the gauge has to be fixed and the fields get quantized. This gauge choice introduces further fields, called Faddeev-Popov ghosts [1]. For the current introduction, the classical Lagrangian is adequate.

Table 2: List of massive particles in the Standard Model and their absolute and relative masses compared to the electron mass. *The values reported for the quarks are estimates from the ($\overline{\text{MS}}$) scheme at renormalization scale $\mu = 2 \text{ GeV}$ for the light quarks (u, d, s) and the running value for the b, c quarks, and direct measurement of top quark mass. Values taken from the 2020 PDG report [2].

Lepton masses			
Electron	e	0.510 MeV	$1 \times m_e$
Muon	μ	106 MeV	$210 \times m_e$
Tauon	τ	1.78 GeV	$3490 \times m_e$
Quark masses*			
Up	u	2.16 MeV	$4 \times m_e$
Down	d	4.67 MeV	$9 \times m_e$
Strange	s	93 MeV	$180 \times m_e$
Charm	c	1.27 GeV	$2490 \times m_e$
Bottom	b	4.18 GeV	$8200 \times m_e$
Top	t	172.76 GeV	$339000 \times m_e$
Gauge boson masses			
W -boson	W^\pm	80.38 GeV	$158000 \times m_e$
Z -boson	Z	91.19 GeV	$179000 \times m_e$
Higgs boson	H	125.1 GeV	$245000 \times m_e$

The QCD sector

The colour gauge group $\text{SU}(3)_C$ gives rise to 8 ($= 3^2 - 1$) gluon fields G_μ^a , $a = 1, \dots, 8$, which we combine into a single gluon field $G_\mu = G_\mu^a \frac{T^a}{2}$. The related field strength tensor is

$$G_{\mu\nu} = \left(\partial_\nu G_\mu^a - \partial_\mu G_\nu^a + g_1 f^{abc} G_\mu^b G_\nu^c \right) T^a, \quad (25)$$

see Table 1. Similarly to how the left-handed fields are combined into doublets under the weak isospin gauge group, quarks are placed in triplets (in the fundamental representation) under the colour gauge group. The three charges are named red, blue and green. The colour gauge group is discussed in more detail when introducing colour expansions in Subsection 2.6.

The electroweak sector

The local gauge symmetry group for the Standard Model undergoes spontaneous symmetry breaking (SSB), in which the electroweak sector of the gauge group is broken as

$$SU(3)_C \times SU(2)_L \times U(1)_Y \xrightarrow{\text{SSB}} SU(3)_C \times U(1)_{\text{QED}} \quad (26)$$

resulting in the strong interaction and the electromagnetic interaction, described by quantum electrodynamics (QED), and the weak vector bosons acquiring mass terms in the Lagrangian.

A general mass term for spinor fields, $m\bar{\psi}_R\psi_L$, is not invariant under the weak isospin group, as the left- and right-handed fields transform differently under the $SU(2)_L$ gauge group. Thus, spinor mass terms can not be present in the Lagrangian before symmetry breaking. In a minimal extension of the unbroken Standard Model, the Brout-Englert-Higgs mechanism is introduced, in which a $SU(2)_L$ doublet complex scalar field $\phi(x)$ is added to the theory, with a kinetic term and a cubic and quartic self-interaction terms (see Table 1). The field acquires a vacuum expectation value, breaking its symmetry to a specific value of

$$\phi_0 = \begin{pmatrix} 0 \\ \frac{v}{\sqrt{2}} \end{pmatrix} \quad (27)$$

which introduces the radial excitation around this minimum as the Higgs field H defined for the second component of the $\phi(x)$ field, $\frac{1}{\sqrt{2}}(v + H(x))$. This Higgs field is a physical scalar field which has been observed and verified.

The spinor fields are coupled to the scalar doublet field through Yukawa couplings before symmetry breaking, through terms on the form

$$g_e \left(\bar{L}_e \phi e_R + \phi^\dagger \bar{e}_R L_e \right) \quad (28)$$

which gives rise to the mass of the electron, and similar terms for all the other massive fermions (for which a right-handed chiral piece exists), see Table 1. These Yukawa terms are invariant under the local gauge symmetry groups. After symmetry breaking, when the scalar doublet field obtains a vacuum expectation value, these terms result in mass terms.

To the weak isospin group $SU(2)_L$ connect three ($= 2^2 - 1$) gauge bosons: $W_\mu^i, i = 1, 2, 3$ with the combined field $W_\mu = W_\mu^i \frac{\sigma_i}{2}$ (σ_i being the Pauli matrices). The related field strength tensor is

$$W_{\mu\nu} = \left(\partial_\nu W_\mu^i - \partial_\mu W_\nu^i + g_2 \epsilon^{ijk} W_\mu^j W_\nu^k \right) \sigma^i. \quad (29)$$

For the weak hypercharge group $U(1)_Y$ the gauge boson B_μ is the mediator. The related field strength tensor for this abelian group takes the simple form of

$$B_{\mu\nu} = \partial_\nu B_\mu - \partial_\mu B_\nu. \quad (30)$$

Thus, we have four vector gauge bosons plus the scalar Higgs boson in the electroweak sector and two gauge couplings, g_2 and g_3 , see Table 1. These four vector gauge bosons are all massless in the unbroken Standard Model Lagrangian. Experiments in the past century have, however, shown clear evidence for massive gauge vector bosons. Bosons acquire mass also in the Brout-Englert-Higgs mechanism, through the kinetic term for the scalar doublet field $D_\mu\phi^\dagger D^\mu\phi$ where the covariant derivative D_μ by local gauge symmetry contains the weak boson connection fields.

This set of vector gauge bosons are not in the physical basis. In the electroweak mixing machinery in the Glashow-Weinberg-Salam theory, two weak isospin gauge bosons combine to two massive charged W^\pm -bosons,

$$W^\pm = \frac{1}{\sqrt{2}}(W^1 \pm iW^2), \quad (31)$$

such that their interaction with the fermions arising from the kinetic term of the fermions with the connection fields entering the covariant derivative (here writing out the first generation quarks) is written as a charged current

$$\bar{u}_L\gamma^\mu W_\mu^+ d_L + \bar{d}_L\gamma^\mu W_\mu^- u_L. \quad (32)$$

and correspondingly for the lepton field and for the second and third generation fermions. The third weak boson mixes with the boson from the hypercharge group to form two neutral bosons, the Z -boson and the photon A_μ , through the planar rotation

$$\begin{pmatrix} A_\mu \\ Z_\mu \end{pmatrix} = \begin{pmatrix} \cos\theta_w & \sin\theta_w \\ -\sin\theta_w & \cos\theta_w \end{pmatrix} \begin{pmatrix} B_\mu \\ W_\mu^3 \end{pmatrix} \quad (33)$$

where the weak mixing angle θ_w is a simple relation between the two gauge couplings,

$$\sin\theta_w = \frac{g_2}{\sqrt{g_2^2 + g_3^2}} \quad (34)$$

and thus is no new parameter of the Standard Model, but simply a combination of two of the free parameters. The relation can, however, be used to replace the free parameters in favour of the weak mixing angle.

After the electroweak mixing, the Z -boson couples to the leptons and fermions through the couplings

$$\frac{e}{\sin\theta_w \cos\theta_w} (I_3^f - Q^f \sin^2\theta_w) \quad (35)$$

where I_3^f is the weak isospin charge and Q^f is the electric charge for each fermion flavour f . It is convenient to introduce a left-handed and right-handed coupling for each fermion as

$$g_L^f = I_3^f - Q^f \sin^2 \theta_w \quad \text{and} \quad g_R^f = -Q^f \sin^2 \theta_w \quad (36)$$

and further to combine these into a vector and axial-vector coupling

$$c_V^f = g_L^f + g_R^f = I_3^f - 2Q^f \sin^2 \theta_w \quad \text{and} \quad c_A^f = g_L^f - g_R^f = I_3^f. \quad (37)$$

In terms of these couplings, we can write the fermion interaction terms with the Z -boson in the Standard Model Lagrangian as

$$-i \frac{g}{2 \cos \theta_w} \bar{\psi}_f \gamma^\mu (c_V^f - c_A^f \gamma_5) \psi_f Z_\mu. \quad (38)$$

With the spontaneous symmetry breaking, the coupling of the weak bosons to the scalar doublet field reduces to

$$\underbrace{\left(\frac{1}{2}g_2v\right)^2}_{m_W^2} W_\mu^+ W^{\mu-} + \frac{1}{2} \underbrace{\left(\frac{1}{2}v\sqrt{g_2^2 + g_3^2}\right)^2}_{m_Z^2} Z_\mu Z^\mu, \quad (39)$$

acquiring masses for the vector bosons which are related, using Eq. (34), at leading order by

$$m_W = m_Z \cos \theta_w. \quad (40)$$

The quark interaction with the weak current has an additional ingredient: the quark mass eigenstates mix to form the weak eigenstates which are those describing the interaction with the weak currents. This mixing is described by the Cabibbo-Kobayashi-Maskawa (CKM) mixing matrix. The quark interaction with the charged current is modified according to

$$(u_L \quad c_L \quad t_L) \gamma^\mu \begin{pmatrix} d_L \\ s_L \\ b_L \end{pmatrix} W_\mu^+ \rightarrow (u'_L \quad c'_L \quad t'_L) \gamma^\mu V \begin{pmatrix} d'_L \\ s'_L \\ b'_L \end{pmatrix} W_\mu^+ \quad (41)$$

where on the left the quark fields are in the weak eigenstate and on the right in the mass eigenstate (primed). The mixing matrix V is a unitary matrix with entries describing the strength of the flavour changes in the charged weak interaction,

$$\begin{pmatrix} V_{ud} & V_{us} & V_{ub} \\ V_{cd} & V_{cs} & V_{cb} \\ V_{td} & V_{ts} & V_{tb} \end{pmatrix} \quad (42)$$

which is measured to be roughly the identity matrix, with some small off-diagonal entries (more significant entries in the mixing between generations 1 and 2).

Discrete symmetries and hadrons

Besides the continuous symmetries introduced so far, there are also some discrete symmetries: charge conjugation (C transformation) is the interchange of particle and corresponding anti-particle $\Psi \rightarrow \Psi^*$; parity transformation (P transformation) is the inversion of the space coordinates $\mathbf{x} \rightarrow -\mathbf{x}$; time reversal (T transformation) is the inversion of the time coordinate $t \rightarrow -t$. Combinations of these are the CP transformation and CPT transformation. The electroweak sector in the Standard Model is parity-violating, but it satisfies CP invariance. There are, however, regions in the Standard Model that indicate a slight tension with CP invariance. The combined CPT invariance is believed to hold for the Standard Model.

The particles introduced here are fundamental particles, which are pointlike objects. However, not all of these pointlike objects can be directly observed at particle detectors. Due to the scale dependence of the strong coupling constant, the light quarks are always bound into hadrons. A bound state of three quarks (three different colour charges) is a colourless baryon (a fermion) and a bound states of two quarks (of charge and anti-charge) is a colourless meson (a boson). Out of the colour sector, it is only these colourless bound states which are detectable at facilities. There is a very large plethora of bound states which are created at particle accelerators, however, only a handful are stable enough to be detected directly. The remaining fundamental particles can in theory be detected, however, among these in practice only the electron, the muon and the photon can be directly detected, which is discussed more in Section 4.

2.2 Cross sections and matrix-elements

As a quantized theory, particle collisions are described by asymptotic states, between some incoming state and some outgoing state and some transition probability between these two. The amplitude from some state $|i\rangle$ to some final state $|f\rangle$ is given by the expectation value

$$\langle f|\mathcal{T}|i\rangle = (2\pi)^4 \delta^4(P_i - P_f) \langle f|\mathcal{M}|i\rangle \quad (43)$$

where P_i denotes the total incoming four-momentum and P_f is the total outgoing four-momentum, the delta-function imposing momentum conservation. The matrix-element $\langle f|\mathcal{M}|i\rangle$ is typically abbreviated as \mathcal{M} , and is the main target for the computation of transition probabilities. The measured quantity at particle colliders for a certain process to occur is the cross section. This quantity for a $2 \rightarrow n$ process of fundamental particles (with massless final states) is given by

$$d\hat{\sigma} = \frac{1}{2s} d\Phi_n (2\pi)^4 \delta^4 \left(\sum_{i=1}^{n+2} p_i \right) |\mathcal{M}(p_i)|^2 \quad (44)$$

where s is the flux of the incoming particles. The $d\Phi_n$ factor is the differential phase space, which in the manifestly Lorentz-invariant form is given by

$$d\Phi_n = \prod_{i=1}^n \frac{d^3\mathbf{p}_i}{(2\pi)^3 2E_i}. \quad (45)$$

One is often interested in considering differential cross sections in some observable \mathcal{O} , which, by introducing the completeness relation, is generally written as

$$\frac{d\hat{\sigma}}{d\mathcal{O}} = \frac{1}{2s} d\Phi_n (2\pi)^4 \delta^4 \left(\sum_{i=1}^{n+2} p_i \right) |\mathcal{M}(p_i)|^2 \delta(\mathcal{O} - \mathcal{O}(\Phi)). \quad (46)$$

The cross section introduced is valid for partons, the fundamental particles in the Standard Model. At hadron colliders, however, the colliding objects are hadrons h . In many of the hadron collisions, only soft interactions (low energy transfer) takes place. In some collisions, however, a large momentum transfer takes place, which is called a hard scattering. The cross section for such hard scatterings can be factorized,

$$\sigma(h_1 h_2 \rightarrow n) = \sum_{a,b} \int_0^1 dx_a dx_b f_a^{h_1}(x_a, \mu_F) f_b^{h_2}(x_b, \mu_F) d\hat{\sigma}_{(ab \rightarrow n)}, \quad (47)$$

where the $f_a^{h_i}$ are parton distribution functions (PDFs), which are the longitudinally factorized probability of finding a parton a inside hadron h_i and are discussed in more detail in Subsection 2.5. The cross section $\hat{\sigma}$ is the cross section for the hard part of the interaction, sometimes also called partonic cross section, and is the main focus of most of the work in the thesis.

To compute the partonic cross section $\hat{\sigma}$ in the region where the coupling constants of the theory are small, perturbation theory can be used. Within perturbation theory, Feynman rules, as presented in Section 1, are introduced to simplify the calculation. For this machinery to be consistent, the region of small couplings is needed, as this framework builds on a perturbative expansion of the interactions, assigning diagrams with larger number of interacting points (vertices) a smaller weight, thus making the infinite perturbation series convergent. More details on the computation of the partonic cross section are discussed in Section 3.

The unit of cross section is that of $[\text{length}]^2$, in other words, the dimension of area (hence the name). Instead of the conventional SI units of m^2 , particle physics has adopted the unit of barn (b), which corresponds to $1 \text{ b} = 10^{-28} \text{ m}^2$. Typical processes at particle colliders range over a very large span of cross sections, but the widely used prefixes are those of nb (10^{-9} b), pb (10^{-12} b), and sometimes fb (10^{-15} b).

2.3 Renormalization, regularization and resonances

In this section, a very brief introduction to some of the technical aspects of quantum field theory is given, to a level which is adequate for understanding the remaining introduction and the papers.

Renormalization

Renormalization is the topic of re-defining fields, couplings and masses in quantum field theory in order to avoid divergences arising from self-interactions. In other words, it is the tool to circumvent divergences by defining physical parameters which do not coincide exactly with their counterparts predicted in the model, but rather as measured quantities. There are two main approaches in viewing renormalization. One is Wilson's approach, where degrees of freedom are integrated out, leading to the Callan-Symanzik renormalization group equations. The other approach is renormalized perturbation theory, which is the one most commonly used in automated computational tools.

The tool of Feynman diagrams in perturbation theory for computing cross sections and other quantities has a mathematical issue appearing in it: loop integrals, which when integrated over all possible momenta of the internal loop lines yield infinite quantities in the ultraviolet (UV) region (at high energies)¹. This arises already at one loop level, as we can see from the example of an electron (or any other charged particle) emitting and absorbing a virtual photon,



(48)

which in the end results in an infinite shift to the bare electron mass. The issue of divergences, however, is not an artifact of perturbation theory, but is omnipresent in quantum field theory. Loop divergences is simply the way they present themselves when perturbation theory is used for computations. As such, even when an all-order computation can be done, renormalization must take place. Loop diagrams can in addition also include infrared (IR) divergences in the regions when the loop momenta are soft. This aspect is discussed more in other parts of the thesis.

UV divergences appear at all places (when loops are involved) where perturbation theory is applied in calculations. The method of renormalization is the way of dealing with this mathematical problem by “hiding” the infinities in the parameters of the theory in a way that they depend on some unphysical scale value. The way free parameters are defined to include the infinities can, however, vary, and hence many different renormalization schemes have developed.

¹High-energy physics is equivalent to short-distance physics.

In the renormalized perturbation theory approach, one defines counterterms at each order in the expansion which cancel the divergences and are included in the perturbative calculations like the other Feynman diagrams. The unphysical scale at which the matching of the divergence cancellation occurs is the renormalization scale μ_R . The final physical result must be independent of this unphysical scale choice. This constraint leads to the renormalization group equation, which governs the scale dependence of the parameters. Following this procedure, the renormalization performed for the coupling constants $g_i, i = 1, 2, 3$ in the Standard Model lead to scale-dependent couplings, obtained by solving the renormalization group equations

$$\mu_R \frac{d}{d\mu_R} g_i(\mu_R; g_i^0) = \beta(g_i), \quad g_i(\mu_R^0, g_i^0) = g_i^0, \quad (49)$$

where $\beta(g_i)$ is a function of the coupling constant defined recursively through this renormalization group equation and hence obtained order-by-order in perturbation theory, and g_i^0 is the bare coupling. In general, the β -function can be expanded in the coupling as

$$\beta(g_i) = g_i \sum_{i=0} b_i \left(\frac{g_i}{4\pi} \right)^{2i+2}. \quad (50)$$

The initial condition is a definition of the renormalized coupling at some scale μ_R^0 . It is straightforward to solve this equation for a β -function of the form $\beta(g_i) = Ag_i^3, A > 0$, which is the case for the electroweak coupling constant, resulting in

$$g_i(\mu_R, g_i^0) = \frac{g_i^0}{1 - Ag_i^0 \log \left(\frac{\mu_R}{\mu_R^0} \right)}, \quad (51)$$

resulting in a coupling which increases with increasing energy. If the β -function instead is negative on the form $\beta(g_i) = -Ag_i^3$, the resulting running of the coupling

$$g_i(\mu_R, g_i^0) = \frac{g_i^0}{1 + Ag_i^0 \log \left(\frac{\mu_R}{\mu_R^0} \right)} \quad (52)$$

decreases with increasing energy. This is a feature for any unitary gauge group $SU(n)$ with $n > 2$, so also for the strong coupling constant. This is the reason for the asymptotic freedom of quarks, and indirectly of the confinement of quarks in bound states of hadrons. The scale at which perturbation theory breaks down because of the strong running coupling is the Λ_{QCD} scale, with a rough value of ~ 1 GeV.

By an expansion in the small g_i^0 limit, we find that the expansion contains terms of the form

$$g_i(\mu_R, g_i^0) \sim (g_i^0)^{k+1} \left(A \log \left(\frac{\mu_R}{\mu_R^0} \right) \right)^k. \quad (53)$$

Thus, given a small coupling constant at the renormalization scale μ_R , the perturbative series for the running coupling may be invalidated if the typical momentum μ_R^0 of the system obeys $\frac{\mu_R}{\mu_R^0} \ll 1$ or $\frac{\mu_R}{\mu_R^0} \gg 1$. Thus, in order for the perturbative expansion in the coupling constants to be well-defined and converge, it is of importance to pick the renormalization scale μ_R at a value of typical order of the hard scattering scale. For this reason, often a dynamical scale is chosen, which evaluates the couplings on an event-by-event basis.

The couplings are often expressed in terms of $\alpha_i = \frac{g_i^2}{4\pi}$, in which case the β -function is obtained by the simple variable change $\beta(\alpha_i) = \frac{g_i}{2\pi} \beta(g_i)$ and similarly the running of the couplings is expressed as $\alpha_i(\mu_R)$ instead. This convention is convenient when the matrix-element is squared to give the contribution to the cross section.

Resonances

The lifetime τ of a particle is characterized by its inverse decay width $\tau \sim 1/\Gamma$. The decay width is the transition probability for a $1 \rightarrow n$ decay, corresponding to a cross section for a $2 \rightarrow n$ process. If a particle is stable, then the decay width $\rightarrow 0$, while an unstable particle has a finite decay width and is then called a resonance. In other words, an unstable particle is one which does not appear as an asymptotic state of the incoming or outgoing state in a process but appears in an intermediate state of the interaction.

To understand resonances more, we investigate the physical propagator of a scalar particle with mass m_0 . For this, we define the one-particle-irreducible (1PI) graphs which is the sum of all possible all-order corrections to an external leg, that is, the diagrams which keep together no matter which internal line is cut. Then, the physical propagator can be written as a sum of any number of insertions of these 1PI contributions,

$$\text{wavy line with black blob} = \text{wavy line with gray blob} + \text{wavy line with two gray blobs} + \text{wavy line with three gray blobs} + \dots$$

with the 1PI correction denoted by gray blobs and denoted by $-i\Sigma(s)$, dependent on the invariant mass s of the propagator. This sum is a geometric series, which can be computed directly as

$$\frac{1}{s - m_0^2} \sum_{n=1}^{\infty} \left(-i\Sigma(s) \frac{i}{s - m_0^2} \right)^n = \frac{1}{s - m_0^2 + \Sigma(s)}. \quad (54)$$

If the propagator can decay into particles (conserving energy and momentum), then it

contributes² to the total cross section as

$$\sigma \sim \frac{1}{(s - m^2)^2 + m^2\Gamma^2}, \quad (55)$$

which is the (relativistic) Breit-Wigner shape of a resonance. From here we see that the width Γ also controls the width of the Gaussian distribution for resonances, hence the name. In the limit $\Gamma/m \rightarrow 0$, which is called the narrow-width approximation (NWA), this Gaussian distribution tends towards

$$\frac{1}{(s - m^2)^2 + m^2\Gamma^2} \rightarrow \frac{\pi}{m\Gamma} \delta(s - m^2) \quad (56)$$

which sets the momentum of the resonance to be on-shell in the final phase-space integral. This often leads to large simplifications in the calculations dealing with resonant particles. The error of this approximation at the total cross section level is $\sim \Gamma/m$, however, for differential observables this is less obviously evaluated. The difference from the narrow-width treatment and the full treatment is often called off-shell effects.

Regularization

To handle the arising divergences in loop diagrams, both in the UV and IR regions, and to correctly follow through the cancellation, a proper bookkeeping, regularization, of the divergent terms must be done. The most commonly used regularization is dimensional regularization³, in which the dimension of the loop integrals is taken to be $d = 4 - \epsilon$ allowing ϵ to be an infinitesimal regulator of the UV divergences, or similarly $d = 4 + \epsilon$ for IR divergences.

As an example for this, we consider the mass correction to the electron by computing the 1PI corrections at one-loop in $d = 4 - \epsilon$ dimensions. The mass shift is given by the shift in the propagator denominator on the form of Eq. (54), which ultimately results in computing the one-loop correction to the self-energy in Eq. (48). The loop integral is evaluated using master integral formulas and dimensional regularization to

$$\delta m \sim \Sigma_{\text{one-loop}}^{\text{electron}} \sim \Gamma(2 - d/2) \int_0^1 dx \frac{(4 - 2x - \epsilon(1 - x))}{((1 - x)^2 m^2 + x\mu^2)^{2-d/2}} \quad (57)$$

with a final result

$$\sim \frac{2}{\epsilon} - \gamma_E + \log 4\pi \quad (58)$$

²Owing to the cutting rules which allow to relate loop amplitudes to open diagrams by cutting the propagator lines.

³Other regularization schemes are mass regularization, in which the massless gluon or photon are given a small mass which regulates the divergence; or applying momentum-cutoffs which are less favored because they break gauge invariance.

where γ_E is the Euler-Mascheroni constant⁴. In the minimal subtraction scheme (MS), the expansion of a loop diagram is in terms of the ϵ regulator only, which in this one-loop case is precisely Eq. (58). One can also include the constants which always accompany this regulator by the redefinition

$$\frac{2}{\epsilon} \rightarrow \left(\frac{2}{\epsilon} - \gamma_E + \log 4\pi \right), \quad (59)$$

in the modified minimal subtraction scheme ($\overline{\text{MS}}$), making the cancellation of infinities simpler to handle. Although the final result is not dependent on which scheme is used, one must be careful to define it for cross-validations and consistent computations.

2.4 Parameters of the Standard Model

Without considering right-handed neutrinos, there are 18 free parameters in the Standard Model, which are summarized in Table 3.

Table 3: The natural way of presenting the 18 free parameters of the Standard Model. Red marks the electroweak parameters (discussed in the text).

Charged lepton masses	m_e, m_μ, m_τ
Quark masses	$m_u, m_d, m_s, m_c, m_b, m_t$
CKM mixing angles	$\theta_{12}, \theta_{13}, \theta_{23}$
CKM CP violating phase	δ_{CKM}
$SU(3)_C$ gauge coupling	g_1
$SU(2)_L$ gauge coupling	g_2
$U(1)_Y$ gauge coupling	g_3
Higgs mass	m_H
Vacuum expectation value	v

In the colour gauge sector of the Standard Model there is firstly the strong gauge coupling g_1 , which by convention is often expressed as $\alpha_s = \frac{g_1^2}{4\pi}$. Secondly, there are the four angles (three mixing angles and one CP violating phase) appearing in the CKM matrix in the quark mixing sector describing flavour-changing currents. These play a crucial role in new physics searches as they probe the CP violating parts of the Standard Model.

⁴The approximate value for this constant is $\gamma_E \approx 0.5772$.

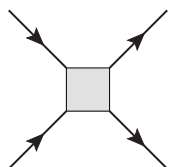
The lepton and quark masses appear as simple (fermion) mass terms after the symmetry breaking of the Yukawa couplings. In the symmetry breaking, the Higgs boson acquires a mass, which is another parameter of the theory, expressed in terms of the coupling μ in the Higgs sector Lagrangian.

We now turn to the red terms in Table 3. These three parameters constitute the **electroweak sector**. All the other parameters are most often used without much modification. However, the electroweak sector is a very precise area in the Standard Model, and hence there have developed alternative ways of expressing these parameters, which better suit the available measurements.

One of these alternative parameters is the weak mixing angle θ_w of the gauge boson fields of the $U(1)_Y$ and the $SU(2)_L$ groups, see Eq. (33). Secondly, in the physical fields of the gauge bosons, the photon field A_μ interacts with the charged quarks and fermions. The coupling with the charged fermions is by convention picked to be the elementary charge e , which is expressed in terms of the underlying gauge couplings as

$$e = \frac{g_2 g_3}{\sqrt{g_2^2 + g_3^2}} \quad (60)$$

and often $\alpha = \frac{e^2}{4\pi}$ is used instead. Another well-measured observable in particle physics is the four-fermion coupling constant, the Fermi constant G_μ appearing in the effective four-point interaction of fermions in the vertex



The diagram shows a central square vertex with four external lines. Two lines enter from the left and two exit to the right, all with arrows pointing away from the vertex. The vertex is shaded gray.

$$\sim -\frac{G_\mu}{\sqrt{2}} (\bar{\psi}(x)\gamma_\mu\psi(x)) (\bar{\psi}(x)\gamma^\mu\psi(x)), \quad (61)$$

originally introduced to explain the β -decay in which the proton, neutron, electron and electron neutrino are the four interacting fermions. As such, the Fermi constant is very well measured through the measurement of the muon lifetime, and hence is often picked as the input parameter in the electroweak sector. These precision parameters relate, at leading order, to the natural parameters of the Standard Model as

$$\cos \theta_w = \frac{m_W}{m_Z}, \quad G_\mu = \sqrt{2} \frac{g_3^2}{8m_W^2}. \quad (62)$$

Combining the relations, we can express the relation between the Fermi constant and the electroweak coupling as

$$\alpha = G_\mu \frac{\sqrt{2}m_W^2}{\pi} \left(1 - \frac{m_W^2}{m_Z^2} \right). \quad (63)$$

The set of electroweak parameters $\{m_W, m_Z, \alpha, G_\mu\}$ can always be reduced to a set of three independent ones. Thus, if this set is chosen consistently, the final result remains gauge invariant. Three main input schemes are defined,

$\alpha(0)$ scheme	$\{\alpha(0), m_W, m_Z\}$
$\alpha(m_Z)$ scheme	$\{\alpha(m_Z), m_W, m_Z\}$
G_μ scheme	$\{G_\mu, m_W, m_Z\}$

where the essential difference between the three schemes is which of the α or G_μ are chosen as input, and/or at which renormalization point α is defined. The values of the electroweak coupling constant α in the $\alpha(0)$ scheme is the fine-structure constant $\alpha(0) \approx 1/137$; in the $\alpha(m_Z^2)$ scheme, the value is (taking the running of the coupling into account to the Z -boson pole mass) $\alpha(m_Z^2) \approx 1/129$; finally in the G_μ scheme, the resulting coupling is $\alpha_{G_\mu} \approx 1/132$ [3]. The relative sizes range from 2.3% to 5.8%. Thus, considering only the input value choice for the coupling results in quite significant differences. The optimal choice for the input scheme is process-specific and care must be taken to not introduce large logarithms when treating a hard scattering at a much larger scale than the coupling is defined. It is important to choose one of the input scheme for the electroweak coupling α for each gauge-invariant part of the computation, otherwise inconsistent results can be obtained. When considering external photons, the choice of the $\alpha(0)$ scheme must be made, however, this introduces dependence on the non-perturbative quark masses in the coupling. One approach is to combine the input schemes in a non-gauge-violating way [4].

A commonly used quantity for the precision relation between the parameters is the ρ -parameter [5], which is defined as

$$\rho = \frac{m_W^2}{m_Z^2 \cos^2 \theta_w}. \quad (64)$$

At tree level, this parameter is simply $\rho = 1$ (as can be easily seen from the relation in Eq. (62)). Including higher order electroweak corrections to the parameters, the ρ -parameter is shifted by

$$\rho = \frac{1}{1 - \Delta\rho} \quad (65)$$

with the corrections embedded in $\Delta\rho$ and computed perturbatively. We can explore the role of the ρ -parameter in the input schemes by relating (at next-to-leading order) the three input schemes for the electroweak coupling

$$\begin{aligned} \alpha(m_Z^2) &= \alpha(0) + \alpha(m_Z^2)\Delta\alpha(m_Z^2), \\ \alpha_{G_\mu} &= \alpha(0) + \alpha(0)\Delta r, \end{aligned} \quad (66)$$

where $\Delta\alpha(m_Z^2)$ is the relative shift due to the running of the coupling from the limit $Q^2 = 0$ to the electroweak scale, including the light fermions, and Δr is the electroweak correction to the vector boson mass correlation. The one-loop correction $\Delta\rho$ contains the dependence on the top quark mass m_t . These corrections are related by

$$\Delta r = \Delta\alpha(m_Z^2) - \Delta\rho \frac{\cos^2 \theta_w}{\sin^2 \theta_w} + \text{small finite part}, \quad (67)$$

which makes the two corrections essentially the same regarding the running corrections $\Delta\alpha(m_Z^2)$. What differs is that the weak couplings obtain a correction via the weak mixing angle $\sin^2 \theta_w \rightarrow \sin^2 \theta_w + \Delta\rho \cos^2 \theta_w$ for every weak $SU(2)_L$ vertex. Putting all this together into the physically relevant weak coupling $\alpha_{G_\mu} / \sin^2 \theta_w$, one obtains that upon applying both of the corrections to the $\sin^2 \theta_w$ and to the α , the $\Delta\rho$ correction drops out, leaving only the $\Delta\alpha(m_Z^2)$ correction

$$\begin{aligned} \frac{\alpha_{G_\mu}}{\sin^2 \theta_w} &\rightarrow \frac{\alpha_{G_\mu}}{(\sin^2 \theta_w + \Delta\rho \cos^2 \theta_w) \left(1 - \Delta\alpha(m_Z^2) - \Delta\rho \frac{\cos^2 \theta_w}{\sin^2 \theta_w}\right)} \\ &\rightarrow \frac{\alpha_{G_\mu}}{\sin^2 \theta_w (1 - \Delta\alpha(m_Z^2))} \end{aligned} \quad (68)$$

where the second line holds up to next-to-leading order.

Currently, theory predicts the ρ -parameter at four-loop level. The main uncertainty entering the theoretical calculations is in the renormalization scale. The customary approach is to pick the $\mu_R = m_t$ and by applying the usual 7- or 9-point variation assess the scale dependence. However, both of these are chosen arbitrarily and thus introduces a strong renormalization scale and scheme dependence in the evaluation of both the ρ -parameter and its errors [6].

An alternative way of treating the weak mixing angle is through the effective leptonic coupling [7]. In this approach, one absorbs the electroweak radiative corrections into a flavour-dependent factor κ_f which alters the weak mixing angle into an effective one by

$$\sin^2 \theta_{\text{eff}}^f = \kappa_f \sin^2 \theta_w \quad (69)$$

and has been measured by experiments (CMS [8], ATLAS [9]). When using the effective weak mixing angle as independent input parameter, extra care must be taken to recover gauge cancellation, as choosing all of the weak boson masses and the weak mixing angle as independent causes inconsistent results.

When intermediate unstable particles enter the calculation, methods have to be applied in order not to violate the gauge symmetry. One such approach is the complex mass scheme [10], which assigns an imaginary part to the mass of the unstable particle

$$\mu^2 = m^2 - i\Gamma m \quad (70)$$

with the decay width Γ and physical mass m . This choice is done such that the propagator denominator is changed to

$$p^2 - m^2 \rightarrow p^2 - m^2 + i\Gamma m$$

which indeed recovers the finite-width resonance structure for the heavy particles. As a consequence, derived parameters, such as α or the Fermi constant G_μ obtain non-vanishing complex phases. If the coupling α obtains a complex phase, the IR cancellation is intricate, as the location of the poles in the complex plane makes the cancellation not exact. One way of remedying this is to render α real. This can be done in several ways, for example by assigning its real value $\alpha \rightarrow \text{Re}[\alpha]$ or by using an absolute value $\alpha \rightarrow |\alpha|$. An alternative approach is to use the relation between the four electroweak parameters in Eq. (70) to assign all complex phases of the electroweak parameters in a complex-valued Fermi constant $G_\mu \rightarrow G_\mu e^{i\theta}$ with θ being the phase resulting from the complex masses of the W - and Z -bosons. This scheme is the complex- G_μ scheme (\overline{G}_μ), which is equivalent to the G_μ scheme in the input parameters, but the input value of G_μ is used for the magnitude only, while the phase is determined by the widths of the unstable particles.

At very high energy collisions, the masses of the light leptons and quarks are negligible. In automated calculations, a model with massless leptons and n_q massless quarks is adopted. The role of the b -quark, however, is intricate, as it is the only quark with a mass $\Lambda_{\text{QCD}} < m_b \ll \{m_Z, m_W\}$. If the b quark is considered massive and is not included in the PDF evolution, we speak of a 4 flavour-scheme ($n_q = 4$), and if also the b -quark is set massless below the scale m_b , we have a 5-flavour scheme ($n_q = 5$). In b -quark productions, large logarithms appear as $\log \frac{s}{m_b^2} \sim 1$, and hence need careful resummation. Defining the b -quark as massless, this problem is alleviated, moving the problem of resummation of the b -quark into the PDF evolution.

2.5 Soft emissions, parton evolution and infrared safety

Measuring and detecting particles with very low energy or two particles produced collinear to each other, is physically not possible. This is also reminiscent in the theoretical description of emissions. To see this precisely, we examine a final state quark splitting $q \rightarrow qg$, treating all particles massless,

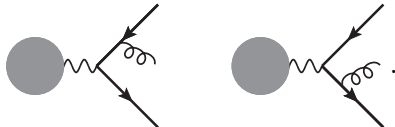


Soft and collinear divergences (which are IR divergences) arise for the internal quark propagator

$$\frac{1}{(k+k')^2} = \frac{1}{2E_1 E_2 (1 - \cos \theta)} \quad (71)$$

as $E_{1,2} \rightarrow 0$ (soft divergence) and $\cos \theta \rightarrow 1$ (collinear divergence) respectively, where θ is the angle between the two emerging quark and gluon and $E_{1,2}$ is the energy of the two outgoing particles. If one instead treats the quark propagator as massive, the extra $-m^2$ in the denominator of the propagator regulates the collinear divergence, leaving only a soft divergence.

To see how such a soft emission affects the cross section, we consider the emission of a soft gluon with energy E from a quark-anti-quark pair, that is connected to some generic process, denoted with a blob,



Considering the emission from both of the fermion legs, in the soft/collinear limit, this part of the total cross section factorizes as

$$\sigma \sim |\mathcal{M}|_{qqg}^2 d\Phi_3 \rightarrow 2C_F \frac{\alpha_s}{\pi} \frac{dE}{E} \frac{d\theta}{\theta} \frac{d\phi}{2\pi} |\mathcal{M}|_{qq}^2 d\Phi_2 \quad (72)$$

where the $d\Phi_{2,3}$ are the 2 and 3-particle phase spaces respectively (with and without the emitted gluon) and C_F is the group theoretical constant introduced in Eq. (22). The soft and collinear divergences appear as double logarithmic divergences after integration in phase space. According to a theorem by Kinoshita, Lee and Nauenberg (KLN theorem) [11, 12], these soft and collinear divergences in the final state emissions cancel the divergences appearing in the virtual contributions (to be discussed later in Subsection 3.4) when all contributions are included order-by-order. The cancellation between the real and virtual contributions is only guaranteed for infrared-safe observables. By infrared safety, one means an observable which is not dependent on the physics which occurs at short distances. At the level of diagrams, an observable \mathcal{O} is said to be infrared safe if the splitting of a particle with momentum \mathbf{p}_i to two particles $\mathbf{p}_i = \mathbf{p}_i^1 + \mathbf{p}_i^2$ does not alter the value of the observable,

$$\mathcal{O}(\mathbf{p}_1, \dots, \mathbf{p}_i^1, \mathbf{p}_i^2, \dots, \mathbf{p}_n) = \mathcal{O}(\mathbf{p}_1, \dots, \mathbf{p}_i, \dots, \mathbf{p}_n) \quad (73)$$

for when at least one of $\mathbf{p}_i^{1,2}$ is soft or if they are collinear to each other.

Infrared safety is an important property for observables when comparing experiments to theory, and especially, fixed-order predictions (discussed more in Section 3). Infrared safety implies that whatever is measured at the detectors can be directly translated to the high-energy (short distance) physics. Examples of infrared safe observables are inclusive cross sections or event shape observables such as thrust⁵. A way of testing infrared safety in

⁵Thrust is defined as $T = \max_{\mathbf{v}} \frac{\sum_i |\mathbf{p}_i \cdot \mathbf{v}|}{\sum_i |\mathbf{p}_i|}$ with the sum over all outgoing particles and \mathbf{v} is picked to define the largest possible T . It is a measure of how pointlike or spherical an event shape is.

numerical calculations of distributions is by examining whether phase-space points which are divergent but their sum is finite always are placed in the same bins in histograms. If this is not the case, it is clear that some bins diverge as the number of phase-space point increases without any IR cancellation occurring bin-by-bin. If an observable is not infrared-safe, it may still be computed, but must be computed within the factorization approach (Eq. (47).), including correctly the parton evolution and PDFs.

As already introduced, the PDFs are probability functions for extracting a parton within a composite particle with certain kinematic properties. Specifically, the probability of a parton a interacting inside proton p with longitudinal momentum fraction in the interval $[x, x + dx]$ having transverse momentum less than Q is given by $f_a^p(x, Q)dx$. The scale dependence on Q encodes that the probability distribution is dependent on the length scale at which we probe the proton. This dependence is mild, and obtains non-zero contributions from higher-order corrections. The longitudinal momentum fraction x is given by $x = \frac{Q^2}{2P \cdot q}$, with P being the incoming hadron momentum, and q the transfer momentum. The PDFs are measured quantities, however, are not measured at each energy scale, but are instead evolved from a measured scale Q_0^2 to the required scale needed for the computation of the hadronic cross section. The evolution of PDFs (the variation with the energy scale Q) can, on the other hand, be computed within perturbation theory. Including only the QCD splittings, this evolution is given by the Dokshitzer-Gribov-Lipatov-Altarelli-Parisi (DGLAP) equations [13–15] at first order in the strong coupling by

$$\frac{df_i(x, \mu_F^2)}{d \log \mu_F^2} = \frac{\alpha_s}{\pi} \sum_j P_{ij}(z) \otimes f_j(x, \mu_F^2) \quad (74)$$

where the sum over j is over all partons inside the proton, and $P_{ij}(z)$ define the splitting functions $i \rightarrow j$, including all colour and kinematic factors of the splitting, with longitudinal momentum fraction z . The usual definition for the convolution of functions is used,

$$(f \otimes g)(x) = \int_0^1 dy dz \delta(x - yz) f(y) g(z). \quad (75)$$

The factorization scale μ_F is introduced instead of the energy scale Q . This scale separates the PDF scale from the hard scattering scale and is another (besides the renormalization scale μ_R) a freely chosen parameter which often is picked as $\mu_F = \mu_R$.

PDFs satisfy momentum sum rules, which incorporate that summing the momenta of all parton species must yield the full momentum of the composite particle,

$$\sum_i \int dx f_i(x, Q) x = 1, \quad (76)$$

and various valence quark content sum rules, which for the proton (with a uud valence quark content) are

$$\int dx(f_u(x) - f_{\bar{u}}(x)) = 2, \quad \int dx(f_d(x) - f_{\bar{d}}(x)) = 1. \quad (77)$$

Based on such relations, and on measurements of quark PDFs in the proton, a rough 50% of parton content is found missing, which is subscribed as the gluon contribution in the proton. Although this gluon content is dependent on both the scale Q and the fraction x , gluon-induced processes are highly dominating at LHC. When electroweak corrections are considered, also the photon content in the proton must be included, which in general is a small contribution, but it may open up new partonic channels which result in sizeable electroweak corrections.

Finally, a direct computation for the factorization at work is presented. Consider an incoming quark which enters the hard scattering (with cross section σ_0). This process at order α_s has a real-emission contributions (emitting a soft or collinear gluon) and a virtual contribution,

When performing the calculations for these two contributions, one finds the cross sections are separately

$$\hat{\sigma}_R = \sigma_0(zp) \frac{\alpha_s C_F}{\pi} \frac{dz}{1-z} \frac{dk_T^2}{k_T^2}, \quad (78)$$

$$\hat{\sigma}_V = -\sigma_0(p) \frac{\alpha_s C_F}{\pi} \frac{dz}{1-z} \frac{dk_T^2}{k_T^2}, \quad (79)$$

where p is the momentum of the quark, and zp is the momentum fraction carried by the quark after the splitting, and k_T is the transverse momentum of the quark after splitting. The total cross section is the sum of the two contributions,

$$\hat{\sigma} = \frac{C_F \alpha_s}{\pi} \int dz \frac{dk_T^2}{k_T^2} \frac{1}{1-z} (\sigma_0(zp) - \sigma_0(p)) \quad (80)$$

from which it becomes clear that for the $z \rightarrow 1$ limit, the soft parts of the real and virtual corrections cancel, while the collinear divergence in $k_T^2 \rightarrow 0$ remains. The remedy is to include the low-energy, non-perturbative region for $k_T < \mu_F$ in the PDFs, introducing a low-energy cut-off in the integral,

$$\sigma = \frac{C_F \alpha_s}{\pi} \sum_i \int_{\mu_F^2}^{Q^2} dx dz \frac{dk_T^2}{k_T^2} \frac{1}{1-z} (\sigma_0(zxp) - \sigma_0(xp)) f_i(x, \mu_F^2) \quad (81)$$

which indeed removes the collinear divergence. Note that now the incoming quark carries the fraction x of the incoming proton momentum p . Physically, we have removed our lack of knowledge on the non-perturbative physics below the cut-off μ_F to be included in the PDFs which are fitted to data.

2.6 The colour expansion in the large- N_C limit

As already introduced, the strong interaction sector of the Standard Model is described by the $SU(3)_C$ gauge group. This gauge group involves heavy computations due to the rich group structure. Hence, when a large number of strongly interacting particles is included in a process, the computation becomes significantly slower due to the colour gauge group handling alone. In paper III, we suggest an improvement to this calculation of the colour gauge group by using the large- N_C limit in the colour expansion of matrix-elements. Here, some introduction is given to these concepts as well as some complementary information to paper III.

The large- N_C expansion

Although there is clear evidence for three colour charges ($N_C = 3$) in the Standard Model, it turns out that treating the number of colours as infinite, $N_C \rightarrow \infty$, leads to simplifications in the calculations and reliable results. To see whether this limit can recover the features of QCD, the β -function (at one-loop) of QCD is examined,

$$\beta(\alpha_s) = b_0 \frac{\alpha_s^2}{4\pi}, \quad b_0 = -\frac{11}{3}N_C + \frac{2}{3}N_F < 0, \quad (82)$$

with N_F active flavours. This leads to the first-order solution of the strong coupling,

$$\alpha_s(Q) = \frac{\alpha_s(\mu^2)}{1 - b_0 \frac{\alpha_s(\mu^2)}{4\pi} \log \frac{Q^2}{\mu^2}}. \quad (83)$$

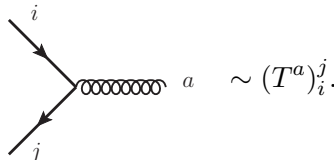
Keeping a fixed value for $\frac{g_1}{\sqrt{N_C}}$ (recall $g_1 = \sqrt{4\pi\alpha_s}$) while taking the $N_C \rightarrow \infty$ limit (meaning that the gauge coupling $g_1 \rightarrow 0$), recovers the same asymptotic behaviour for the strong interaction.

Next, we investigate how this limit simplifies computations. The $SU(N_C)$ gauge group has the representation

$$\mathbf{N}_C \otimes \overline{\mathbf{N}}_C = (\mathbf{N}_C^2 - \mathbf{1}) \oplus \mathbf{1}. \quad (84)$$

The gauge bosons, in the adjoint representation $(\mathbf{N}_C^2 - \mathbf{1})$ carry a colour index denoted by $a = 1, 2, \dots, N_C^2 - 1$ (which are the 8 physical gluons already introduced). The quarks,

transforming under the fundamental representation, carry an index $i = 1, 2, \dots, N_C$ and the anti-quarks carry an index $j = 1, 2, \dots, N_C$ (no distinction is made between the notation for the quark and anti-quark index). With this notation, the fundamental generators $(T^a)_i^j$ carry one adjoint index, one fundamental index and one anti-fundamental index, corresponding to the colour factor of the particle indices in a quark-gluon vertex,

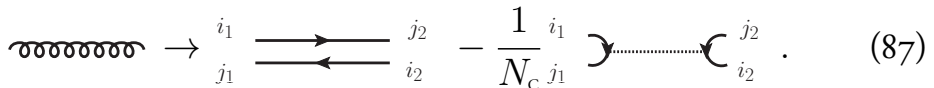


$$\begin{array}{c} i \\ \swarrow \\ \text{---} \\ \searrow \\ j \end{array} \text{---} a \sim (T^a)_i^j. \quad (85)$$

In the colour-flow representation, the gluon field can be viewed as a two-index field rather than one with an adjoint index. This means that the gluon propagator, proportional to δ_b^a in the adjoint representation, becomes

$$\delta_{j_2}^{i_1} \delta_{j_1}^{i_2} - \frac{1}{N_C} \delta_{j_1}^{i_1} \delta_{j_2}^{i_2}. \quad (86)$$

This decomposition introduces new Feynman rules for the gluon propagator, in the so-called the double-line notation,



$$\text{---} \rightarrow \begin{array}{c} i_1 \\ \text{---} \\ j_1 \end{array} \begin{array}{c} \text{---} \\ \text{---} \\ j_2 \\ i_2 \end{array} - \frac{1}{N_C} \begin{array}{c} i_1 \\ \text{---} \\ j_1 \end{array} \begin{array}{c} \text{---} \\ \text{---} \\ i_2 \\ j_2 \end{array}. \quad (87)$$

This identity is called the Fierz identity and is a decomposition of the $SU(N_C)$ boson into a $U(N_C)$ boson and a (subtracted) $U(1)$ part. This implies that the gluon field with an adjoint index is now written in terms of a field with two fundamental indices

$$G_\mu^a \rightarrow G_{\mu,i}^j = G_\mu^a (T^a)_i^j, \quad (88)$$

with the traceless constraint of $G_{\mu,i}^i = 0$. Using the basis for the Gell-Mann matrices this field can be written explicitly as

$$\begin{pmatrix} G_\mu^3 + \frac{1}{\sqrt{3}} G_\mu^8 & G_\mu^1 - i G_\mu^2 & G_\mu^4 - i G_\mu^5 \\ G_\mu^1 + i G_\mu^2 & -G_\mu^3 + \frac{1}{\sqrt{3}} G_\mu^8 & G_\mu^6 - i G_\mu^7 \\ G_\mu^4 + i G_\mu^5 & G_\mu^6 + i G_\mu^7 & -\frac{2}{\sqrt{3}} G_\mu^8 \end{pmatrix}. \quad (89)$$

The $U(1)$ gauge boson, however, does not couple to the $SU(N_C)$ part of the bosons, as these constitute an orthogonal decomposition of the gluon representation. As such, in all-gluon amplitudes, only the $U(N_C)$ contributions need to be considered, while if fermions are present, then both of the contributions of the gluon must be considered. The $U(1)$ part is accompanied with a factor of $\frac{1}{N_C}$, meaning that in the large- N_C limit these vertices are suppressed.

The colour expansion

The matrix-element of a generic process can be colour decomposed, meaning that the colour factors are stripped off the diagrams. The square of the matrix-element then is the interference of two such decompositions, schematically of the form

$$|\mathcal{M}|^2 = g_1^x \sum_{\sigma_k, \sigma_l} C(\sigma_k, \sigma_l) \mathcal{A}(\sigma_k, p_i, \lambda_i) \mathcal{A}^*(\sigma_l, p_i, \lambda_i) \quad (90)$$

where the $C(\sigma_k, \sigma_l)$ matrix is called the colour matrix and contains the colour factors for the colour expansion. The momenta of the external particles are p_i and their helicities are λ_i . The rows and columns of the colour matrix are labeled with σ_k, σ_l , which are some permutations of the QCD particles in the process. The order of the strong coupling g_1^x depends on the type of particles included in the amplitude. The \mathcal{A} are the gauge-invariant dual amplitudes, or colour-ordered amplitudes. These objects are dependent solely on the kinematics and helicity (and the permutation of the particles). The exact content of the colour matrix depends on the type of process and the representation chosen. A summation over the colour indices is always understood at the level of the squared matrix-element.

To be specific, an all-gluon matrix-element with n external gluons, is decomposed as

$$\mathcal{M} = g_1^{n-2} \sum_{\sigma \in S_{n-1}} \text{Tr}[T^{a_{\sigma(1)}} \dots T^{a_{\sigma(n-1)}} T^{a_n}] \mathcal{A}(\sigma(1), \dots, \sigma(n-1), n) \quad (91)$$

where S_{n-1} is the permutation group of $n-1$ elements. The $(n-1)!$ dual amplitudes are not all independent, but are related by

$$\begin{aligned} \mathcal{A}(1, 2, \dots, n-1, n) &= \mathcal{A}(n, 1, 2, \dots, n-1), \\ \mathcal{A}(1, 2, \dots, n-1, n) &= (-1)^n \mathcal{A}(n, n-1, \dots, 2, 1), \\ \mathcal{A}(1, 2, 3, \dots, n) &+ \mathcal{A}(2, 1, 3, \dots, n) + \mathcal{A}(2, 3, 1, \dots, n) \\ &+ \dots + \mathcal{A}(2, 3, \dots, 1, n-1, n) + \mathcal{A}(2, 3, \dots, 1, n) = 0, \end{aligned} \quad (92)$$

which describe invariance under cyclic permutation, the reflection property, and the dual Ward identity relation (the insertion of a gluon index in all possible positions sums to zero).

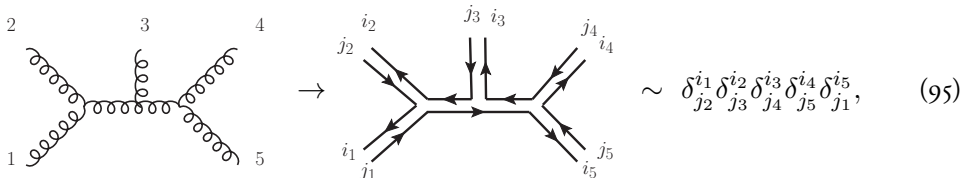
In the colour-flow representation of an n -gluon process, the same set of dual amplitudes is used, but the colour factors are simpler. The all-gluon amplitude in this basis is written as

$$\mathcal{M} = g_1^{n-2} \sum_{\sigma \in S_{n-1}} \delta_{j_{\sigma(1)}}^{i_n} \delta_{j_{\sigma(2)}}^{i_{\sigma(1)}} \dots \delta_{j_n}^{i_{\sigma(n-1)}} \mathcal{A}(\sigma(1), \dots, \sigma(n-1), n). \quad (93)$$

In this basis, the elements in the colour matrix are products of Kronecker deltas, which are computed to monomials in N_C with the basic index contraction

$$\delta_{j_2}^{i_1} (\delta_{j_2}^{i_1})^\dagger = \delta_{j_2}^{i_1} (\delta_{i_1}^{j_2}) = \delta_{i_1}^{j_2} = N_C. \quad (94)$$

In other words, the colour-flow representation utilizes the decomposition of the adjoint index according to the double-line notation to a fundamental and anti-fundamental index as in Eq. (87). In this notation, the colour factors of the Feynman diagrams in this basis are intuitively read off from the diagram,



and the case with quark lines are similarly constructed (but each quark line carrying one colour index only).

The set of relations in Eq. (92) can be used to eliminate redundant dual amplitudes. It has been shown [16] that the number of independent dual amplitudes for all-gluon processes is $(n-2)!$. Using this minimal set of dual amplitudes, one can decompose the matrix-element in the adjoint representation

$$\mathcal{M} = g_1^{n-2} \sum_{\sigma \in S_{n-2}} (F^{a_{\sigma(2)}} \dots F^{a_{\sigma(n-1)}})_{a_n}^{a_1} \mathcal{A}(1, \sigma(2), \dots, \sigma(n-1), n). \quad (96)$$

When squaring this matrix-element, the colour factors contract to combine into the colour-matrix

$$C(\sigma_k, \sigma_l) = \text{Tr}[F^{a_{\sigma_k(2)}} \dots F^{a_{\sigma_k(n-1)}} F^{b_{\sigma_l(2)}} \dots F^{b_{\sigma_l(n-1)}}] \quad (97)$$

with the adjoint matrices $(F^a)_c^b = -if^{abc}$.

The colour matrix-elements are polynomials (in the adjoint and fundamental representations) and monomials (in the colour-flow representation) in N_C . As such, the entries are of the form

$$N_C^x + aN_C^{x-1} + bN_C^{x-2} + \mathcal{O}(N_C^{x-3}), \quad (98)$$

where the first non-vanishing term is called leading-colour (LC), the next term is next-to-leading colour (NLC), and so on. For amplitudes with no or distinct-flavoured quark lines, this colour expansion is actually in terms of $\left(\frac{1}{N_C}\right)^2$, yielding an error of $\left(\frac{1}{N_C}\right)^4 \approx 1\%$ at a NLC truncation.

The computationally costly part of the calculation for large number of strongly interacting particles is the large number of colour-ordered amplitudes that need to be evaluated in the sum over the permutations of the particles. The LC terms in the colour matrix are those with a squared dual amplitude ($\sigma_k = \sigma_l$). Hence, in theory, all dual amplitudes must still be computed, even with a sparse colour matrix. In practice, one can utilize the symmetry of final state particles, which is suggested in paper III. This allows to not

Table 4: For the colour matrix in the fundamental representation, the number of non-zero elements in one row (middle column) and total number of rows (middle column parenthesis) and number of dual amplitudes (right column) that need to be computed when a NLC truncation and final state symmetry is utilized for all-gluon processes with n gluons.

all-gluon		
n	Non-zero elements	#JAMPS
4	6 (6)	6
5	11 (24)	24
6	24 (120)	70
7	50 (720)	180
8	95 (5040)	413
9	166 (40320)	856
10	271 (362880)	1629
11	419 (3628800)	2890
12	620 (39916800)	4840
13	885 (479001600)	7728
14	1226 (6227020800)	11856

Table 5: For the colour matrix in the fundamental representation, the number of non-zero elements in one row (middle column) and total number of rows (middle column parenthesis) and number of dual amplitudes (right column) that need to be computed when a NLC truncation and final state symmetry is utilized for one-quark line amplitudes with n gluons, for a $q\bar{q}$ initial state (left table), qg initial state (middle table) and gg initial state (right table).

$q\bar{q} \rightarrow n$ -gluon			$qg \rightarrow q + (n-1)$ -gluon			$gg \rightarrow q\bar{q} + (n-2)$ -gluon		
n	Non-zero elements	#JAMPS	n	Non-zero elements	#JAMPS	n	Non-zero elements	#JAMPS
2	6 (6)	3	2	6 (6)	2	2	6 (6)	2
3	11 (24)	5	3	11 (24)	6	3	11 (24)	6
4	24 (120)	11	4	24 (120)	22	4	24 (120)	24
5	50 (720)	25	5	50 (720)	68	5	50 (720)	116
6	95 (5040)	52	6	95 (5040)	180	6	95 (5040)	444

only reduce some terms in the columns of the colour matrix, but also reduce the number of rows needed in the computation. This implies also that the number of needed dual amplitudes can be reduced, even at LC. The total number of colour-ordered amplitudes

(called JAMPS to follow notation from MadGraph5_aMC@NLO) that need to be computed for all-gluon amplitudes is given in Table 4. For the all-gluon case, the choice of the rows to keep is redundant. However, for processes with quarks involved, a choice is to be made which rows are to be kept for evaluation, and different choices lead to different efficiencies in the number of dual amplitudes that must be computed. The number of needed dual amplitudes with one quark line and n gluons is presented in Table 5. As can be seen from the tables, evidently, the number of dual amplitudes needed for computation is the least when all gluons are in the final state (left-most table), as then most final state symmetry can be utilized for the reduction of the number of dual amplitudes.

The aim of paper III is to investigate the colour matrix at NLC accuracy, by finding the rules on how to obtain the locations of the NLC elements in the colour matrix. When the locations are obtained, the sparseness of the matrix is evaluated and compared in the fundamental, colour-flow and adjoint representations.

All the above is valid for tree-level colour decompositions. A similar procedure can in principal be done involving loops, at a higher perturbative order. In that case, the loop diagrams interferes with the Born ones, and this results in general in a non-square colour matrix, because the loop amplitudes have a different number of dual amplitudes in the colour expansion. The complication of an analytical evaluation of the location of the leading- N_c terms in the colour matrix is minor, but needs careful analysis.

3 Monte Carlo collider physics

“If you cannot be a star in the sky - be a lantern in the house.”

— Hungarian proverb

Even with the greatly simplifying tool of Feynman diagrams, calculating cross sections at high precision is a tedious and numerically challenging problem. With an increasing computing power, the past decades have employed many physicists with developing computational tools for the simulation of particle interactions. In this section, first an overview of the Monte Carlo integration technique is given. Then, the structure of higher order perturbation calculations is presented. Finally, event generators are discussed, with a special emphasis on the matrix-element generator `MadGraph5_aMC@NLO`, which is the main tool for the computations performed in the papers of this thesis.

3.1 Monte Carlo integration

In the quantum field theoretical formulation of particle physics, the differential cross section of a process is given by the integration over the allowed final-state phase space, as presented in Eq. (44). The integrated cross section,

$$\sigma = \int d\sigma \sim \int |\mathcal{M}|^2 \prod_{i=1}^n \frac{d^3 \mathbf{p}_i}{2E_i (2\pi)^3} \quad (99)$$

is a $(3n - 4)$ -dimensional integral in phase space⁶. The limits of integration depend on the particle kinematics, however, with variable substitution, it can in general be re-cast into an integral over a unit hypercube in $3n - 4$ dimensions, $]0, 1[^{3n-4}$.

To solve the above integral analytically becomes impossible for other than LO and low-multiplicity processes, as the matrix-element can be a complicated function of the phase-space variables. Therefore, numerical methods must be employed to compute the integral. Most numerical integration techniques based on quadrature methods have a dimension-dependent error and hence become less efficient when n becomes sizable. The Monte Carlo integration technique, however, is a statistical integration method, that is based on the law of large numbers in probability theory,

$$\int_0^1 f(x) dx = \lim_{N \rightarrow \infty} \frac{1}{N} \sum_{i=1}^N f(x_i), \quad x_i \in]0, 1[\quad (100)$$

⁶Plus 2 dimensions for the integration over the longitudinal momentum fraction x_i variable for the two partons in the factorized cross section for hadron collisions.

with the points x_i distributed flat in the interval. The integration region of an arbitrary integral can always be rescaled to match this unit interval by variable substitution. The full integral approximation is

$$\int_0^1 f(x)dx = \lim_{N \rightarrow \infty} \left(\frac{1}{N} \sum_{i=1}^N f(x_i) \pm \sqrt{\frac{1}{N}} \sqrt{\sum_{i=1}^N |f(x_i)|^2 - \left(\sum_{i=1}^N f(x_i) \right)^2} \right) \quad (101)$$

meaning that the decrease of the error of this approximation scales as $\frac{1}{\sqrt{N}}$ and is independent of the dimension of the integration. Therefore, this technique becomes very useful for high-dimensional integration and is thus the tool used for the computation of cross sections and for simulation of particle collisions on the computer.

Monte Carlo integration can be made more efficient by various improvements. One of the major methods is importance sampling, where the sampled points x_i are not uniformly distributed in the interval as in the conventional Monte Carlo method, but are sampled according to a known overestimate distribution. This essentially leads to a smaller variance, given in the square root expression in Eq. (101). Adaptive integration is another method for the improvement of the Monte Carlo method. The main idea here is dividing up the integration interval into grids from which the points are sampled, in a way that each grid contributes roughly similarly to the integral. This means that where the integrand is large or varies rapidly, a denser grid is set up. This method is often combined with importance sampling and the two are, for instance, implemented in the FORTRAN-based programs of VEGAS [17] and MINT [18] which are frequently used as the internal integrators in event generators.

Yet another greatly simplifying modification is multi-channel integration. Within this method, the integral is divided into regions in a way that each region includes one (or few) peaked regions of the integrand function. When applied in particle physics, the integral of the square of the matrix-element is rewritten,

$$\int \underbrace{\frac{\sum_i |\mathcal{M}_i|^2}{\sum_j |\mathcal{M}_j|^2}}_{\approx 1} |\mathcal{M}|^2 = \sum_i \int |\mathcal{M}_i|^2 \underbrace{\frac{|\mathcal{M}|^2}{\sum_j |\mathcal{M}_j|^2}}_{\approx 1} \quad (102)$$

where the integral is divided into a sum of the $i = 1, 2, \dots, n$ channels, each with its own integral to solve. The division is based either on single diagrams or groups of diagrams with similar peak structure. The approximation that the full squared matrix-element is roughly the sum of the square of the diagrams (neglecting the interference effects) allows to probe each channel by its own pole structure for each (group of) diagram contribution $|\mathcal{M}_i|^2$, effectively decoupling the peaks into separate integrals. This method is the single-diagram-enhanced multi-channel integration which is utilized in, for instance, MadGraph5_aMC@NLO.

3.2 Perturbative fixed-order expansion

In the high-energy regions, the matrix-element is computed as a sum of Feynman diagrams which contribute at a certain order in perturbation theory. When the terms included in the matrix-element are of a strict perturbative order, we speak of fixed-order expansion. The NLO contributions to the matrix-element have two origins at diagram-level: real corrections, in which an extra particle is emitted, and virtual corrections, in which a virtual extra particle is exchanged in a loop. As an example, we take the process $q\bar{q} \rightarrow q\bar{q}$ and write some of the Feynman diagrams contributing to the matrix-element at order $\mathcal{O}(g_1^4)$,

$$\mathcal{M} = \underbrace{\text{Born} \sim g_1^2}_{\text{Born} \sim g_1^2} + \underbrace{\text{real} \sim g_1^3}_{\text{real} \sim g_1^3} + \underbrace{\text{virtual} \sim g_1^4}_{\text{virtual} \sim g_1^4} + \dots \quad (103)$$

with the order of the strong coupling constant g_1 explicitly denoted for each diagram. When considering the squared matrix-element, $\mathcal{M}^*\mathcal{M}$, there are squared diagrams and interference terms between the diagrams of various orders in g_1 . The LO contribution for this process is of order α_s^2 (from squaring the Born diagrams) and the NLO contribution is of order α_s^3 . Combining the possible diagrams and g_1 coupling orders from Eq. (103), the possible contributions to the $\alpha_s^3 \sim g_1^6$ terms is obtained from two types of interferences:

$$\begin{aligned} \text{real} \times \text{real} : & \quad \text{and} \\ \text{Born} \times \text{virtual} : & \end{aligned} \quad (104)$$

Before investigating the fixed-order expansion in more detail, we first make a note that the notion of the perturbative orders for fixed-order expansion can be ambiguous. For example, the transverse momentum of the $t\bar{t}$ system in the process $pp \rightarrow t\bar{t}$ at order α_s^2 vanishes. At order α_s^3 it obtains non-zero values, when an additional particle acts as a recoil to the $t\bar{t}$ system. Thus, at LO, the transverse momentum of the $t\bar{t}$ pair, $p_T(t\bar{t})$, vanishes and one may therefore define the LO for this specific observable to be of order α_s^3 . Other observables for the process, such as the invariant mass of the $t\bar{t}$ system, or the transverse momentum of the t and \bar{t} separately, are LO observables at α_s^2 .

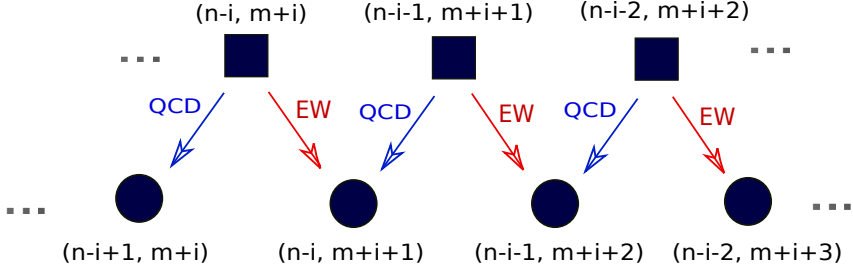


Figure 3: Expansion in mixed QCD and EW couplings at leading order (first row, boxes) and NLO (second row, blobs). In parentheses are noted the exponents (n, m) for each order $\alpha_s^n \alpha^m$.

Now we consider both of the coupling constants which are present for the Standard Model: the strong coupling α_s and the electroweak coupling α . One possible way [19] of defining a fixed-order perturbative expansion of a general observable \mathcal{O} in the two couplings is

$$\mathcal{O}(\alpha_s, \alpha) = \alpha_s^{c_1} \alpha^{c_2} \sum_{q=0}^{\infty} \sum_{k=0}^{\rho_0+q} \alpha_s^{\rho_0+q-k} \alpha^k \mathcal{O}_{c_1+\rho_0+q-k, c_2+k} \quad (105)$$

where ρ_0, c_1, c_2 are process-specific parameters. The leading-order contribution is defined as the $q = 0$ terms:

$$\begin{aligned} \mathcal{O}_{\text{LO}} = & \underbrace{\alpha_s^{c_1+\rho_0} \alpha^{c_2} \mathcal{O}_{c_1+\rho_0, c_2}}_{\text{LO}_1} + \underbrace{\alpha_s^{c_1+\rho_0-1} \alpha^{c_2+1} \mathcal{O}_{c_1+\rho_0-1, c_2+1}}_{\text{LO}_2} \\ & + \dots + \underbrace{\alpha_s^{c_1} \alpha^{c_2+\rho_0} \mathcal{O}_{c_1, c_2+\rho_0}}_{\text{LO}_{\rho_0-1}}. \end{aligned} \quad (106)$$

Given the size of the couplings, $\alpha_s^2 \approx \alpha$, and $\alpha_s \ll 1$, $\alpha \ll 1$, this perturbative series is convergent (the cases with large logarithms are discussed later in this section), hence, the leading-order terms satisfy

$$\Sigma_{\text{LO}_1} \gg \Sigma_{\text{LO}_2} \gg \dots \gg \Sigma_{\text{LO}_{\rho_0-1}}, \quad (107)$$

which defines a leading LO term (LO_1) and further subleading LO terms ($\text{LO}_2, \text{LO}_3, \dots$). Often, by LO is meant the first term only in this series, sometimes also referred to as LO QCD.

Similarly, the NLO contributions are the $q = 1$ terms;

$$\begin{aligned} \mathcal{O}_{\text{NLO}} = & \underbrace{\alpha_s^{c_1+\rho_0+1} \alpha^{c_2} \mathcal{O}_{c_1+\rho_0+1, c_2}}_{\text{NLO}_1} + \underbrace{\alpha_s^{c_1+\rho_0} \alpha^{c_2+1} \mathcal{O}_{c_1+\rho_0, c_2+1}}_{\text{NLO}_2} \\ & + \dots + \underbrace{\alpha_s^{c_1} \alpha^{c_2+\rho_0+1} \mathcal{O}_{c_1, c_2+\rho_0+1}}_{\text{NLO}_{\rho_0}} \end{aligned} \quad (108)$$

with the same convergent behavior

$$\Sigma_{\text{NLO}_1} \gg \Sigma_{\text{NLO}_2} \gg \dots \gg \Sigma_{\text{NLO}_{\rho_0}}. \quad (\text{I09})$$

Higher order corrections are obtained similarly, NNLO ($q = 2$), N³LO ($q = 3$) and so on. An alternative notation is to denote each order of contribution $\alpha_s^n \alpha^m$ with (n, m) such that their sum $n + m = A$ for LO, $n + m = A + 1$ for NLO, and so on. The upper and lower limits of n, m and A are process-specific. The tower of contributions can be portrayed for the LO and NLO terms as in Figure 3. Here, the QCD (red) and EW (blue) arrows indicate if the corresponding NLO correction is obtained as QCD correction or EW correction to a LO term. Some NLO blobs can therefore be reached both as a QCD correction to a LO term or an EW correction of the LO term of one order higher. Complete-NLO corrections are those in which all NLO terms are included and summed.

The hierarchical structure of the fixed-order perturbation expansion can be spoiled. As an example, we consider photon radiation from a charged particle. When including all initial and final state soft radiation, the leading-order differential cross section $d\sigma_0$ is corrected by an exponential Sudakov form factor,

$$d\sigma = d\sigma_0 \times e^{-\frac{\alpha}{\pi} \log\left(\frac{Q^2}{m^2}\right) \log\left(\frac{Q^2}{E^2}\right)}. \quad (\text{II0})$$

This Sudakov form factor describes the probability of not emitting a photon of energy E . Indeed, when $E \rightarrow 0$, this probability goes to 0, that is, it is impossible to not emit arbitrarily soft photons. Expanding the form factor yields a perturbative expansion where the coupling constant is accompanied by double logarithms at each order on the form

$$\left(\alpha \log\left(\frac{Q^2}{m^2}\right) \log\left(\frac{Q^2}{E^2}\right) \right)^n. \quad (\text{III})$$

Here, the scale Q is the scale of interaction, m is the mass of the particle emitting the soft photons. Hence, the expansion in the coupling is well-behaved provided the logarithms are small. In the regions where the logarithms are large, the expansion is spoiled and one cannot assume a hierarchy between the perturbative fixed-order expansion terms. In these cases, a resummation in the logarithms must be performed at each perturbative order: this is remedied with analytical resummation or with parton showers.

Another case when the hierarchies between the orders might be altered is when a higher-order correction opens up channels of initial state which are not included in the leading-order set of channels. Such is the case in the NLO QCD corrections to $t\bar{t}W$ production when the qg channel opens up at NLO QCD, compared to the only initial state $q\bar{q}$ at LO [20]. This can lead to artificially large NLO corrections. Similarly, when NLO EW are considered, photon-initiated channels, although suppressed with powers of α , might yield artificially large electroweak corrections.

The combination of NLO QCD and EW corrections on top of the Born prediction are defined in two ways. To demonstrate this, we consider a case with a single LO term and one NLO QCD and one NLO EW term (one square and two blobs according to Figure 3). Given the relative NLO QCD and NLO EW corrections, δ_{QCD} and δ_{EW} respectively, an observable at these perturbative orders is

$$\begin{aligned}\mathcal{O}_{\text{NLO QCD}} &= \mathcal{O}_{\text{LO}} (1 + \delta_{\text{QCD}}), \\ \mathcal{O}_{\text{NLO EW}} &= \mathcal{O}_{\text{LO}} (1 + \delta_{\text{EW}}),\end{aligned}\tag{II2}$$

and the commonly used K -factors are

$$\begin{aligned}K_{\text{NLO QCD}} &= \frac{\mathcal{O}_{\text{NLO QCD}}}{\mathcal{O}_{\text{LO}}} = 1 + \delta_{\text{QCD}}, \\ K_{\text{NLO EW}} &= \frac{\mathcal{O}_{\text{NLO EW}}}{\mathcal{O}_{\text{LO}}} = 1 + \delta_{\text{EW}}.\end{aligned}\tag{II3}$$

The complete NLO for this example is defined either in the additive approach, in which we speak of NLO QCD+EW,

$$\mathcal{O}_{\text{NLO QCD+EW}} = \mathcal{O}_{\text{LO}} (1 + \delta_{\text{QCD}} + \delta_{\text{EW}})\tag{II4}$$

or in the multiplicative approach, in which we speak instead of NLO QCD \times EW,

$$\begin{aligned}\mathcal{O}_{\text{NLO QCD}\times\text{EW}} &= \mathcal{O}_{\text{QCD}} (1 + \delta_{\text{EW}}) \\ &= \mathcal{O}_{\text{LO}} (1 + \delta_{\text{QCD}}) (1 + \delta_{\text{EW}}).\end{aligned}\tag{II5}$$

Although the perturbative expansion is valid in both cases, the final results for the observable may differ. In addition, one may evaluate the difference between the two approaches, $\mathcal{O}_{\text{LO}}\delta_{\text{QCD}}\delta_{\text{EW}}$ to evaluate the size of further corrections at the given order. Specifically, the multiplicative approach includes an approximation to the higher order EW corrections, while this is omitted in the additive approach. This makes the multiplicative approach less sensitive to the scale variation. This feature is nicely portrayed in $t\bar{t}$ production in Ref. [21]. The additive approach may, however, be preferred when the orders need to be sorted and kept track of.

When considering observables which are expressed as ratios of other observables, the situation becomes more subtle. This is the case in paper II and paper IV, where spin correlation coefficients and angular coefficients are considered, respectively, where the considered observables are of the general form

$$R = \frac{N}{D},\tag{II6}$$

where the numerator N and denominator D is expanded at NLO in α and α_s separately, but no mixed terms of $\alpha_s\alpha$ are included,

$$N = \underbrace{N_0 + \alpha N_3}_{=N_2} + \alpha_s N_1, \quad (\text{II7})$$

$$D = \underbrace{D_0 + \alpha D_3}_{=D_2} + \alpha_s D_1. \quad (\text{II8})$$

The unexpanded approach for the perturbative expansion of the ratio is to compute the numerator and denominator separately at this order and take the quotient. The expanded approach, on the other hand, is to first expand the ratio in the α_s coupling,

$$R = \frac{N_1}{D_1} + \alpha_s \frac{N_2 D_1 - N_1 D_2}{D_2^2}, \quad (\text{II9})$$

and secondly to expand N_2, D_2 in the α coupling, leading to

$$R = \frac{N_0}{D_0} + \alpha \frac{N_3 D_1 - N_1 D_3}{D_3^2} + \alpha_s \frac{N_2 D_1 - N_1 D_2}{D_2^2} + \alpha_s \alpha \frac{N_2 D_3 - N_3 D_2}{D_2^2}, \quad (\text{I20})$$

where the term marked with red is formally of the mixed-coupling order, which is technically excluded from the computation. Hence, this term should be omitted, otherwise misleading results might be obtained. A similar situation⁷ arises in paper II where compete-NLO corrections are considered, and paper IV where NNLO QCD corrections are combined with NLO EW corrections.

3.3 More on NLO EW corrections

When considering electroweak corrections, one must be careful about treating the emitted soft or collinear photon correctly. In the real radiation diagrams, photons can be emitted collinear to a charged fermion line. As such, demanding a fixed number of photons in the final state is not infrared safe. This introduces the concept of dressing leptons, also called photon recombination. Dressed leptons (and quarks) are those final state fermions which have been recombined with any photon that satisfies an angular separation of R in the (η, ϕ) -plane (the definition of the angular separation is given in Section 4). After recombination, the photon momentum is added to the dressed fermion momentum and is removed as a final state particle. This should be done whenever NLO EW corrections are considered.

Electroweak corrections at NLO are typically of the size $\mathcal{O}(\alpha) \sim 1\%$. However, they can have larger effects in some cases. Firstly, this can be due to opening up of photon-induced

⁷In paper I, only the additive and unexpanded approach is used for the coefficients for the combination of NLO QCD and NLO EW corrections.

channels, as discussed earlier. Secondly, the bremsstrahlung contributions of photons can make a significant impact. This is the emission of final state photons, and hence is also called the photon final state radiation. The third main contribution to larger NLO EW corrections is from the emission of massive gauge bosons, which is different from the case when emitting massless photons. These bosons have a finite mass and hence are detectable objects. As such, their real radiation is treated as a physically distinguishable process and the cancellation between the real and virtual correction does not take place, in a physically meaningful way. Another way of viewing this non-cancellation is through the weak charges. In an interaction initiated by a strongly charged particle, the colour charge is summed over. However, the weak charges of the initial particles are not summed and averaged, as we consider a quark of a specific flavour, which is only one of the entries in the weak doublets. This breaking of the weak gauge group symmetry in the initial state leads to that these corrections between the real and virtual corrections in the weak sector are not canceled. The result of the weak boson corrections are the virtual contributions, and these are evaluated to enhancements on the form $-\alpha \log^k \frac{s}{m_V^2}$ and are relevant when $s \gg m_V^2$, with the hard scattering scale s and the weak boson mass m_V (either m_W or m_Z) and $k = 1, \dots, 2n$. If these corrections are large, resummation must be made in order to achieve precise results. For NLO EW ($n = 1$) involving one-loop corrections, there are two main contributions: the double logarithms ($k = 2$), known as leading (EW) Sudakov logarithms and the single logarithms ($k = 1$), known as the subleading ones [22].

The double-logarithmic Sudakov enhancement and single-logarithmic Sudakov enhancement for the NLO EW one-loop corrections of the forms

$$\frac{\alpha}{4\pi} \log^2 \left(\frac{s}{m_V^2} \right) \quad \text{and} \quad \frac{\alpha}{4\pi} \log \left(\frac{s}{m_V^2} \right) \quad (121)$$

reach up to $\sim 8\%$ and $\sim 1\%$, respectively, for the LHC with $s = (13 \text{ TeV})^2$. For proposed future facilities at higher energies, such as the Future Circular Collider (FCC) with a proposed center of mass energy of 100 TeV, these corrections can be even more dominant.

The double- (and single-) logarithmic Sudakov enhancements originate from the Feynman diagrams and logarithms of the form

$$\log^2 \frac{r_{ij}}{m_V^2} \quad (122)$$

with the invariants r_{ij} formed between the external particle momenta p_i, p_j [23, 24]. The region where the NLO EW corrections can be approximated by the simple Sudakov enhancements is in the region where all invariants $r_{ij} = (p_i + p_j)^2$ are large compared to the weak scale, $r_{ij} \gg m_{W/Z}^2$. In other regions, this Sudakov approximation to the NLO EW corrections breaks down. Therefore, in resonance diagrams where the internal boson is on-shell, the one-loop Sudakov approximation to the NLO EW corrections is a priori

not valid. One possible remedy is to use reweighting of events to obtain the Sudakov approximations before the decay of the on-shell resonance takes place.

3.4 Event generators

The way to compute and simulate full hadronic collisions in which a hard scattering takes place, is through a chain of events, spanning over a large energy scale, each stage in need of separate modeling or calculation, as portrayed for a hadron-hadron collision in Figure 4. The red arch in the figure denotes the hard scattering part, which occurs at the highest energy transfer between partons and results in a final state with some relatively low number of partons. This is the partonic interaction and can most often be computed with perturbation theory. The final partonic state is then dressed with soft and collinear emissions, and in this way propagated down from the hard scale to some hadronization scale, represented by the green arch in the figure. At this scale, the coloured partons are combined into colourless bound states of hadrons, marked with green blobs. Unstable hadrons are further decayed to stable hadrons (dark green blobs). It is this final state of sprays of stable hadrons which are detected in a detector at a hadron collider. For the simulation of this entire chain of processes, multi-purpose event generators have been developed. These are often interfaced to other programs, which have a more specific focus on one aspect of the collision. This is the case with matrix-element generators, which often have high precision computation of the hard scattering implemented, and are interfaced to the parton shower and hadronization modeling of the multi-purpose event generators. The three largest multi-purpose event generators today are PYTHIA8 [25], HERWIG7 [26] and SHERPA [27]. Predictions obtained with these tools are often also passed through a detector simulation, that produces results which finally can be compared to experimental data.

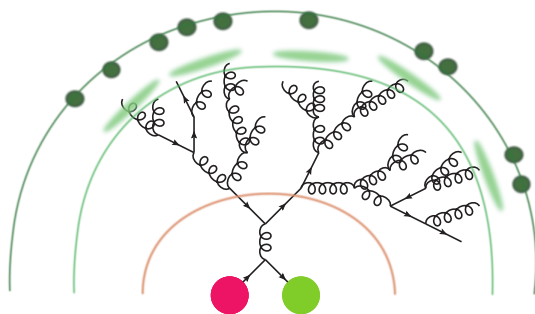


Figure 4: Schematic figure of a scattering event portraying the hard scattering (red arch), the soft emissions (up to light green arch), the hadronization into unstable hadrons (light green blobs) and finally the decay to stable hadrons (dark green blobs).

Scale uncertainties

Within the factorization approach for hadron collisions, the factorization scale μ_F enters the computation. When higher than LO is considered in the hard scattering computation, also the renormalization scale μ_R enters the calculation. Although these scales are unphysical, the accuracy of the calculations relies partly on what values are chosen for them. Generally, one needs to pick values which are on the order of the hard process: large ranges of scales in a process leads to large logarithms and ill-behaved convergent series in the region where perturbation theory is applied. The effect of the scale choice is conventionally evaluated by a 7- or 9-point variation of the scales by varying the central value for both the renormalization and factorization scales by factors in the range of $\{\frac{1}{2}, 1, 2\}$ and performing an envelope over these values. The scale uncertainties, when correctly computed, indicates the size of the missing higher order effects.

PDF sets and uncertainties

Presently, the most widely used distributor of PDF sets is the LHAPDF [28] library. In this library, almost all PDF data are collected from different collaborations, providing an interface between PDF data and event generators. The PDF sets consist of a (x, Q) grid, and interpolation schemes allow for a continuous usage in event generators. PDF sets are computed by fits to data of a parametrized model with a set of parameters, and this fit of the parameters is performed differently for the different PDF groups, but all are based on some χ^2 -fit. Some collaborations, such as the NNPDF collaboration [29], utilizes a neural network fitting of data to the DGLAP evolution equations. Together with the central values, modern PDF sets are presented with a set of uncertainties on the fitted parameters, which can be used directly in the evaluation of the PDF uncertainty dependence of the computations. These uncertainties are often the largest source of error in theoretical predictions.

In recent years, the photon PDF in the proton has received much attention. One of the collaborators focusing on the photon content is LUXqed [30], using points from electron-positron scattering to obtain the structure functions for the photon content. The LUXqed also defines a formalism to obtain the photon contribution, and is used by other collaborations, such as the NNPDF collaboration, to obtain PDF sets with a more reliable and correct photon content, implemented in, for example, the NNPDF3.1-luxQED set [31].

Introducing MadGraph5_aMC@NLO

The matrix-element generator MadGraph5_aMC@NLO [32] is a fully automated program that computes hard scattering processes with NLO QCD and NLO EW precision. The NLO QCD precise results can be interfaced to parton showers, through the MC@NLO

matching prescription. As such, the program can either do event generation (with parton shower matching) or a fixed-order computation, in which only the hard scattering partonic process is computed. The rough outline of an event file generation is described in the flow chart in Figure 5. As the first step, the user defines the model to use for the process, and defines the process to generate. The physics model input is produced with the `FeynRules` interface [33], a Wolfram Mathematica script which generates the Feynman rules from the given Lagrangian. The translated Feynman rules are contained in a UFO (Universal FeynRules Output) file [34], containing the generated parameters, vertices and propagators. Given this input, the information is passed on to ALOHA (Automatic Libraries of Helicity Amplitudes) [35], that generates libraries of calls to helicity amplitudes based on the set of Feynman rules, according to the HELAS library subroutines [36]. This provides the user a standalone process directory. With a numerical integration tool (currently MINT), phase-space points are sampled and the integral for the cross section is computed. The phase-space points are either passed through an on-the-fly analysis (for fixed-order generation) or, when the MC@NLO matching is used, summarized and stored in an LHE file. LHE files is a standardized way [37] of passing information from the parton-level process to the parton shower and hadronization tools, based on established LHA (Les Houches Accords) agreements [38].

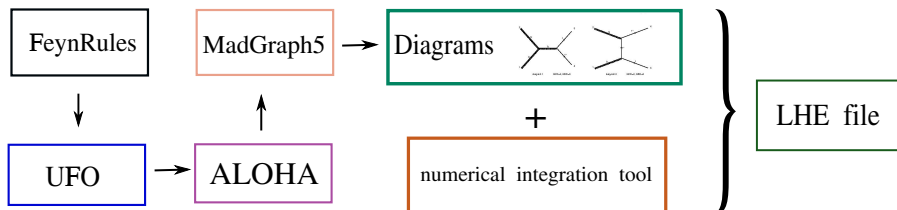


Figure 5: Flow chart of event generation, collected in an LHE file, in `MadGraph5_aMC@NLO`.

The phase-space events which are generated in this way are weighted, meaning that they have different weights. This, however, does not resemble real particle collisions, in which each event has the same weight, but occurs with different probability. To produce more realistic events, unweighting is applied, in which each event is given the same weight, while at the same time altering the number of events in each kinematic region, in order to maintain the same distributions. To be specific, given a set of N weighted events with weights $\{w_i\}$ summing to the total cross section

$$\sigma = \sum_{i=1}^N w_i, \quad (123)$$

the events can be unweighted if there exists an upper bound w_{\max} such that one can rewrite

$$\sigma = w_{\max} \sum_{i=1}^N \frac{w_i}{w_{\max}}, \quad (124)$$

where each event i is accepted with probability $\frac{w_i}{w_{\max}} < 1$ and then assigned the same weight w_{\max} . This method can be applied when the integrand is positive and bounded. Thus, this is not the case when NLO corrections are considered at fixed-order computations, where the matrix-element diverges in certain phase-space regions. However, when the NLO accurate predictions are matched to parton showers, this divergence is lifted and the unweighting procedure can be performed.

Further tools, such as the FKS-subtraction within MadFKS [39] for dealing with the divergent parts of the real and virtual corrections at NLO; the loop calculator MadLoop5 [40], together with CutTools [41] and other integral reduction methods [42–46], which calculate the loop contributions in dimensional regularization scheme for the virtual contributions, are utilized for a complete handling of fully automated NLO computations inside MadGraph5_aMC@NLO.

Dealing with the KLN theorem numerically at NLO

The IR divergences in the virtual and real diagrams in final state radiation cancel according to the KLN theorem, while a remainder finite part contributes to the total cross section. Treating this cancellation numerically can, however, be challenging. There are two main types of methods for implementing these IR cancellations: phase-space slicing methods and subtraction methods. The FKS-subtraction scheme introduced by Frixione-Kunszt-Signer [47], which is the scheme implemented in MadGraph5_aMC@NLO, is here briefly described.

A $2 \rightarrow n$ process is considered with massless final state particles. The (partonic) cross section at NLO is obtained from contributions from the Born, virtual and real emissions,

$$\hat{\sigma}^{\text{NLO}} = \int_n d\hat{\sigma}^B + \int_n d\hat{\sigma}^V + \int_{n+1} d\hat{\sigma}^R \quad (125)$$

where the number of final state particles in the integral is depicted: n for the Born and virtual contributions and $n + 1$ for the real emission contribution.

If the Born matrix-element is denoted with $\mathcal{M}_n^{\text{tree}}$ and similarly $\mathcal{M}_{n+1}^{\text{tree}}$ denotes the tree-level matrix-element from the real emission $2 \rightarrow n + 1$ diagrams, and $\mathcal{M}_n^{\text{loop}}$ the loop-level matrix-element with an n -body final state, then the various contributions to the cross

section are expressed as

$$\begin{aligned}
d\hat{\sigma}^B &\sim \sum_{\text{colour,spin}} |\mathcal{M}_n^{\text{tree}}|^2 d\Phi_n, \\
d\hat{\sigma}^R &\sim \sum_{\text{colour,spin}} |\mathcal{M}_{n+1}^{\text{tree}}|^2 d\Phi_{n+1}, \\
d\hat{\sigma}^V &\sim \sum_{\text{colour,spin}} 2\text{Re} \left[\mathcal{M}_n^{\text{loop}} (\mathcal{M}_n^{\text{tree}})^* \right] d\Phi_n,
\end{aligned} \tag{126}$$

where the proportionality factors omitted are the flux factors and the averaged colour factors for the incoming particles.

The three cases in which soft and collinear singularity occurs is when one of the massless final state particles is soft (its energy $E \rightarrow 0$), or when one of them goes collinear with the initial partons (angle $\theta \rightarrow 0$ between the two parton directions) or when two final state partons go collinear. In order to account for these divergence cancellations in the virtual and real emissions, a counter-term function (subtraction function) S is introduced in the integrals,

$$\hat{\sigma}^{\text{NLO}} = \int d\Phi_n \left(\hat{\sigma}^B + \hat{\sigma}^V + \int d\Phi_1 S \right) + \int d\Phi_{n+1} (\hat{\sigma}^R - S), \tag{127}$$

such that it incorporates the singular parts of the real emission and thus renders the integrals separately finite. This subtraction is introduced in a way that each of the soft and collinear singularities are isolated into separate regions, simplifying their structured computations.

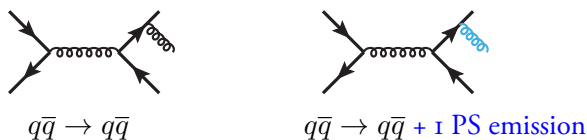
In this way, two type of events are generated: those with n -body kinematics, including the Born, virtual and counterterm contributions (denoted as **S** events), and events with $n + 1$ -body kinematics, which include the real emission and the counterterms (denoted as **H** events). For fixed-order computations, these are grouped into `eventgroups` in the output LHE files. These events are correlated and their weights partially cancel, therefore, the weights and errors should be combined accordingly when evaluating the error of the Monte Carlo calculation.

Matching matrix-element calculations with parton showers

The non-abelian nature of QCD leads to colour confinement at short distances, meaning that the strongly interacting objects are detected only as colourless bound states. But at short distances, perturbation theory for the description of QCD breaks down. Hence, different mathematical tools are to be used at high and low energies for the modeling of particle interactions. In the varying of energy scales, coloured objects emit collinear and

soft gluons and quarks. This process is typically simulated and computed through parton shower algorithms. These algorithms are Monte Carlo-based generators, which generate soft and collinear emissions of the final partonic state. These events are generated as Markov-chains, using the veto algorithm to include an ordering in energy. This way, the partonic final states are evolved from a hard scattering down to a low energy scale, where the parton shower is cut off and the final states are passed to hadronization models, that combine the particles into colourless hadrons.

The first, hardest emission of a parton shower to a partonic event may, however, recover the contribution of a real emission correction, already taken into account in a real-emission NLO diagram. This is exemplified in a hard-scattering real emission correction to quark-anti-quark pair production, $q\bar{q} \rightarrow q\bar{q}g$, and the first soft emission in the shower algorithm (marked in blue) to the tree-level $q\bar{q} \rightarrow q\bar{q}$ process,



which can be the same contribution for certain kinematic setups. In order to reduce this double-counting of contributions, a matching method must be employed. The two main matching prescriptions are the MC@NLO method [48] and the POWHEG method [49]. The former is an additive matching prescription, while the latter is a multiplicative matching. The current version of MadGraph5_aMC@NLO has automated matching of NLO QCD hard matrix-elements to the parton shower based on the MC@NLO framework. However, the NLO EW corrections are available currently only for fixed-order event generation.

Decaying resonances with MadSpin

Unstable particles which are created in the partonic process can be decayed within the multi-purpose event generator before the parton shower algorithm is applied. However, in most cases this approach for the decay does not consider spin correlations between the decay products. Within MadGraph5_aMC@NLO, the spin correlations can be included with the MadSpin module [50]. Although it has some limitation, it is an efficient approach to obtain spin-correlated decayed events which can be passed onto parton showers.

The method in MadSpin relies on the decay chain model. This is the two-step production of decayed events, by first producing a set of production events with final state unstable particles, and secondly by producing decay events for each of the unstable particles which are then attached to the production events [51]. The procedure in more detail is as follows: MadGraph5_aMC@NLO generates a set of production events in an LHE file, following the steps described above, with the final state resonance particles. Decays in the resonance

particles' rest frames are then generated at LO precision in a set of unweighted events. Each production event with kinematics Φ_{prod} is tested to a decay event with kinematics Φ_{dec} . This differential cross section is bounded from above

$$\frac{d\sigma}{d\Phi_{\text{prod}}d\Phi_{\text{dec}}} < B_{\text{max}} \quad (128)$$

for some value B_{max} . A proposed full event is generated by boosting the final state momenta to match the production kinematics to form the full kinematics Φ_{full} . An accept-or-reject method is applied by picking a random number $r \in [0, 1]$ and accepting the full kinematics Φ_{full} only if

$$\frac{d\sigma}{d\Phi_{\text{full}}} > rW_{\text{max}} \quad (129)$$

and otherwise proceeding to the next decay event until a decay event is accepted for each production event. To obtain this upper weight bound W_{max} , a set of N production events are probed at the beginning of the computation, with a set of n decay events each. For each, a maximum value w^i is obtained, and these are combined and averaged to obtain the upper bound weight,

$$W_{\text{max}} = \langle w^i \rangle + \xi \text{std}(w^i) \quad (130)$$

with some parameter ξ . The three free parameters ξ, N, n have been tested to various processes, presented in Ref. [50] to optimize the calculation for a general process.

For the evaluation of the differential cross section $\frac{d\sigma}{d\Phi_{\text{full}}}$, tree-level diagrams are used for the given phase-space point Φ_{full} . As such, events with Born-type kinematics (both Born-level and virtual events) obtain only leading-order correction to the spin correlation, while real-emission events obtain tree-level next-to-leading corrections. In other words, MadSpin approximates virtual spin-correlation effects with tree-level ones.

For making an estimation of finite width effects, MadSpin internally does a smearing procedure which captures the Breit-Wigner shape of the resonant particle around the mass peak. The way this is done is by picking a virtual invariant mass for the resonance randomly around the Breit-Wigner peak, then reshuffling the momenta for the undecayed event, before attaching the unweighted decay event. This method captures a part of the off-shell effects.

Reweighting in event generation

Generator-level events (those passed a parton shower algorithm and stored in an LHE file) are passed through detector simulations at a very high computational and memory cost.

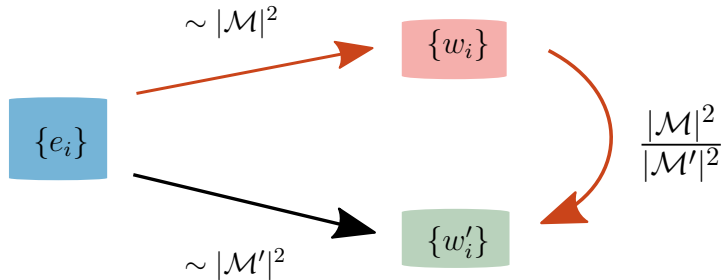


Figure 6: Schematic overview of the combined reweighting and unweighting procedures applied on parton-level events by a multiplication of the ratio of the matrix-elements squared.

Altering any parameter in the theory or model at generator level would in principle need a new passing of all generator-level events through the detector simulation. This tedious and computation-costly method can be avoided by the method of reweighting.

In leading-order reweighting [52], given a set of events with weights $\{w_i\}$, produced with the matrix-element \mathcal{M} , the same set of events (kinematics) can be multiplied with the ratio

$$\frac{|\mathcal{M}'|^2}{|\mathcal{M}|^2} \quad (131)$$

to obtain events with weights corresponding to a new physical scenario, in which the matrix-element \mathcal{M}' governs the physics instead. This simple method can be used because at leading order, the weights are given by

$$w_i = B(e_i^B) \Phi(e_i^B), \quad B(e_i^B) = f_1(x, \mu_F^2) f_2(x, \mu_F^2) |\mathcal{M}_B|^2, \quad (132)$$

omitting flux factors, and if the new scenario has the same kinematical setup, all factors cancel in the ratio between the weights except the matrix-elements. As such, if the model requires a change of $\alpha_s \rightarrow \alpha'_s$, $\alpha \rightarrow \alpha'$, $\mu_{R/F} \rightarrow \mu_{R'/F'}$, $f_i \rightarrow (f_i)'$, this simple factor in Eq. (132) is not enough for a re-sampling of events. But if the new model consists of for example different mass parameters or other input parameters appearing in the matrix-element only, the parton distributions and flux factors cancel and the reweighting is a simple factor of the matrix-elements (squared), evaluated at the phase-space point of each event.

Reweighting can be combined with unweighting of events. The weighted events $\{e_i\}$ can be unweighted, using the procedure described in Eq. (134). The total cross section for the old events, with unweighted weights $\{w_i\}$, changes in a new physics as

$$\sigma = \sum_{i=1}^N w_i \quad \rightarrow \quad \sigma' = \sum_{i=1}^N w'_i, \quad (133)$$

with a new set of unweighted events $\{w'_i\}$. These new events can be obtained directly in the procedure of unweighting the old events with the multiplication of the ratio of the weights,

$$\sigma' = w_{\max} \sum_{i=1}^N \frac{|\mathcal{M}'|^2}{|\mathcal{M}|^2} \frac{w_i}{w_{\max}}. \quad (134)$$

This combination of reweighting and unweighting is depicted in Figure 6, where the re-weight route is marked with red arrows.

At NLO, the procedure is less straightforward, as one obtains events of type $2 \rightarrow n$ to which both virtual and Born-level kinematics contribute, and also $2 \rightarrow n+1$ real emission events. As given in Eq. (125), there are various pieces in the NLO calculation which contribute to the integration and a careful reweighting must be done for the different type of events.

Reweighting in decay chains

Reweighting is applied in the decay chain model, developed for parton-showered events [51], for generating spin correlated events from a set of decay events with no spin correlation. This makes the calculation much more efficient and in many cases a very good approximation. In the NWA, there is a compact form in which one can relate the weight of a production event to the fully decayed event. This is exemplified with top quark pair production and decay into a 6-body final state. The full matrix-element of this process at leading-order is written

$$\mathcal{M}_{\text{full}} \sim \frac{1}{p_t^2 - m_t^2 + im_t\Gamma_t} \frac{1}{p_t^2 - m_t^2 + im_t\Gamma_t} \mathcal{M}_{\text{prod}} \mathcal{M}_{\text{dec}}, \quad (135)$$

with the two top/anti-top propagators, and the matrix-elements containing the production part, $\mathcal{M}_{\text{prod}}$, and decay part, \mathcal{M}_{dec} . The propagators in the squared matrix-element for the top and anti-top quark are replaced in the NWA by

$$\frac{1}{(p_t^2 - m_t^2)^2 + (m_t\Gamma_t)^2} \frac{1}{(p_t^2 - m_t^2)^2 + (m_t\Gamma_t)^2} \rightarrow \left(\frac{\pi}{m_t\Gamma_t}\right)^2 \delta(p_t^2 - m_t^2) \delta(p_t^2 - m_t^2). \quad (136)$$

The squared, colour- and spin-summed, matrix-element is expressed in this limit as

$$\sum_{\text{colour, spin}} |\mathcal{M}|^2 = \left(\frac{\pi}{m_t\Gamma_t}\right)^2 \sum_{ss'} \mathcal{M}_s^\dagger \rho_{ss'} \mathcal{M}_{s'} \delta(p_t^2 - m_t^2) \delta(p_t^2 - m_t^2), \quad (137)$$

where the sum over the top quark and anti-top quarks spins s and s' respectively, has been explicitly written out, and the spin-density operator ρ incorporates the spin states. The density operator can be diagonalized with a unitary matrix U

$$\rho = U^\dagger \rho^D U, \quad (138)$$

and the sum over the spins can be rewritten as

$$\sum_{ss'} \mathcal{M}_s^\dagger \rho_{ss'} \mathcal{M}_{s'} \rightarrow \sum_{ss'} (U \mathcal{M}_s)^\dagger \rho_{ss'}^D (U \mathcal{M}_{s'}). \quad (139)$$

As a positive-definite matrix, the density operator has an upper limit on its diagonal elements, and hence

$$\sum_{ss'} (U \mathcal{M}_s)^\dagger \rho_{ss'}^D (U \mathcal{M}_{s'}) \leq \max_s \rho_{ss}^D. \quad (140)$$

This leads to that the fully-decayed event is bounded from above

$$\frac{d\sigma}{d\Omega_{6(+1)}} \leq B_{\max} \frac{d\sigma}{d\Omega_{2(+1)}} \quad (141)$$

with a constant B_{\max} which depends on the kinematic structure of the matrix-elements, but calculable at any perturbative order. In parenthesis are denoted the real emission phase spaces, with one extra particle in the phase space. In practice, this upper bound can be obtained from a sample of production and decay events by sampling a set and retrieving the maximum value by a process described in Subsection 3.4.

Following this upper-boundedness of the fully decayed events, we use this reweighting method in paper II for a fixed-order event generation with the phase-space points gathered in `eventgroups`, performed at NLO QCD+EW precision, in order to pass weighted events obtained with electroweak corrections to a generation of spin-correlated decayed events.

4 Phenomenology at the Large Hadron Collider

“Where in the Schrödinger equation do you put the joy of being alive?”

— translation from Wigner Jenő

The leading particle accelerator in high-energy research today is the Large Hadron Collider (LHC), which is an underground circular collider located at the CERN science facility outside of Geneva. Its data taking at a center of mass energy of 14 TeV, which was planned to start in 2008, was postponed due to an unforeseen technical problem. This led to a later start in 2010 and with a reduced total energy of 7 TeV. The plethora of high-energy processes and final states which has been observed at the LHC is enormous. High performance and precision tracking and calorimetric techniques allow for accurate determination and reconstruction of final state particles, their kinematics and tracks.

In this section, after some general introduction to the LHC and its detectors, the processes investigated in the papers of this thesis are presented. Firstly, the very important and well-established Drell-Yan production, the topic of paper I and paper IV, is described. Secondly, a more recently detected process, the top quark pair production is considered, as the main focus of paper II is examining the spin correlation coefficients related to the top quark pair production. Finally, an introduction is given to jets and multi-jet events, which is the prominent background at the LHC and is the main target of the tools that paper III lays the foundation for.

4.1 The Large Hadron Collider and its detectors

The LHC, located underground on the border between Switzerland and France, is a circular collider of hadrons. The primary collision type is that of colliding proton bunches, although also heavy ions (lead nuclei) have been collided in p-Pb and Pb-Pb collisions.

The four main experiments at LHC are ATLAS, CMS, ALICE and LHCb. The former two are general-purpose detectors, while the ALICE experiment is specialized in heavy ion collisions and LHCb is a dedicated experiment for bottom quark physics. During data taking, these experiments record the number of signals N of some type. From this number, the cross section for that given type is deduced through the relation

$$\frac{dN}{dt} = \sigma \times \mathcal{L}, \quad L = \int \mathcal{L} dt = \frac{N}{\sigma}, \quad (142)$$

where \mathcal{L} denotes the luminosity (measured in $\text{b}^{-1}\text{s}^{-1}$) and L is the integrated luminosity, which is a specific value for a certain machine, like the center of mass energy it operates

at. When experiments search for some specific signal, the methodology in general is to compute

$$\sigma = \frac{N_{\text{signal}} - N_{\text{background}}}{\epsilon L}, \quad (143)$$

where N_{signal} is the obtained count for the signal, $N_{\text{background}}$ is any underlying Standard Model process which is not the signal one is looking for but with the same signature (this is called background), and ϵ is a selection efficiency of the given signal, obtained from calibration.

The particles which are present in theoretical simulations are often not the objects that can be detected at experiments. The detectable objects are called particle-level objects and are those which have a lifetime of over 0.3×10^{-10} s. In addition, they have to be within the kinematic ranges which the detector covers (this can be different for the different experiments). The first type of particle-level objects are photons and electrons. These are detected in the electromagnetic calorimeter, which measures the (electromagnetic) interaction of these particles with the matter in the detector. As a registered electron may have emitted photons which alters its kinematics, we typically refer to such leptons as dressed leptons. Muons, on the other hand, are not detected in this area as, due to their much heavier mass, they pass through the electromagnetic calorimeters with very little energy lost to the surrounding. Instead, they are detected at designated muon detectors, which are located in the outmost layer of the detectors. Therefore, we speak of muons as bare leptons, as the radiated photons are typically not altering the detected 4-momentum of the muon. The tau is a particle with a very short lifetime and hence is not directly detectable at the detectors. However, in more recent analyses, it has been reconstructed and identified in data.

The other set of objects which can be directly detected at the LHC experiments are the hadronic jets. Strongly interacting particles radiate other strongly interacting particles in the soft and collinear limit with diverging probability, as described in Section 2. These emitted partons are converted at the hadronization scale into hadrons, which are further decayed into stable hadrons. The emerging collimated sprays of hadrons thus are not individually detectable, but are measured as energy deposits in the hadronic calorimeter and are detected as jets. The field of jet substructure works with identifying the underlying structure of these jets, such that more refined internal information of the particles can be extracted.

The kinematics of the detected particles or objects can be reconstructed using trackers. The common variables for reporting the kinematics are in terms of the rapidity,

$$y = \frac{1}{2} \log \frac{E + p_z}{E - p_z} \quad (144)$$

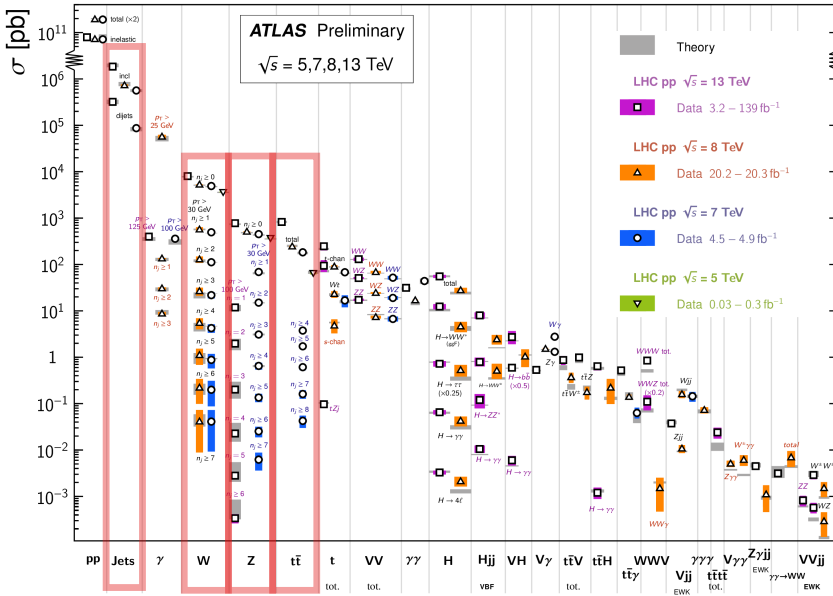


Figure 7: Figure with a summary of the most common Standard Model processes and their cross sections, measured at ATLAS. Figure is reproduced from ATLAS data repository https://atlaspo.cern.ch/public/summary_plots/.

and the related pseudo-rapidity,

$$\eta = -\log \left(\tan \frac{\theta}{2} \right) \quad (145)$$

where E is the energy of the particle, p_z is the component of the momentum along the beam axis (z -axis) and θ is the angle of the momentum with the beam axis. The difference in rapidity (or pseudo-rapidity) Δy ($\Delta \eta$) constitutes a Lorentz-invariant quantity along the beam axis. With these definitions, one constructs the angular separation in the (η, ϕ) -plane as

$$\Delta R = \sqrt{(\Delta \eta)^2 + (\Delta \phi)^2}, \quad (146)$$

where $\Delta \phi$ is the azimuthal angular distance between two objects. The reason for this way of defining the angular separation rather than in direct space is the unmeasured longitudinal momentum fraction that is carried by the fundamental partons inside the colliding hadron. Other commonly used observables are the transverse momentum $p_T = \sqrt{p_x^2 + p_y^2}$, invariant mass $p^2 = E^2 - |\mathbf{p}|^2$ or the angular separation $\cos \theta$ between two momenta.

Detectors measure objects in a limited phase space. This region is called the fiducial phase space, and varies between the different processes and experiments. On the theory side, various cuts can be imposed and in that way predictions can be made in the fiducial phase space to better match the experimental measurements. Experimental analyses do an unfolding to the inclusive phase space, by doing comparisons of the theory predictions (with detector simulations) between the fiducial and inclusive phase space and in that way extrapolate the measurements in the fiducial phase space to an inclusive one.

A summary of the most common processes and their cross sections, measured at the ATLAS detector, is presented in Figure 7. The four processes which have been addressed in the papers of the thesis are indicated in the table with red boxes. These processes are now introduced and discussed.

4.2 A key process at the LHC: Drell-Yan production

The production of a lepton pair at hadron colliders has been topic of interest for many years, with a first detection of both the weak bosons, the Z -boson and the W -boson, in 1983 at SPS at CERN [53, 54]. The process is generally termed Drell-Yan production, and comes either in a neutral-current setup (with a charged lepton pair in the final state), corresponding to a neutral Z -boson or photon production and later decay; and as a charged-current (with a charged lepton and its corresponding neutrino in the final state), with the production and subsequent decay of a charged W -boson, see Figure 8 for a schematic diagram. At leading order, this production comes solely from a quark and an anti-quark initiated partonic process. However, when higher order corrections are considered or the production with an associated extra emission at leading-order is considered, also gluon-initiated processes contribute. First a general introduction to both types of the Drell-Yan processes is given and then a more detailed discussion of each of them follow. As such, when lepton pair is mentioned, it can either be a pair of charged leptons, or one charged lepton and its corresponding neutrino, depending on the context.

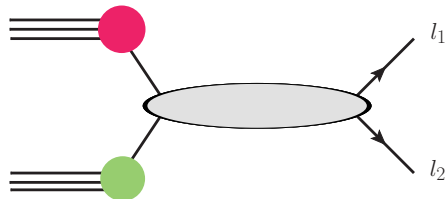


Figure 8: Schematic diagram of the Drell-Yan process. For the neutral-current setup, the outgoing particle pair is $(l_1, l_2) \in \{(e^-, e^+), (\mu^-, \mu^+), (\tau^-, \tau^+)\}$; while for the charged-current case, the pair is a charged lepton and its corresponding anti-neutrino, $(l_1, l_2) \in \{(e^-, \bar{\nu}_e), (\mu^-, \bar{\nu}_\mu), (\tau^-, \bar{\nu}_\tau)\}$ or with the opposite sign.

The process of interest for this thesis is the Drell-Yan production at finite weak boson transverse momentum. This corresponds to the process

$$p + p \rightarrow l_1 + l_2 + X \quad (147)$$

where X is some recoil against the lepton pair, yielding a non-zero value for the produced weak boson transverse momentum. The total cross section (and a generic IR-safe observable) for this process is expanded in the strong and electroweak couplings as

$$\begin{aligned} \sigma_{\text{LO}}(\alpha_s, \alpha) &= \underbrace{\alpha_s \alpha^2 \sigma_{1,2}}_{\text{LO}_1} + \underbrace{\alpha^3 \sigma_{0,3}}_{\text{LO}_2}, \\ \sigma_{\text{NLO}}(\alpha_s, \alpha) &= \underbrace{\alpha_s^2 \alpha^2 \sigma_{2,2}}_{\text{NLO}_1} + \underbrace{\alpha_s \alpha^3 \sigma_{1,3}}_{\text{NLO}_2} + \underbrace{\alpha^4 \sigma_{0,4}}_{\text{NLO}_3}. \end{aligned} \quad (148)$$

In paper I, the LO_1 term alone is referred to as LO. The NLO QCD correction is the $\text{LO}_1 + \text{NLO}_1$ terms, while the NLO EW correction include also the sub-leading LO term, $\text{LO}_1 + \text{LO}_2 + \text{NLO}_2$.

Specially interesting to investigate related to this process is the angular distribution of the final state leptons, as this probes the spin structure and the coupling structure between the weak boson and the leptons in the Standard Model. For the measurement of the lepton distribution, the Collins-Soper frame is used. The Collins-Soper frame is often preferred in analyses for both experiments and theory predictions of the process [55]. This frame is a rest frame of the weak boson, in which the axes are defined in the following way. In the hadron plane formed by the two incoming hadron momenta P_1, P_2 , the unit vector \hat{x} is defined to be the bisector of the two momenta and \hat{z} is an external bisector, in a way that the positive \hat{z} direction is in the positive direction of the (negatively) charged lepton in the laboratory frame, and the positive \hat{x} is in the opposite direction to the sum of the incoming hadron momenta. The system is completed to a Cartesian coordinate system with the unit vector \hat{y} normal to the hadron plane, see Figure 9.

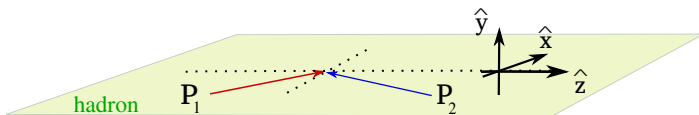
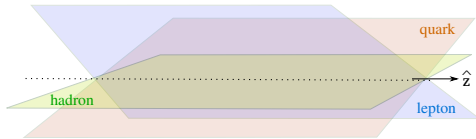


Figure 9: The hadron plane with the two incoming hadron momenta in the rest frame of the weak boson.

With a pointlike interaction, the lepton plane and quark plane bisect the hadron plane in the z -axis,



with the azimuthal angles Φ_1 and Φ , respectively. In the quark and lepton planes lie the quark momentum and the (negatively) charged lepton momentum, respectively. The polar angles θ_1 and θ are defined in the Collins-Soper frame, see Figure 10 for the definition of the angles. The angle θ_0 between the quark momentum (with unit vector \hat{p}_q) and lepton momentum (with unit vector \hat{p}_l) in this frame is defined through

$$\hat{p}_l \cdot \hat{p}_q = \cos \theta_0. \quad (149)$$

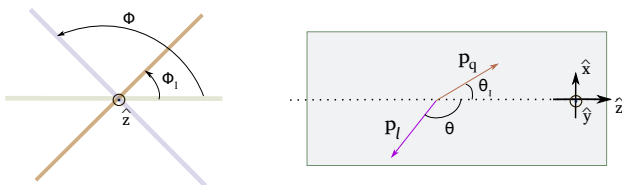


Figure 10: Azimuthal (left) and polar (right) angles of the (negatively) charged lepton and the quark.

To arrive at the definition of the decay coefficients of the Drell-Yan process, a more intuitive path is taken, which is valid for the neutral-current case. For this process, the differential cross section is expanded in terms of the angle θ_0 between the quark and lepton momenta,

$$\frac{d\sigma}{d\Omega} = \left(\frac{d\sigma}{d\Omega} \right)^{\text{unpol.}} (1 + a \cos \theta_0 + \cos^2 \theta_0) \quad (150)$$

with the unpolarized normalizing cross section factorized [55]. The origin of this expression is a summation of the various helicity configurations of the spin- $\frac{1}{2}$ quark and anti-quark pair into a vector boson: this simple argument yields the usual $1 + \cos^2 \theta_0$ dependence. The additional term proportional to the forward-backward asymmetry arises from the parity-violating coupling to the Z -boson. The angular distribution is azimuthally symmetric around the quark and anti-quark axis. To relate this expansion to the measurable angles Φ and θ , we make use of the relation

$$\cos \theta_0 = \cos \theta \cos \theta_1 + \sin \theta \sin \theta_1 \cos(\Phi - \Phi_1) \quad (151)$$

to rewrite the differential cross section in Eq. (150) in terms of (θ, Φ)

$$\begin{aligned}
\frac{d\sigma}{d\Omega} \sim & \left((1 + \cos^2 \theta) + \underbrace{\sin^2 \theta_1}_{A_0} \frac{1}{2} (1 - 3 \cos^2 \theta) + \underbrace{\left(\frac{1}{2} \sin 2\theta_1 \cos \Phi_1 \right)}_{A_1} \sin 2\theta \cos \Phi \right. \\
& + \underbrace{\sin^2 \theta_1 \cos 2\Phi_1}_{A_2} \frac{1}{2} \sin^2 \theta \cos 2\Phi + \underbrace{a \sin \theta_1 \cos \Phi_1}_{A_3} \sin \theta \cos \Phi + \underbrace{a \cos \theta_1}_{A_4} \cos \theta \\
& + \underbrace{\frac{1}{2} \sin^2 \theta_1 \sin 2\Phi_1 \sin^2 \theta \sin 2\Phi}_{A_5} + \underbrace{\frac{1}{2} \sin 2\theta_1 \sin \Phi_1 \sin 2\theta \sin \Phi}_{A_6} \\
& \left. + \underbrace{a \sin \theta_1 \sin \Phi_1 \sin \theta \sin \Phi}_{A_7} \right), \tag{152}
\end{aligned}$$

where the functions A_0, \dots, A_7 are scalar functions of the weak boson kinematics: the rapidity y_V , the transverse momentum $p_{T,V}$ and the invariant mass m_{ll} of the lepton pair, and are called angular coefficients (or decay coefficients). The coefficients are defined such that the remaining angular dependence in (θ, Φ) appear in the differential cross section as real spherical harmonics of degree up to $l = 2$ defined as

$$Y_m^l(\theta, \Phi) = \begin{cases} (-1)^m \sqrt{2(2l+1)} \frac{(l+m)!}{(l-m)!} P_{|m|}^l(\cos \theta) \sin(|m|\Phi) & m < 0, \\ \sqrt{2l+1} P_m^l(\cos \theta) & m = 0, \\ (-1)^m \sqrt{2(2l+1)} \frac{(l-m)!}{(l+m)!} P_m^l(\cos \theta) \cos(m\Phi) & m > 0, \end{cases} \tag{153}$$

with the associated Legendre polynomials $P_m^l(\theta, \Phi)$. In this definition, the spherical harmonics are orthogonal with the relation

$$\int Y_m^l(\theta, \Phi) Y_{m'}^{l'}(\theta, \Phi) d\Omega = 4\pi \delta_{mm'} \delta_{ll'}, \tag{154}$$

with which the coefficients A_0, \dots, A_7 can be projected out,

$$\begin{aligned}
A_0 &= 4 - 10 \langle \cos^2 \theta \rangle, & A_1 &= 5 \langle \sin 2\theta \cos \Phi \rangle, \\
A_2 &= 10 \langle \sin^2 \theta \cos 2\Phi \rangle, & A_3 &= 4 \langle \sin \theta \cos \Phi \rangle, \\
A_4 &= 4 \langle \cos \theta \rangle, & A_5 &= 5 \langle \sin^2 \theta \cos 2\Phi \rangle, \\
A_6 &= 5 \langle \sin 2\theta \sin \Phi \rangle, & A_7 &= 4 \langle \sin \theta \sin \Phi \rangle. \end{aligned} \tag{155}$$

The angled brackets indicate a weighted average of the function, normalized to the total cross section.

For the charged-current process, the same decomposition into scalar decay coefficients is made. However, the interpretation from the basic cross section in Eq. (150) is not valid, as

there is no term proportional to the parameter for the parity-odd coupling a . But, when a precise expansion of the cross section in terms of the hadronic and leptonic current is made, the final result with the same set of coefficients (but with different values) is obtained.

The decomposition in Eq. (152) is based on that the weak bosons decay in a $1 \rightarrow 2$ body process. Thus, when electroweak corrections are considered, this assumption is broken, as one may have $1 \rightarrow 3$ decays into a lepton pair and an additional photon (which is not present when only NLO QCD corrections are considered), or the decay parts may have virtual electroweak boson corrections. This mismatch is termed electroweak non-closure effect and is discussed in more detail in the appendix of paper IV.

The neutral-current process: producing and decaying a Z -boson

Within the Standard Model, this process at leading-order is the annihilation of a quark-anti-quark pair into a virtual photon or a Z -boson, which promptly decays to a charged lepton pair, with the final leptons being either an electron pair or a muon pair, both of which can be very well measured⁸. This process yields an insight into the hadron PDF and is in fact one of the key processes, along with deep inelastic scattering, for determining PDFs at the LHC, as well as further parameters such as the boson masses and widths. It is also one of the most abundant processes at the LHC (inclusive cross section of roughly 10^3 pb as can be seen from Figure 7) with a clear signature of two charged leptons.

The process can be investigated in various invariant mass m_{ll} ranges of the lepton pair: this invariant mass window sets a limit on which of the mediating bosons dominate the interaction. To investigate the Z -boson kinematics, it is customary to pick the invariant mass window

$$m_{ll} \in [80, 100] \text{ GeV} \tag{156}$$

as is done by analysis performed by ATLAS [56] and CMS [57], and is done in paper I. This (or any finite) lower cut on the lepton pair invariant mass is needed also in order to avoid a divergence in the Born diagram with the photon propagator: with $m_{ll} \rightarrow 0$, the propagator goes on-shell and these diagrams cause the cross section to diverge.

As is discussed in paper I and paper IV, an additional transverse momentum cut is needed on the charged leptons when NLO electroweak corrections are considered. The divergence in the example Feynman diagram shown in paper I which appears when both the gluon and the lepton go collinear to the incoming partons simultaneously, would be canceled for

⁸Experimentally, the decay into a tau pair is difficult to measure and hence most often omitted in the analyses.

example by a double-loop diagram such as

which enters at two-loop level for the mixed corrections, and hence is not included in the computation. One way of avoiding the problem, as is done in paper I, is to use a single lepton transverse momentum cut. However, the phase space considered in that case is limited and an extrapolation is needed.

In recent years, special attention has been given to two of the angular coefficients presented in Eq. (152) for the neutral-current Drell-Yan process,

$$A_0 = \sin^2 \theta_1 \quad \text{and} \quad A_2 = \sin^2 \theta_1 \cos 2\Phi_1 \quad (158)$$

which for $\Phi_1 = 0$ or $\theta_1 = 0$ are equal, $A_0 - A_2 = 0$. This relation is known as the Lam-Tung relation [58, 59]. The case when the quark is collinear to the hadron, that is, without any initial state radiation or transverse momentum of the incoming parton, the case $\theta_1 = 0$ holds. Thus, the Lam-Tung relation is a measure of the parton transverse momentum, or similarly, sensitive to higher-order QCD corrections. From the factor $\cos 2\Phi_1$, it is clear that $A_0 - A_2 \geq 0$ in general.

The first measurements on the angular coefficients were performed with pion beams at NA10 (CERN) [60] and E165 (Fermilab) [61] experiments. Both of these experiments measured a higher violation of the Lam-Tung relation than is predicted by the Standard Model, up to the accuracy which was available at the time. More recent measurements have been performed at $\sqrt{s} = 1.96$ TeV CDF collaboration (Tevatron) [62] in $p\bar{p}$ collisions; at the CMS detector for LHC collisions, at $\sqrt{8}$ TeV [57], measured differentially up to $p_{T,Z} = 300$ GeV in Z -boson transverse momentum; and at ATLAS [56], all showing a clear violation of the Lam-Tung relation. In Figure 11, the measured violation of the Lam-Tung relation measured by the ATLAS detector is shown. For larger $p_{T,Z}$ values, ATLAS data shows high discrepancy from the theory prediction at NNLO QCD (at zero- p_T of the weak boson: hence, this corresponds to a NLO QCD for the angular coefficients).

There are some featuring properties of the angular coefficients which will now be discussed. Firstly, for the case when the quark is collinear to the hadron, $\theta_1 = 0$, only the A_4 coefficient remains non-zero, as θ_0 becomes θ in Eq. (150), which is indeed a property verified by experimental measurements.

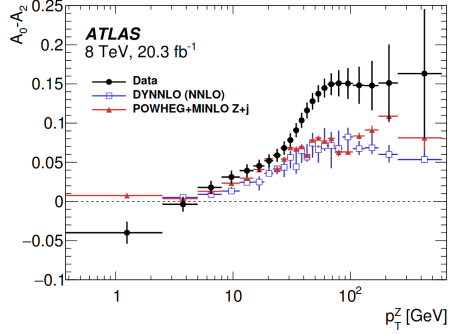


Figure 11: Differential distribution in $p_{T,Z}$ of the Lam-Tung relation $A_0 - A_2$ from ATLAS measurement and theory prediction at NNLO QCD, figure taken from Ref. [56].

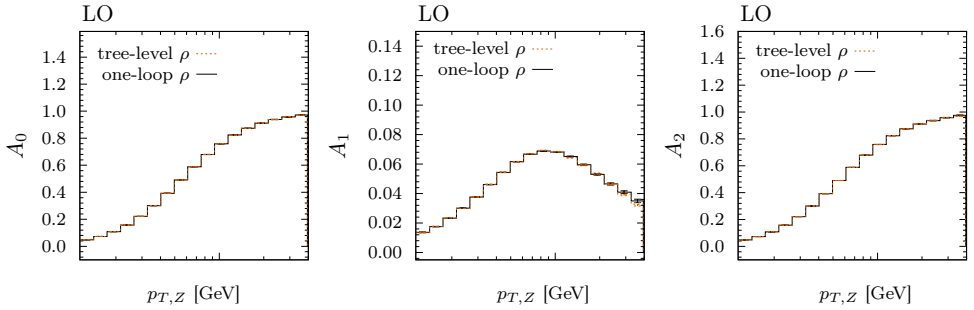


Figure 12: The angular coefficients A_0 (left), A_1 (middle) and A_2 (right) at LO with the ρ -parameter at tree-level (dashed) and including the top-induced one-loop corrections (solid).

Secondly, the decay coefficients transform differently under parity. By re-defining the angles θ, Φ to be those of the positively charged lepton instead,

$$\Phi \rightarrow \Phi + \pi, \quad \theta \rightarrow \pi - \theta, \quad (159)$$

one can see from Eq. (155) that the coefficients A_3, A_4, A_7 are odd under parity, while the other coefficients are even. The parity-odd coefficients are sensitive to the Z -boson coupling to leptons and the weak mixing angle (we see this also in their dependence on the coefficient a). In paper I this effect is mitigated by introducing higher order corrections to the weak mixing angle (in terms of the ρ -parameter). To complement the Figures I.2-I.4 of paper I, the LO distributions with and without the one-loop ρ -parameter is presented in Figure 12 (A_0, A_1, A_2) and Figure 13 (A_3 and A_4), in the same kinematic range and with the same calculation setup as the results presented in the paper. As can be seen in these figures, the parity-even coefficients remain unaffected by an inclusion of the top-induced

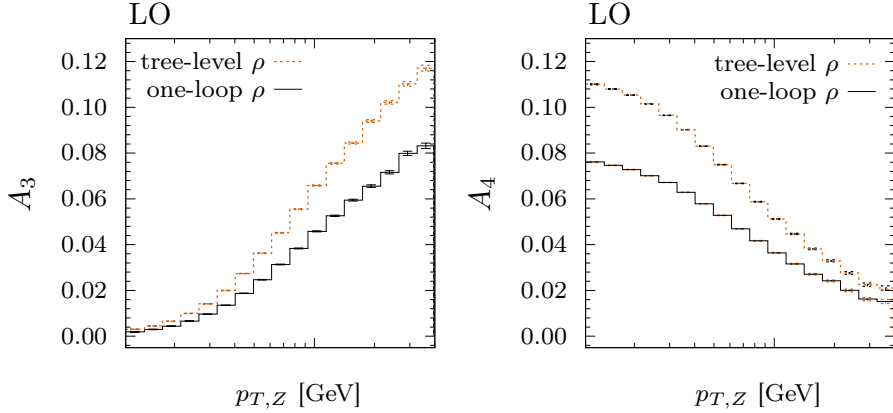


Figure 13: The angular coefficients A_3 (left) and A_4 (right) at LO with the ρ -parameter at tree-level (dashed) and including the top-induced one-loop corrections (solid).

one-loop correction to the ρ -parameter, while the parity-odd coefficients A_3 and A_4 show a significant dependence on the exact value on this electroweak parameter. The same feature is also present when including NLO QCD corrections.

The next point to mention is the dependence on Φ_1 : only the last three angular coefficients A_5, A_6, A_7 are odd under $\Phi_1 \rightarrow -\Phi_1$. There is, however, no prediction within the Standard Model which demands the quark and hadron planes to be oriented in a preferred azimuthal direction. Hence, it is expected that these coefficients, at least at LO, cancel for sufficiently large statistics. This phenomena is again observed at both CMS and ATLAS: all three coefficients are measured to be very small, see Figure 14 for the measurements by ATLAS.

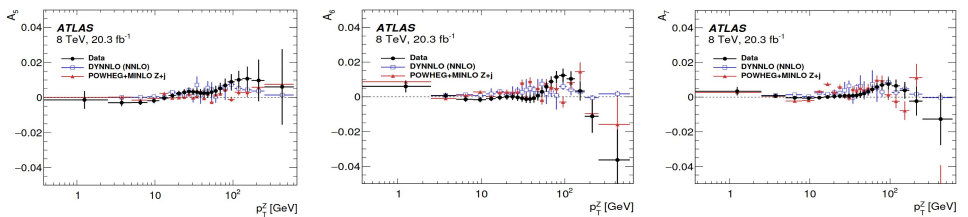


Figure 14: Differential distribution in $p_{T,Z}$ of the three vanishing coefficients A_5 (left) A_6 (middle) and A_7 (right) from ATLAS measurements, figures taken from Ref. [56].

Having introduced the coefficients and the Lam-Tung relation, we summarize the perturbative accuracy for each of these in Table 6, highlighting that observables may be of different fixed-order accuracy, depending on their intrinsic nature. In the following and in the pa-

pers, however, the notation for LO, NLO (and similarly NNLO) is the one presented in Eq. (148) which is valid at the total cross section level.

Table 6: The perturbative orders for the coefficients and the Lam-Tung relation at various orders of the coupling constants.

	$\mathcal{O}(\alpha^2)$	$\mathcal{O}(\alpha_s\alpha^2)$	$\mathcal{O}(\alpha_s^2\alpha^2)$
A_0, A_1, A_2, A_3	-	LO	NLO
A_4	LO	NLO	NNLO
A_5, A_6, A_7	-	-	LO
$A_0 - A_2$	-	-	LO

This concludes the introduction to the study of the angular coefficients of the neutral-current Drell-Yan process for finite- p_T production. In paper I the fixed-order NLO EW corrections to the angular coefficients is presented. This complements the existing NNLO QCD corrections to these decay coefficients [63].

The charged-current process: the W -boson and its mass

The production of a lepton pair with one charged lepton and one neutrino (measured as missing momentum in the detector) is the charged-current Drell-Yan process, related to the neutral one by a simple switch from the Z -boson as mediating particle to a W -boson, with a charge corresponding to the charge of the outgoing charged lepton. As can be seen from Figure 7, this process is roughly an order of magnitude more abundant than the neutral-current process, owing to the nature of the internal couplings and the lower mass of the W -boson.

Despite its abundance, a precise measurement of this process has been less successful than the neutral-current counterpart, due to the difficulty in measuring precisely the missing momentum of the neutrino. However, it is a key process in determining the mass of the W -boson, one of the free parameters of the Standard Model. The relation which connects the electroweak parameters to the W -boson mass at leading order is

$$m_W^2 \left(1 - \frac{m_W^2}{m_Z^2} \right) = \frac{\pi\alpha}{\sqrt{2}G_\mu}. \quad (160)$$

When radiative corrections are considered, the right-hand side of this relation is multiplied with $(1 + \Delta r)$, where Δr contains higher order effects to the muon decay.

W-boson charge Kinematic distribution	W^+		W^-		Combined	
	p_T^l	m_T	p_T^l	m_T	p_T^l	m_T
δm_W [MeV]						
Fixed-order PDF uncertainty	13.1	14.9	12.0	14.2	8.0	8.7
AZ tune	3.0	3.4	3.0	3.4	3.0	3.4
Charm-quark mass	1.2	1.5	1.2	1.5	1.2	1.5
Parton shower μ_F with heavy-flavour decorrelation	5.0	6.9	5.0	6.9	5.0	6.9
Parton shower PDF uncertainty	3.6	4.0	2.6	2.4	1.0	1.6
Angular coefficients	5.8	5.3	5.8	5.3	5.8	5.3
Total	15.9	18.1	14.8	17.2	11.6	12.9

Figure 15: The table presenting the uncertainties entering the W -boson mass measurements by ATLAS, taken from Ref. [64], with added red box markers for the largest source of uncertainty (PDF) and the error entering from the angular coefficients modeling.

The W -boson mass has been directly measured at the LHC by ATLAS [64] with data collected from the 7 TeV run, and LHCb [65] from data collected from the 13 TeV run. The obtained results are in agreement with the Standard Model. A recent measurement was published by the CDF II collaboration at Tevatron [66], presenting a 7σ -discrepancy from the previously made measurements of the mass. In general, pp collisions introduce larger uncertainties for the measurement of the charged-current Drell-Yan process than the corresponding $p\bar{p}$ collisions, such as those at Tevatron. The main reason for this is that the W^+ (W^-) process is dominantly produced by the $u\bar{d}$ ($\bar{d}u$) partonic interaction, which consists of purely valence quarks at a $p\bar{p}$ collider, but involves sea quarks at the LHC. Another source of uncertainty at the LHC are the heavy-flavour-initiated partonic processes (25% of all the processes), which are less dominant for the Z -boson process and the corresponding process at the Tevatron. These heavier quarks are modeled in PDFs with lower precision than the lighter u and d quarks. This introduces a large source of uncertainty for the precise measurement of the m_W parameter at the LHC [64].

In measuring m_W from the 7 TeV data by ATLAS, the strategy adopted in Ref. [64, 67] is a template fit to the charged lepton transverse momentum and the transverse mass of the lepton pair distributions: p_T^l, m_T . Distributions are fit to theory predictions and a minimal χ^2 -fit is performed for obtaining a best value for the m_W parameter. The mass is extracted from production of both W^+ and W^- and from both the electron and muon channels. The results in the analysis shows a slightly larger error in the W^+ samples entering through the PDF uncertainty. After the leading PDF uncertainties, the next source of uncertainties in the template fits are the angular coefficients, which parametrize the outgoing lepton angular distribution. The table from Ref. [64] is reproduced in Figure 15, indicating the largest source of uncertainty (PDF) and the theoretical uncertainties entering via the angular coefficients.

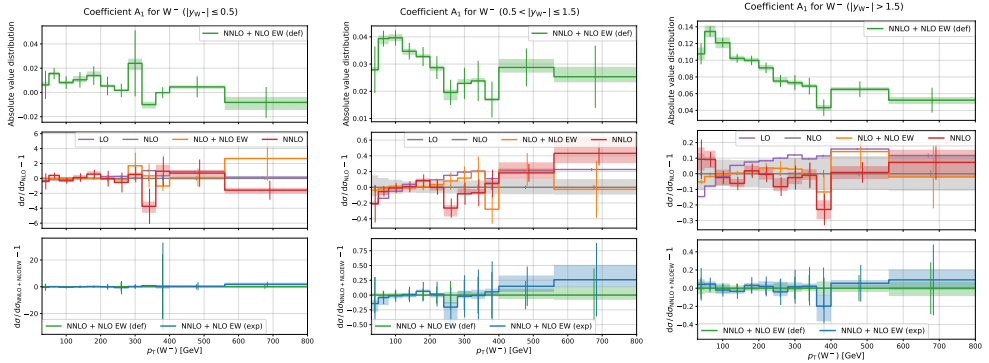


Figure 16: Rapidity dependence of the coefficient A_1 as a function of the W -boson transverse momentum. The results are shown for three rapidity bins of the W -boson: $|y| \leq 0.5$ (left), $0.5 < |y| \leq 1.5$ (middle), and $|y| > 1.5$ (right).

The angular coefficients for the charged-current Drell-Yan process, however, cannot be measured directly due to the missing momentum. The procedure adopted in Ref. [64] is to make an unfolding from the NLO QCD predictions for the Z -boson (for which the coefficients are very well measured) and the corresponding W -boson predictions for the coefficients. In this procedure, the assumption that the errors are similar for the two processes is made. This assumption, however, must be carefully investigated by considering higher order terms which are not present in the unfolding procedure, which would be those of NNLO QCD and NLO EW. Including these higher orders reduces significantly the assumptions included in the unfolding procedure between the Z - and the W -boson samples for the indirect measurement of the decay coefficients. This is the main motivation for the work in paper IV, in which we present combined NNLO QCD and NLO EW corrections to these angular coefficients. One issue with the fixed-order predictions at high precision is that they are not accessible in the low- p_T ranges of the weak boson due to large Sudakov factors of the form $\log\left(\frac{m_W}{p_{T,W}}\right)$, making the reasonable region accessible only for $p_{T,W} > 30$ GeV. The main region of interest for the template fits for the mass extraction is precisely this low- p_T range, where also the bulk of the reconstructed events lie.

Alternative direct measurements have been performed for these decay coefficients by the CDF collaboration [68]. To measure the azimuthal distribution directly, the W -boson mass is used here to constrain the kinematics and in that way extract the missing momentum. As this allows for a direct measurement of the coefficients, it is clear that such a measurement cannot be utilized also for the extraction of the W -boson mass.

In paper IV, the angular coefficients are presented differentially in the weak boson transverse momentum and rapidity, at a combined accuracy of NNLO QCD and NLO EW. As complement to the figures in the paper, in Figures 16-18 are shown the rapidity depend-

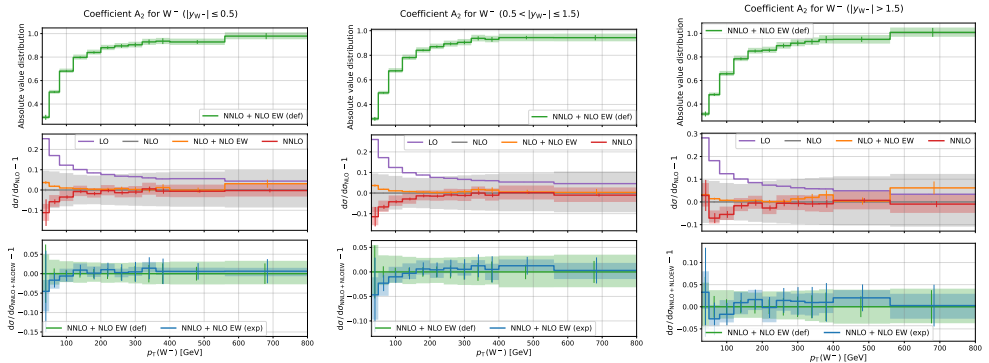


Figure 17: Rapidity dependence of the coefficient A_2 as a function of the W -boson transverse momentum. The results are shown for three rapidity bins of the W -boson: $|y| \leq 0.5$ (left), $0.5 < |y| \leq 1.5$ (middle), and $|y| > 1.5$ (right).

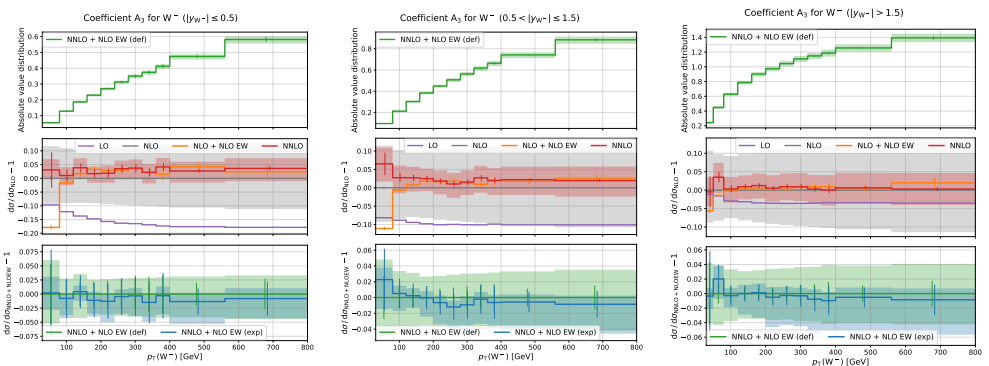


Figure 18: Rapidity dependence of the coefficient A_3 as a function of the W -boson transverse momentum. The results are shown for three rapidity bins of the W -boson: $|y| \leq 0.5$ (left), $0.5 < |y| \leq 1.5$ (middle), and $|y| > 1.5$ (right).

encies of the omitted coefficients (A_1 , A_2 , A_3 respectively) from paper IV. The detailed description of the figure setups is given in paper IV.

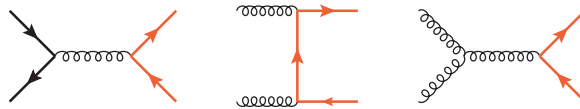
The single neutrino produced in this process escapes the detectors, but is reconstructable to a large degree in the transverse plane. The total momentum in the transverse plane approximates to zero, which neglects the transverse momentum of the incoming partons, a valid approximation in the high energy limits. The longitudinal momentum sum, however, is not measured, since the partons carry a fraction of the longitudinal momentum, which is undetermined from experiments. Hence, in the transverse plane only, the missing neutrino momentum can be reconstructed, by summing all the other detected final state particles (in theory only those emerging from the hard scattering). The neutrino reconstruction,

however, becomes more complicated when multiple neutrinos are in the final state, which is the case for a dileptonic decay of a top quark pair production. This is the next process we will present.

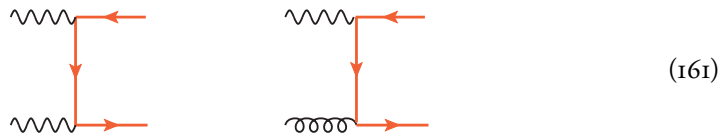
4.3 The most abundant heavy process: top-quark pair production

As the heaviest particle in the Standard Model, and with a fairly recent discovery (1995), the top quark entails many interesting investigations related to it. The pair production of top quarks, as can be seen in Figure 7, is the process with highest total cross-section after the Drell-Yan process at the LHC, as measured by ATLAS.

The Feynman diagrams at leading-order contributing to the pair production are the quark-anti-quark annihilation, and the s - and t -channel gluon fusions,



where the red fermion lines indicate on-shell top quark lines. At the LHC, the dominant production channel at LO is the gg fusion, while at $p\bar{p}$ colliders, such as the Tevatron, the dominant is the quark-anti-quark pair annihilation. There are, however, also photon induced channels if one considers also the electroweak couplings at leading-order, the $\gamma\gamma$ induced and the $g\gamma$ induced processes,



where again the red lines indicate top quarks.

This pair production process allows to investigate spin correlation effects between the final state particles. The reason is that the decay width of the top quark can be computed to be $\Gamma_t \sim m_t^3$, which implies that the top quark has a very large decay width and short lifetime. Therefore, it decays before hadronization and hence there have not been any bound top quark states observed. For this reason, in pair production, the spin correlation information is passed on to the decay products, as the time for decorrelation ($\sim 10^{-21}$ s) is longer than the lifetime of the quark ($\sim 10^{-23}$ s).

The LO and NLO expansion of this process in the α_s and α couplings is

$$\begin{aligned}\sigma_{\text{LO}}(\alpha_s, \alpha) &= \underbrace{\alpha_s^2 \sigma_{2,0}}_{\text{LO}_1} + \underbrace{\alpha_s \alpha \sigma_{1,1}}_{\text{LO}_2} + \underbrace{\alpha^2 \sigma_{0,2}}_{\text{LO}_3}, \\ \sigma_{\text{NLO}}(\alpha_s, \alpha) &= \underbrace{\alpha_s^3 \sigma_{3,0}}_{\text{NLO}_1} + \underbrace{\alpha_s^2 \alpha \sigma_{2,1}}_{\text{NLO}_2} + \underbrace{\alpha_s \alpha^2 \sigma_{1,2}}_{\text{NLO}_3} + \underbrace{\alpha^3 \sigma_{0,3}}_{\text{NLO}_4}.\end{aligned}\tag{162}$$

Table 7: List of partonic subprocesses contributing to LO terms for $t\bar{t}$ production.

Partonic subprocess	Contributes to order
$gg \rightarrow t\bar{t}$	LO ₁
$g\gamma \rightarrow t\bar{t}$	LO ₂
$\gamma\gamma \rightarrow t\bar{t}$	LO ₃
$q\bar{q} \rightarrow t\bar{t}$	LO ₁ +LO ₂ +LO ₃

In paper II, the leading LO contribution LO₁ is referred to as LO. The complete-LO refers to full LO expansion, LO₁+LO₂+LO₃. The NLO QCD refers to LO₁+NLO₁ and finally the complete-NLO refers to full-LO plus NLO₁+NLO₂+NLO₃+NLO₄ and finally NLO EW refers to LO₁+NLO₂. The various production channels which contribute to the LO terms is listed in Table 7. The $q\bar{q}$ -initiated process is the only process to include interference of mixed orders at leading order. In a 4-flavour scheme (massive b -quark), this interference is

$$\sim \text{Tr}[T^a] = 0 \tag{163}$$

between an s -channel gluon diagram and an s -channel photon diagram. Drawing the colour-flow lines of the interference diagram (middle diagram) and using the tracelessness of the fundamental generators, this interference contribution vanishes.

Including bottom quarks in the proton PDFs in a 5-flavour scheme, however, the interference between a t -channel diagram and s -channel diagram,

$$\sim \text{Tr}[T^a T^a] = (N_C^2 - 1) \tag{164}$$

contributes to the LO₂ term with a non-vanishing colour factor. We can repeat this for the NLO terms and the real emission processes which appear then in Table 8. One can similarly investigate which interferences vanish due to the colour structure in this case: most interferences have non-vanishing contributions.

Table 8: List of partonic subprocesses contributing to NLO terms for $t\bar{t}$ production.

Partonic subprocess	Contributes to order
$gg \rightarrow t\bar{t}g$	NLO ₁
$gg \rightarrow t\bar{t}\gamma$	NLO ₂
$g\gamma \rightarrow t\bar{t}g$	NLO ₂
$g\gamma \rightarrow t\bar{t}\gamma$	NLO ₃
$\gamma\gamma \rightarrow t\bar{t}g$	NLO ₃
$\gamma\gamma \rightarrow t\bar{t}\gamma$	NLO ₄
$q\bar{q} \rightarrow t\bar{t}g$	NLO ₁ +NLO ₂ +NLO ₃
$gq \rightarrow t\bar{t}q$	NLO ₁ +NLO ₂ +NLO ₃
$q\bar{q} \rightarrow t\bar{t}\gamma$	NLO ₂ +NLO ₃ +NLO ₄
$\gamma q \rightarrow t\bar{t}q$	NLO ₂ +NLO ₃ +NLO ₄

The total cross section for the process with the setup used in paper II, at the various perturbative orders is presented in Table 9. The orders in the table are not the orders which are examined in paper II, where we sum all NLO corrections to form a single complete-NLO correction. We see in the table that the EW effects are very small for the total cross section. Summing all the corrections besides the NLO₁, one finds that the EW effects are $\sim 0.5\%$. The reason for this small correction is the cancellation between the relatively large one percent NLO₂ correction (the leading NLO EW correction) and the subleading LO and subleading NLO contributions. Hence, in our complete-NLO calculations in paper II, where we include the top decays, a similar cancellation can be occurring at the integrated quantities (definitely) and differential distributions (possibly). Besides the total cross section, of interest to the work of this thesis are the spin correlation coefficients and the asymmetries. Both of these are introduced in turn, starting with a brief summary of the spin-density formalism.

Table 9: Total cross section of $pp \rightarrow t\bar{t}$ (without decay) at various orders and the ratio to the LO₁ value.

order	LO ₁	LO ₂	LO ₃	NLO ₁	NLO ₂	NLO ₃	NLO ₄
value [pb]	582.1(5)	2.316(8)	2.115(2)	211.0(2)	-7.226(2)	3.577(1)	0.0163(6)
ratio to LO ₁	1	+0.397 %	+0.363 %	+36.3 %	-1.24 %	+0.614 %	+0.003 %

Spin-density formalism

The spin-density formalism [69,70] relies on the density operator expression for observables in quantum mechanics. For this we introduce the density matrices for the outgoing $t\bar{t}$ final state to be $\rho_t(k_t, s_t)\rho_{\bar{t}}(k_{\bar{t}}, s_{\bar{t}})$, with momentum k and spin s for each of the quark and anti-quark. The matrix-element for the production of this final state is then

$$|\mathcal{M}|^2 \sim \text{Tr}[\rho_t(k_t, s_t)\rho_{\bar{t}}(k_{\bar{t}}, s_{\bar{t}})R], \quad (165)$$

where R is the spin-density matrix including the spin structure of the top quark and anti-quark. It can be expanded in the direct-product spin-space of the $t\bar{t}$ pair,

$$R = A(1 \otimes 1) + B_i^+(1 \otimes \sigma_i) + B_j^-(\sigma_j \otimes 1) + C_{ij}(\sigma_i \otimes \sigma_j), \quad (166)$$

where the i, j specify the three directions of the spin projection in some coordinate system. The σ_i are the usual Pauli spin matrices in a Cartesian system (x, y, z) . The coordinate system used in paper II is a Cartesian coordinate in the rest frame of the top-quark-pair, with axes $(\hat{k}, \hat{n}, \hat{r})$: the exact definition is given in the paper.

The spin correlation coefficients of interest are the 6 B_i^\pm -coefficients and the 9 C_{ij} coefficients. These are obtained by an expansion into the lepton angles θ_\pm^i with the three axes $i = k, n, r$ for the l^+ and l^- respectively. As such, the B_i^\pm coefficients correspond to an asymmetry in the $\cos \theta_\pm^i$ distributions, and the C_{ij} coefficients to asymmetries in the $\cos \theta_\pm^i \cos \theta_\pm^j$ distributions and the coefficients are computed as weighted averages of these trigonometric functions, normalized to the total cross section.

Top charge asymmetry

In pair production at hadron colliders, the top quark and top anti-quark have been observed to have preferred directions along the beam axis. This phenomena also arises in other type of processes, with different final states, and is termed asymmetry. At the Tevatron ($p\bar{p}$ collisions) where the dominant production channel is the $q\bar{q}$ initial state, Standard

Model predicts an asymmetric distribution of the top and anti-top along the beam axis: this is called the forward-backward asymmetry. The interest for examining the top quark forward-backward asymmetry arose when a $\sim 2\sigma$ discrepancy between theory⁹ and experiment had been measured at both of the Tevatron experiments, D0 and CDF. This stimulated interest and the process was investigated in more detail also at LHC. At a pp collider such as the LHC, the LO prediction is a symmetric production of the top and anti-top pair at leading order: this is due to the dominant gg initiated process and at LO there is no additional symmetry-breaking diagram. Thus, one speaks rather of charge asymmetry (or central-peripheral asymmetry) at LHC, which slightly deviates from zero due to higher-order contributions. The forward-backward asymmetry and the charge asymmetry is defined by

$$A_C^{t\bar{t}} = \frac{\sigma(\Delta y > 0) - \sigma(\Delta y < 0)}{\sigma(\Delta y > 0) + \sigma(\Delta y < 0)}, \quad (167)$$

with the Δy defined as the distance in rapidity-space between the top quark and the top anti-quark.

Including decays

A single top quark decays to Wb (branching ratio $\sim 100\%$), where the produced W -boson further decays either to a quark pair or to a lepton pair. The total branching ratio in different decay channels of the top quark pair is summarized in Table 10, where lepton universality (including decays to e, μ, τ) has been assumed in the branching ratio values.

Table 10: A summary of decay channels and branching ratios (BR) for a top quark pair [2].

	Final state	BR
all-hadronic	$q\bar{q}'q''\bar{q}'''b\bar{b}$	45.7 %
semi-leptonic	$l\nu_l q\bar{q}'b\bar{b}$	43.8 %
dilepton	$l\nu_l l'\nu_{l'}b\bar{b}$	10.5%

The total cross section when including top quark decays to a specific final state is expected to decrease with the corresponding branching ratio. As the branching ratio of the top quark to the electron (or muon) channel is $\sim 11\%$, the combined reduction of cross section for the dilepton channel for top quark pair production is $\sim 1.2\%$. The total cross section predictions for the dilepton channel are summarized in Table 11 at each fixed order up to NLO as given in Eq. (162), in the same setup as used in paper II.

Table II: Total cross section of $pp \rightarrow t\bar{t} \rightarrow e^+v_e\mu^-\bar{\nu}_\mu b\bar{b}$ in the NWA at various orders included in the production.

order	LO ₁	complete-LO	NLO QCD	complete-NLO
σ [pb]	6.859(2)	6.909(2)	9.340(3)	9.349(3)
ratio to LO ₁	-	+0.7 %	+36.2 %	+36.3 %

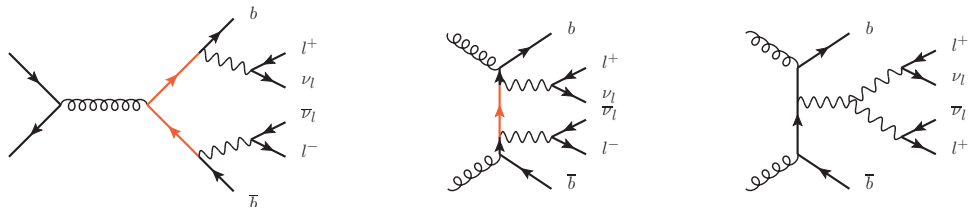


Figure 19: Examples of double-resonant diagrams (left), single-resonant diagrams (middle) and non-resonant diagrams (right). The red lines indicate on-shell top quark fermion lines.

The dilepton final state $pp \rightarrow t\bar{t} \rightarrow e^+v_e\mu^-\bar{\nu}_\mu b\bar{b}$ has contributions from double-resonant diagrams, single-resonant diagrams and non-resonant diagrams, of which examples are given in Figure 19. In the NWA, the top quarks are assumed to be on-shell in the production, and hence only the double-resonant diagrams contribute. In this approximation, the total cross section is schematically decomposed into

$$\sigma_{\text{tot}} = \sigma_{t\bar{t}} \times \Gamma_t \times \Gamma_{\bar{t}}, \quad (168)$$

with the decays of the top and anti-top respectively denoted with $\Gamma_{t/\bar{t}}$ and the production cross section of the on-shell top quark pair denoted by $\sigma_{t\bar{t}}$. The program `MadSpin` computes the production part with all real emission diagrams and loop diagrams included. The decay part is generated based on LO matrix-elements, without real emissions. Similarly, loop corrections which connect the production and decay part are not included in the decay chain model. Examples of diagrams which are included (left) and which are not included (right) in the computations of paper II, are shown in Figure 20.

The program `MadSpin` is currently unable to separate the spin correlations into each of the separate NLO and LO terms. To portray this, we consider the example of the $qg \rightarrow qt\bar{t}$ channel, for which one of the interferences is shown in Figure 21, with the indicated QCD and QED couplings at the matrix-element level. The interference is of order $\alpha_s^2\alpha$. In

⁹The current best theory prediction for the asymmetry is NNLO QCD accurate [71].

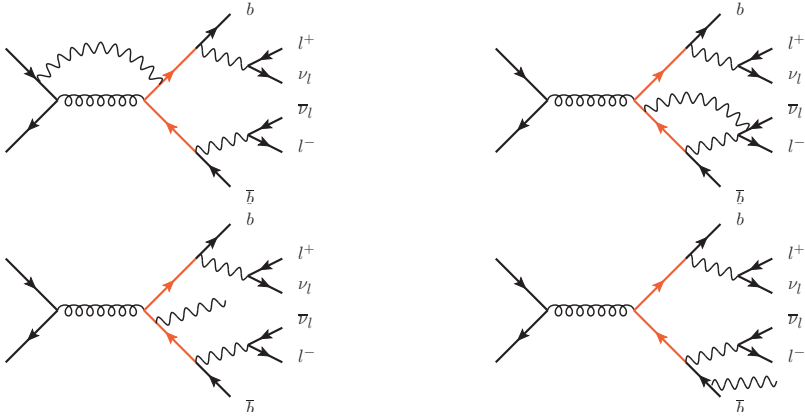


Figure 20: Examples of loop diagrams (upper) in the NLO EW corrections which enter only in the production part (left) and which enter as interference between the production and decay part (right). Example of real emission diagrams (lower) which are explicitly included in the computation (left) with the emission from the production part and example of real emission from the decay part (right) not included in the computation.

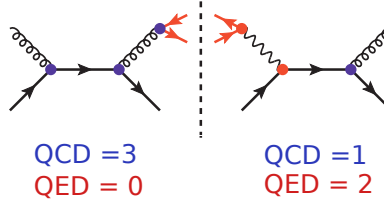


Figure 21: An example of an interference for $gq \rightarrow qt\bar{t}$ at $\mathcal{O}(\alpha_s^2\alpha)$ depicting the QCD (blue) and QED (red) couplings.

the current version of MadSpin, however, the QCD and QED couplings are specified on matrix-element level, and hence a generation¹⁰

pp > t t~ QCD=2 QED=1 [QCD QED]

does not run. The reason for this is that neither of these diagrams can be generated with the syntax within MadSpin and an increase in the generation syntax QCD=2 or QED=1 would yield a correct generation of these interferences, but would include also higher orders in the spin correlations.

¹⁰The syntax for the order specification was changed during the writing of this thesis: here the syntax which was used in the version and branch used for the calculations in paper II is presented.

We present some distributions for the top quarks which were performed in the analysis of paper II but are not included in the paper. In Figure 22 the top quark transverse momentum and rapidity and the invariant mass of the top quark pair at LO, NLO QCD and complete-NLO are presented. This can be compared to the results presented in Ref. [21], where the transverse momentum distribution is presented contribution-by-contribution in the NLO corrections. Although a straight-forward comparison is not feasible due to the different binning and calculation setup, we can see that our results reflect these distributions qualitatively. Further, we note that the complete-NLO corrections are negligible throughout most of the region, with a couple of percent effect. In the tails of the distributions, the statistics is indeed low, but from the smoothness of the K -factors, we note that the electroweak corrections can be deduced to be quite small in also these regions.

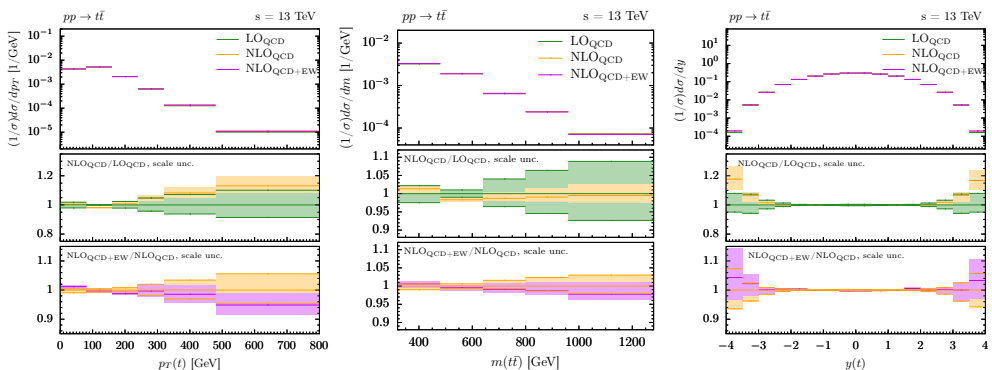


Figure 22: Top quark distributions in the $pp \rightarrow t\bar{t}$ process, the transverse momentum of the top quark (left), the invariant mass of the top pair (middle) and the top rapidity (right).

As presented in paper II, the complete-NLO corrections to the B spin correlation coefficients are sizeable and with these corrections the coefficients become non-zero, in comparison to the values obtained with NLO QCD when the coefficients vanish. To investigate this, one can examine the shape of the corresponding differential distributions at complete-NLO precision. This is shown in Figure 23 (for the B^+ coefficients in the three different axes directions $\hat{k}, \hat{n}, \hat{r}$) and in Figure 24 (similarly for the B^- coefficients). As can be seen from the figures, the shape of the coefficients are not altered by a significant amount by the complete-NLO corrections. Only in B_r^\pm can one observe some effect which creates a slight asymmetry in the distribution. The remaining C coefficients do not obtain any non-negligible contribution from the complete-NLO corrections: hence, these distributions are not presented here, and the corresponding coefficients are presented in paper II.

This concludes the introduction to the top quark pair production which is needed for an understanding of the results of complete-NLO corrections to the spin correlation coefficients and asymmetries presented in paper II.

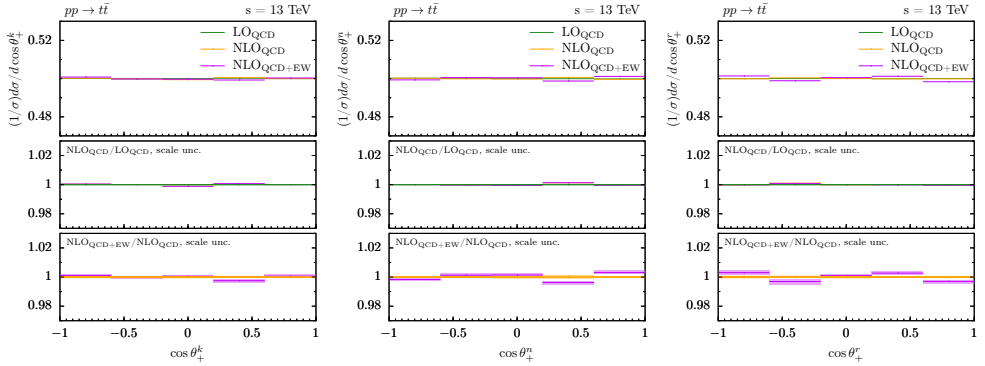


Figure 23: Angular distributions corresponding to B^+ coefficients along the three axes \hat{k} (left), \hat{n} (middle) and \hat{r} (right).

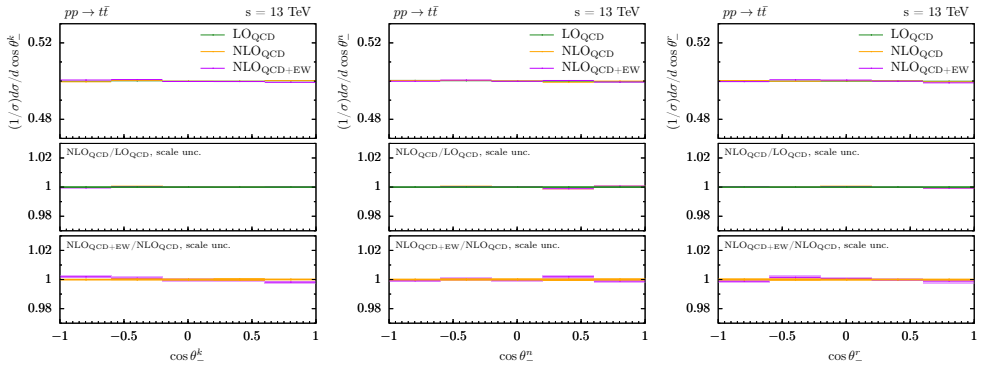


Figure 24: Angular distributions corresponding to B^- coefficients along the three axes \hat{k} (left), \hat{n} (middle) and \hat{r} (right).

4.4 What washes over the detectors: multi-jet processes

Due to the enhanced emission rates for soft and collinear particles, the partonic process at a hadron collider is dressed with $\mathcal{O}(100)$ final state partons when evolving to the lower scales. Most of these particles, however, have very low transverse momenta, low invariant masses and small angular separation from other observable objects. A jet clustering algorithm is typically used to obtain jets of collimated particles, rather than individual very soft or collinear particles, in order to obtain IR-safe results. The jet clustering algorithms must

be infrared-safe in order for obtaining reasonable predictions. Two main types of such clustering algorithms exist today: the cone algorithms and the k_T -algorithm family.

The cone algorithms constitute the simplest clustering of the detected hadronic signals. In the clustering, a main particle is picked, and all surrounding particles within a radius of R_{cone} in the (η, ϕ) -plane are clustered, adding the 4-momentum accordingly. The basic formulation of this algorithm, however, suffers from IR unsafety. Improvements can be made in order to remedy this, but often results in that the intuitive picture for the algorithm is lost.

The k_T -family utilizes an iterative procedure, in which each pair of particles (i, j) in the sample is considered in turn and the following quantities are computed:

$$d_{b,i} = p_{T,i}^{2n} \quad (169)$$

$$d_{i,j} = \frac{R_{ij}}{R_0} \min((p_{T,i})^{2n}, (p_{T,j})^{2n}), \quad (170)$$

where the distance $R_{i,j}$ is computed according to Eq. (146) in the (η, ϕ) -plane, and n, R_0 are parameters. The smallest computed distance measure is picked, and the two particles are clustered either with each other (if $d_{i,j}$ is the smallest measure) or with the beam (if $d_{b,i}$ is the smallest measure). Three main algorithms are included in this family: the k_T -algorithm, for which $n = 1$ and thus constitutes a clustering based on the transverse momentum. The Cambridge-Aachen algorithm uses $n = 0$, so it is a clustering based only on the radial separation. Finally, the most commonly used algorithm today is the anti- k_T algorithm, which uses $n = -1$ as parameter.

With a well-defined object of jets, experiments can measure processes with many jets in the final state, within some fiducial cuts of the detectors and demanding certain minimum transverse momenta for the jets. The inclusive jet production, as can be seen from Figure 7, is the process that is most abundant at the LHC. By demanding well-separated and hard jets however, the cross section decreases for increasing number of final jets.

Multi-jet events are the most dominating backgrounds in many rare process or new physics searches. Due to the large phase space and the large colour space that is spanned by multi-jet events, precise theoretical computations are very limited for a large number of external particles. The current status is computing up to 10 jets at LO [72]. However, the method with which these are computed is a Monte Carlo sampling in the colour space, introducing very large point-by-point fluctuations when doing the phase-space integration. Computations treating the colour algebra in an exact manner can handle roughly up to 6 final state QCD particles. Experiments, on the other hand, are able to measure up to 8-9 final state jets [73]. So the gap between precise theory possibilities for precise predictions and the experimental measurements of multi-jet final states is as of today a challenging issue, but one which must be overcome for efficiently accounting for Standard Model background.

A solution to this problem, presented in paper III, is to perform an exact colour summation of the matrix-element, based on the colour expansion in powers of $\frac{1}{N_C}$. The simplification suggested is to truncate the colour sum at NLC accuracy. The results shown in paper III indicate that this indeed results in a colour matrix with much fewer terms than a full colour summation, reducing a factorial square growth of the colour sum to a polynomial growth. The paper presents the rules on how to obtain exactly the locations of the NLC terms in the colour matrix, allowing for determination of the colour sum of NLC precision prior to computing all the colour factors. The theory foundation in the paper opens up the possibility for an NLC-precise matrix-element generator, that can handle up to 8-9 final state QCD partons.

5 Outlook

“The past is not yours, only its trailing shadow. The future is not yours, only its beam which falls before you. The hour is yours. Only the hour in which you live. Do not hurry out of it.”

— translation from Gárdonyi Géza

After its unexpected postponed start of the LHC, the data collected in a lower energy range than first intended, has led to a large Standard Model community development and a precision frontier which has expanded largely in the past $\mathcal{O}(10)$ years. The work in this thesis is a contribution to this effort of pushing the precision frontier for some of the important processes at the LHC, with a main focus on the hard scattering with NLO EW corrections, their combination with NNLO QCD predictions and the colour expansion of matrix-elements. The ultimate goal of this joint precision effort is to have a handle on the Standard Model background from the theory side at the finest possible level. Only then can, if any, the discrepancy with very small effect be extracted from data and any potential new physics hiding in the shadows of uncertainty bands be detected.

The future of particle physics and of precision phenomenology as it is performed today has perhaps a natural upper limit. Although the technical aspect is also an evolving field of research, the need for computational power for higher order computations within perturbation theory tends towards being overwhelming. At some undetermined point in the future, particle physics will face the need to develop a new approach beyond perturbation theory at high energies, and, perhaps, even beyond quantum field theory. However, until we reach that upper limit, a multitude of development is still in place within our current framework.

An equally important complement to the theory developments on the phenomenology horizon is the upgrade of experimental techniques: precision in theory has no significance if it is not matched by precision in experiment. For precision in data taking, precise detector equipment is needed, and a sufficient amount of statistics. The latter aspect is hopefully to be improved by the high-luminosity era of LHC, with a luminosity 10 times larger than the current LHC setup, with a planned operational start in 2029.

This friendly trigger of precise data taking and predictions between the experimental and theory community is what drives particle physics forward. It is thus needless to say that the field of phenomenology, the language of the dialogues between these two aspects of particle physics, is unavoidable and crucial for any future development. Encouraging fruitful collaborations across these two fields, exchanging knowledge and creating an open atmosphere is vital for this field of research. Only together can we walk the bridge of phenomenology towards the unknown lands of particles.

References

- [1] L. D. Faddeev and V. N. Popov, “Feynman Diagrams for the Yang-Mills Field,” *Phys. Lett. B* **25** (1967) 29–30.
- [2] **Particle Data Group** Collaboration, P. A. Zyla *et al.*, “Review of Particle Physics,” *PTEP* **2020** no. 8, (2020) 083C01.
- [3] A. Denner and S. Dittmaier, “Electroweak Radiative Corrections for Collider Physics,” *Phys. Rept.* **864** (2020) 1–163, [arXiv:1912.06823 \[hep-ph\]](#).
- [4] D. Pagani, H.-S. Shao, I. Tsirikos, and M. Zaro, “Automated EW corrections with isolated photons: $t\bar{t}\gamma$, $t\bar{t}\gamma\gamma$ and $t\gamma j$ as case studies,” *JHEP* **09** (2021) 155, [arXiv:2106.02059 \[hep-ph\]](#).
- [5] D. A. Ross and M. J. G. Veltman, “Neutral Currents in Neutrino Experiments,” *Nucl. Phys. B* **95** (1975) 135–147.
- [6] Q. Yu, H. Zhou, J. Yan, X.-D. Huang, and X.-G. Wu, “A new analysis of the pQCD contributions to the electroweak parameter ρ using the single-scale approach of principle of maximum conformality,” *Phys. Lett. B* **820** (2021) 136574, [arXiv:2105.07230 \[hep-ph\]](#).
- [7] M. Chiesa, F. Piccinini, and A. Vicini, “Direct determination of $\sin^2 \theta_{eff}^l$ at hadron colliders,” *Phys. Rev. D* **100** no. 7, (2019) 071302, [arXiv:1906.11569 \[hep-ph\]](#).
- [8] **CMS** Collaboration, A. Bodek, “Measurement of the effective weak mixing angle $\sin^2 \theta_{eff}^{lept}$ from the forward-backward asymmetry of Drell-Yan events at CMS,” in *13th Conference on the Intersections of Particle and Nuclear Physics*. 8, 2018. [arXiv:1808.03170 \[hep-ex\]](#).
- [9] **ATLAS** Collaboration, “Measurement of the effective leptonic weak mixing angle using electron and muon pairs from Z -boson decay in the ATLAS experiment at $\sqrt{s} = 8$ TeV,” *ATLAS-CONF-2018-037* (2018) .
- [10] A. Denner and S. Dittmaier, “The Complex-mass scheme for perturbative calculations with unstable particles,” *Nucl. Phys. B Proc. Suppl.* **160** (2006) 22–26, [arXiv:hep-ph/0605312](#).
- [11] T. Kinoshita, “Mass singularities of Feynman amplitudes,” *J. Math. Phys.* **3** (1962) 650–677.
- [12] T. D. Lee and M. Nauenberg, “Degenerate Systems and Mass Singularities,” *Phys. Rev.* **133** (1964) B1549–B1562.

- [13] G. Altarelli and G. Parisi, “Asymptotic Freedom in Parton Language,” *Nucl. Phys. B* **126** (1977) 298–318.
- [14] Y. L. Dokshitzer, “Calculation of the Structure Functions for Deep Inelastic Scattering and e^+e^- Annihilation by Perturbation Theory in Quantum Chromodynamics,” *Sov. Phys. JETP* **46** (1977) 641–653.
- [15] V. N. Gribov and L. N. Lipatov, “Deep inelastic $e p$ scattering in perturbation theory,” *Sov. J. Nucl. Phys.* **15** (1972) 438–450.
- [16] V. Del Duca, L. J. Dixon, and F. Maltoni, “New color decompositions for gauge amplitudes at tree and loop level,” *Nucl. Phys. B* **571** (2000) 51–70, [arXiv:hep-ph/9910563](#).
- [17] G. P. Lepage, “Adaptive multidimensional integration: VEGAS enhanced,” *J. Comput. Phys.* **439** (2021) 110386, [arXiv:2009.05112](#) [[physics.comp-ph](#)].
- [18] P. Nason, “MINT: A Computer program for adaptive Monte Carlo integration and generation of unweighted distributions,” [arXiv:0709.2085](#) [[hep-ph](#)].
- [19] R. Frederix, S. Frixione, V. Hirschi, D. Pagani, H. S. Shao, and M. Zaro, “The automation of next-to-leading order electroweak calculations,” *JHEP* **07** (2018) 185, [arXiv:1804.10017](#) [[hep-ph](#)]. [Erratum: *JHEP* **11**, 085 (2021)].
- [20] J. M. Campbell and R. K. Ellis, “ $t\bar{t}W^{+-}$ production and decay at NLO,” *JHEP* **07** (2012) 052, [arXiv:1204.5678](#) [[hep-ph](#)].
- [21] M. Czakon, D. Heymes, A. Mitov, D. Pagani, I. Tsinikos, and M. Zaro, “Top-pair production at the LHC through NNLO QCD and NLO EW,” *JHEP* **10** (2017) 186, [arXiv:1705.04105](#) [[hep-ph](#)].
- [22] V. V. Sudakov, “Vertex parts at very high-energies in quantum electrodynamics,” *Sov. Phys. JETP* **3** (1956) 65–71.
- [23] A. Denner and S. Pozzorini, “One loop leading logarithms in electroweak radiative corrections. I. Results,” *Eur. Phys. J. C* **18** (2001) 461–480, [arXiv:hep-ph/0010201](#).
- [24] A. Denner and S. Pozzorini, “Leading electroweak logarithms at one loop,” in *5th International Symposium on Radiative Corrections: Applications of Quantum Field Theory to Phenomenology*, **1**, 2001. [arXiv:hep-ph/0101213](#).
- [25] T. Sjöstrand, S. Ask, J. R. Christiansen, R. Corke, N. Desai, P. Ilten, S. Mrenna, S. Prestel, C. O. Rasmussen, and P. Z. Skands, “An introduction to PYTHIA 8.2,” *Comput. Phys. Commun.* **191** (2015) 159–177, [arXiv:1410.3012](#) [[hep-ph](#)].

- [26] J. Bellm *et al.*, “Herwig 7.0/Herwig++ 3.0 release note,” *Eur. Phys. J. C* **76** no. 4, (2016) 196, arXiv:1512.01178 [hep-ph].
- [27] **Sherpa** Collaboration, E. Bothmann *et al.*, “Event Generation with Sherpa 2.2,” *SciPost Phys.* **7** no. 3, (2019) 034, arXiv:1905.09127 [hep-ph].
- [28] A. Buckley, J. Ferrando, S. Lloyd, K. Nordström, B. Page, M. Rüfenacht, M. Schönherr, and G. Watt, “LHAPDF6: parton density access in the LHC precision era,” *Eur. Phys. J. C* **75** (2015) 132, arXiv:1412.7420 [hep-ph].
- [29] S. Forte, L. Garrido, J. I. Latorre, and A. Piccione, “Neural network parametrization of deep inelastic structure functions,” *JHEP* **05** (2002) 062, arXiv:hep-ph/0204232.
- [30] A. Manohar, P. Nason, G. P. Salam, and G. Zanderighi, “How bright is the proton? A precise determination of the photon parton distribution function,” *Phys. Rev. Lett.* **117** no. 24, (2016) 242002, arXiv:1607.04266 [hep-ph].
- [31] **NNPDF** Collaboration, V. Bertone, S. Carrazza, N. P. Hartland, and J. Rojo, “Illuminating the photon content of the proton within a global PDF analysis,” *SciPost Phys.* **5** no. 1, (2018) 008, arXiv:1712.07053 [hep-ph].
- [32] J. Alwall, R. Frederix, S. Frixione, V. Hirschi, F. Maltoni, O. Mattelaer, H. S. Shao, T. Stelzer, P. Torrielli, and M. Zaro, “The automated computation of tree-level and next-to-leading order differential cross sections, and their matching to parton shower simulations,” *JHEP* **07** (2014) 079, arXiv:1405.0301 [hep-ph].
- [33] A. Alloul, N. D. Christensen, C. Degrande, C. Duhr, and B. Fuks, “FeynRules 2.0 - A complete toolbox for tree-level phenomenology,” *Comput. Phys. Commun.* **185** (2014) 2250–2300, arXiv:1310.1921 [hep-ph].
- [34] C. Degrande, C. Duhr, B. Fuks, D. Grellscheid, O. Mattelaer, and T. Reiter, “UFO - The Universal FeynRules Output,” *Comput. Phys. Commun.* **183** (2012) 1201–1214, arXiv:1108.2040 [hep-ph].
- [35] P. de Aquino, W. Link, F. Maltoni, O. Mattelaer, and T. Stelzer, “ALOHA: Automatic Libraries Of Helicity Amplitudes for Feynman Diagram Computations,” *Comput. Phys. Commun.* **183** (2012) 2254–2263, arXiv:1108.2041 [hep-ph].
- [36] H. Murayama, I. Watanabe, and K. Hagiwara, “HELAS: HELicity amplitude subroutines for Feynman diagram evaluations,” *KEK-91-II* (1992) .
- [37] J. Alwall *et al.*, “A Standard format for Les Houches event files,” *Comput. Phys. Commun.* **176** (2007) 300–304, arXiv:hep-ph/0609017.

- [38] E. Boos *et al.*, “Generic User Process Interface for Event Generators,” in *2nd Les Houches Workshop on Physics at TeV Colliders*. 9, 2001. [arXiv:hep-ph/0109068](#).
- [39] R. Frederix, S. Frixione, F. Maltoni, and T. Stelzer, “Automation of next-to-leading order computations in QCD: The FKS subtraction,” *JHEP* **10** (2009) 003, [arXiv:0908.4272 \[hep-ph\]](#).
- [40] V. Hirschi and O. Mattelaer, “Automated event generation for loop-induced processes,” *JHEP* **10** (2015) 146, [arXiv:1507.00020 \[hep-ph\]](#).
- [41] G. Ossola, C. G. Papadopoulos, and R. Pittau, “CutTools: A Program implementing the OPP reduction method to compute one-loop amplitudes,” *JHEP* **03** (2008) 042, [arXiv:0711.3596 \[hep-ph\]](#).
- [42] G. Ossola, C. G. Papadopoulos, and R. Pittau, “Reducing full one-loop amplitudes to scalar integrals at the integrand level,” *Nucl. Phys. B* **763** (2007) 147–169, [arXiv:hep-ph/0609007](#).
- [43] P. Mastrolia, E. Mirabella, and T. Peraro, “Integrand reduction of one-loop scattering amplitudes through Laurent series expansion,” *JHEP* **06** (2012) 095, [arXiv:1203.0291 \[hep-ph\]](#). [Erratum: *JHEP* **11**, 128 (2012)].
- [44] T. Peraro, “Ninja: Automated Integrand Reduction via Laurent Expansion for One-Loop Amplitudes,” *Comput. Phys. Commun.* **185** (2014) 2771–2797, [arXiv:1403.1229 \[hep-ph\]](#).
- [45] V. Hirschi and T. Peraro, “Tensor integrand reduction via Laurent expansion,” *JHEP* **06** (2016) 060, [arXiv:1604.01363 \[hep-ph\]](#).
- [46] F. Cascioli, P. Maierhöfer, and S. Pozzorini, “Scattering amplitudes at next-to-leading order with Open Loops,” *PoS LL2012* (2012) 055.
- [47] S. Frixione, Z. Kunszt, and A. Signer, “Three jet cross-sections to next-to-leading order,” *Nucl. Phys. B* **467** (1996) 399–442, [arXiv:hep-ph/9512328](#).
- [48] S. Frixione and B. R. Webber, “Matching NLO QCD computations and parton shower simulations,” *JHEP* **06** (2002) 029, [arXiv:hep-ph/0204244](#).
- [49] P. Nason, “A New method for combining NLO QCD with shower Monte Carlo algorithms,” *JHEP* **11** (2004) 040, [arXiv:hep-ph/0409146](#).
- [50] P. Artoisenet, R. Frederix, O. Mattelaer, and R. Rietkerk, “Automatic spin-entangled decays of heavy resonances in Monte Carlo simulations,” *JHEP* **03** (2013) 015, [arXiv:1212.3460 \[hep-ph\]](#).

- [51] S. Frixione, E. Laenen, P. Motylinski, and B. R. Webber, “Angular correlations of lepton pairs from vector boson and top quark decays in Monte Carlo simulations,” *JHEP* **04** (2007) 081, arXiv:hep-ph/0702198.
- [52] O. Mattelaer, “On the maximal use of Monte Carlo samples: re-weighting events at NLO accuracy,” *Eur. Phys. J. C* **76** no. 12, (2016) 674, arXiv:1607.00763 [hep-ph].
- [53] UA1 Collaboration, G. Arnison *et al.*, “Experimental Observation of Lepton Pairs of Invariant Mass Around 95-GeV/c² at the CERN SPS Collider,” *Phys. Lett. B* **126** (1983) 398–410.
- [54] UA2 Collaboration, M. Banner *et al.*, “Observation of Single Isolated Electrons of High Transverse Momentum in Events with Missing Transverse Energy at the CERN anti-p p Collider,” *Phys. Lett. B* **122** (1983) 476–485.
- [55] J.-C. Peng, D. Boer, W.-C. Chang, R. E. McClellan, and O. Teryaev, “On the rotational invariance and non-invariance of lepton angular distributions in Drell–Yan and quarkonium production,” *Phys. Lett. B* **789** (2019) 356–359, arXiv:1808.04398 [hep-ph].
- [56] ATLAS Collaboration, G. Aad *et al.*, “Measurement of the angular coefficients in Z-boson events using electron and muon pairs from data taken at $\sqrt{s} = 8$ TeV with the ATLAS detector,” *JHEP* **08** (2016) 159, arXiv:1606.00689 [hep-ex].
- [57] CMS Collaboration, I. Gorbunov, V. Shalaev, and S. Smatov, “Measurement of the Drell–Yan Angular Coefficients with the CMS Experiment at LHC,” *J. Phys. Conf. Ser.* **1337** no. 1, (2019) 012009.
- [58] C. S. Lam and W.-K. Tung, “A Systematic Approach to Inclusive Lepton Pair Production in Hadronic Collisions,” *Phys. Rev. D* **18** (1978) 2447.
- [59] C. S. Lam and W.-K. Tung, “A Parton Model Relation Sans QCD Modifications in Lepton Pair Productions,” *Phys. Rev. D* **21** (1980) 2712.
- [60] NA10 Collaboration, M. Guanziroli *et al.*, “Angular Distributions of Muon Pairs Produced by Negative Pions on Deuterium and Tungsten,” *Z. Phys. C* **37** (1988) 545.
- [61] J. S. Conway *et al.*, “Experimental Study of Muon Pairs Produced by 252-GeV Pions on Tungsten,” *Phys. Rev. D* **39** (1989) 92–122.
- [62] CDF Collaboration, T. Aaltonen *et al.*, “First Measurement of the Angular Coefficients of Drell-Yan e^+e^- pairs in the Z Mass Region from $p\bar{p}$ Collisions at $\sqrt{s} = 1.96$ TeV,” *Phys. Rev. Lett.* **106** (2011) 241801, arXiv:1103.5699 [hep-ex].

- [63] R. Gauld, A. Gehrmann-De Ridder, T. Gehrmann, E. W. N. Glover, and A. Huss, “Precise predictions for the angular coefficients in Z-boson production at the LHC,” *JHEP* **11** (2017) 003, arXiv:1708.00008 [hep-ph].
- [64] ATLAS Collaboration, M. Aaboud *et al.*, “Measurement of the W-boson mass in pp collisions at $\sqrt{s} = 7$ TeV with the ATLAS detector,” *Eur. Phys. J. C* **78** no. 2, (2018) 110, arXiv:1701.07240 [hep-ex]. [Erratum: *Eur.Phys.J.C* **78**, 898 (2018)].
- [65] LHCb Collaboration, R. Aaij *et al.*, “Measurement of the W boson mass,” *JHEP* **01** (2022) 036, arXiv:2109.01113 [hep-ex].
- [66] CDF Collaboration, T. Aaltonen *et al.*, “High-precision measurement of the W boson mass with the CDF II detector,” *Science* **376** no. 6589, (2022) 170–176.
- [67] ATLAS Collaboration, “Improved W boson Mass Measurement using 7 TeV Proton-Proton Collisions with the ATLAS Detector,” *ATLAS-CONF-2023-004* (2023) .
- [68] CDF Collaboration, D. Acosta *et al.*, “Measurement of the azimuthal angle distribution of leptons from W boson decays as a function of the W transverse momentum in $p\bar{p}$ collisions at $\sqrt{s} = 1.8$ TeV,” *Phys. Rev. D* **73** (2006) 052002, arXiv:hep-ex/0504020.
- [69] W. Bernreuther, D. Heisler, and Z.-G. Si, “A set of top quark spin correlation and polarization observables for the LHC: Standard Model predictions and new physics contributions,” *JHEP* **12** (2015) 026, arXiv:1508.05271 [hep-ph].
- [70] W. Bernreuther and A. Brandenburg, “Tracing CP violation in the production of top quark pairs by multiple TeV proton proton collisions,” *Phys. Rev. D* **49** (1994) 4481–4492, arXiv:hep-ph/9312210.
- [71] M. Czakon, D. Heymes, A. Mitov, D. Pagani, I. Tsirikos, and M. Zaro, “Top-quark charge asymmetry at the LHC and Tevatron through NNLO QCD and NLO EW,” *Phys. Rev. D* **98** no. 1, (2018) 014003, arXiv:1711.03945 [hep-ph].
- [72] T. Gleisberg and S. Hoeche, “Comix, a new matrix element generator,” *JHEP* **12** (2008) 039, arXiv:0808.3674 [hep-ph].
- [73] CMS Collaboration, A. M. Sirunyan *et al.*, “Event shape variables measured using multijet final states in proton-proton collisions at $\sqrt{s} = 13$ TeV,” *JHEP* **12** (2018) 117, arXiv:1811.00588 [hep-ex].

6 Overview of publications

*“When someone speaks, others may misunderstand. But one still has to speak.
For there might be something of value in what others do not misunderstand.”*

— translation from Teller Ede

In the field of theoretical particle physics, all authors are listed alphabetically, rather than in order of the level of contribution. Below follows a short description of each of the publications included in this thesis and my contribution to each one.

Paper I

Electroweak corrections to the angular coefficients in finite- p_T Z -boson production and dilepton decay

Rikkert Frederix, **Timea Vitos**

Eur. Phys. J. C **80**, 939 (2020)

e-print: arXiv:2007.08867 [hep-ph]

In this paper we examine the electroweak corrections to the angular coefficients parametrizing the dilepton channel of the neutral-current Drell-Yan process at pp colliders at center of mass energy of 8 TeV, for a non-zero vector boson p_T . When NLO EW corrections are considered, the expansion of the differential cross section in the eight coefficients is a priori not valid, however, in this paper we examine to which extent the same expansion that holds at NLO QCD also holds for NLO EW corrections. A more careful examination of the input electroweak parameters is needed, as the two parity-odd coefficients, A_3 and A_4 , show strong dependence on the electroweak mixing angle θ_w . This is remedied by including higher order effects in the ρ -parameter for the LO and NLO QCD for a fair comparison with the NLO EW corrections. In addition to the coefficients, we examine the Lam-Tung relation and the electroweak impacts on it.

The idea formulation to this paper was by Rikkert. I performed, with detailed supervision, all calculations presented in the paper. The major part of writing the paper, apart from a large fraction of the results, was done by myself with completion by and discussion with Rikkert.

Paper II

Probing the spin correlations of $t\bar{t}$ production at NLO QCD+EW

Rikkert Frederix, Ioannis Tsinikos, Timea Vitos

Eur. Phys. J. C **81**, 817 (2021)

e-print: [arXiv:2105.11478](https://arxiv.org/abs/2105.11478) [hep-ph]

In this work we investigate the spin correlations in top quark pair production and decay into the dilepton channel. The spin correlation coefficients as they are defined in the spin-density formalism, have been computed at NNLO QCD and with NLO weak corrections previously in the literature. In this work, we investigate the complete-NLO corrections to the production part of this process, including photon-induced partonic channels. In this way, full electroweak effects to all terms at NLO are included at production level, within the narrow-width approximation, producing a top-quark pair on-shell, and then decaying them, including tree-level spin correlation effects, within the decay chain model implemented in MadSpin. Alongside with the spin correlation coefficients, we investigate the complete-NLO effects on various leptonic distributions and asymmetries.

My main contribution to this project was the investigation of the reweighting of events at NLO in fixed-order phase-space point generation in MadSpin. I also performed all the calculations for the observables and distributions, based on a close discussion with Ioannis. I contributed to writing a large part of the introductory sections and to the editing of the paper together with Ioannis.

Paper III

The colour matrix at next-to-leading-colour accuracy for tree-level multi-parton processes

Rikkert Frederix, Timea Vitos

J. High Energ. Phys. **2021**, 157 (2021)

e-print: [arXiv:2109.10377](https://arxiv.org/abs/2109.10377) [hep-ph]

High-multiplicity QCD processes, which is a dominant background at hadron collision facilities such as the LHC, have long presented numerical challenges for their computation. The main reason for the complexity of these processes is due to the large number of terms in the colour expansion which need to be summed, and evaluated for each phase-space point. In this paper, we investigate the possibility to reduce the factorial complexity of the computations by truncating the colour matrix at next-to-leading colour in the large- N_C limit. We do an analysis of the number of non-zero elements at this accuracy in the fundamental and the colour-flow basis and compare these, where possible, to the adjoint basis. The perturbative precision for the investigations is leading order. This study is done for partonic processes, with up to two quark lines. We utilize the phase-space symmetry for identical final state particles to further reduce the number of dual amplitudes that are

needed for the computation of cross sections.

My contribution to this project was to derive all proofs of the rules for obtaining the NLC terms in the colour matrix and to perform all numerical calculations which are presented in the paper, with frequent discussions with Rikkert. I wrote the first draft of the paper, which was later revised to a great extent by Rikkert.

Paper IV

Angular coefficients in $W+j$ production at the LHC with high precision

Mathieu Pellen, Rene Poncelet, Andrei Popescu, Timea Vitos

Eur. Phys. J. C **82**, 693 (2022)

e-print: [arXiv:2204.12394](https://arxiv.org/abs/2204.12394) [hep-ph]

This paper is a natural continuation of paper I: while the latter focuses on completing a state-of-the-art high-precision calculation of the angular coefficients for the neutral-current Drell-Yan process, the present paper presents likewise the NLO electroweak corrections to the charged-current Drell-Yan process, in addition to the NNLO QCD predictions at fixed order, combined in various ways. The results are presented differentially in the W -boson transverse momentum (starting from 30 GeV) and rapidity. These predictions constitute the main theoretical basis for performing a direct measurement of these angular coefficients at the LHC in the near future. In addition, the results serve to reduce the theoretical uncertainty entering through these coefficients of the measurement of the W -boson mass at the LHC.

The main idea formulation for this project; the NLO EW corrections computation; comparison and combination with the NNLO QCD corrections and cross-check of all results and figures in the paper, were my main contributions to this work. The cross-check and combination of the results was done in close collaboration with Andrei. I also took part in contributing to the writing of the introductory parts of the paper and revising it.



Phenomenology: from experiment to theory and then back again.

